JOURNAL OF ADVANCED

APPLIED SCIENCES

E-ISSN: 2979-9759

2026
VOLUME 5
ISSUE 1

WWW.JAASCI.COM

PRENSIP

JOURNAL OF ADVANCED APPLIED SCIENCES

2026 • VOLUME 5 • ISSUE 1

jaasci.com — jadvappsci@gmail.com

prensip.gen.tr — info@prensip.gen.tr

Journal of Advanced Applied Sciences is a peer-reviewed scientific journal published by ***Prensip Publishing*** twice a year.

JOURNAL OF ADVANCED APPLIED SCIENCES

2026 • VOLUME 5 • ISSUE 1

TABLE OF CONTENTS

JAASCI
http://jaasci.com
JOURNAL OF ADVANCED APPLIED SCIENCES
e-ISSN: 2979-9759
PRENSİP
https://prensip.gen.tr

RESEARCH ARTICLE

Refining the Effective Atomic Number of Copper Compounds: A High-Precision Analysis via Rayleigh-to-Compton Scattering Intensity Ratios

Ahmet Turşucu[1]✉ • Mehmet Fatih Turhan[2]

[1]Şırnak University, Faculty of Engineering, Department of Electrical and Electronics Engineering, Şırnak/Türkiye
[2]Afyonkarahisar Health Sciences University, Atatürk Vocational School of Health Service, Department of Medical Imaging Techniques, Afyonkarahisar/Türkiye

ARTICLE INFO

Article History
Received: 15.04.2026
Accepted: 01.06.2026
First Published: 28.06.2026

Keywords
Chemical environment
Copper compounds
Effective atomic number
HPGe detector
Rayleigh-to-Compton scattering

ABSTRACT

This study presents a comprehensive investigation into the effective atomic numbers (Z_{eff}) and electron densities (N_{eff}) of various copper compounds using the Rayleigh-to-Compton (R/C) scattering ratio method. Measurements were performed using a high-resolution HPGe detector and a ^{241}Am radioisotope source emitting 59.54 keV gamma rays. The experimental R/C ratios were utilized to derive Z_{eff} values, which were then compared with theoretical data obtained via WinXCOM. A significant correlation was observed between the chemical environment of the copper compounds and their scattering intensities. One of the main conclusions that can be drawn from the experimental results is how accurately the effective atomic number is determined using data obtained from coherent and Compton scattering. As proof of this, it is clearly seen that the Compton and coherent scattering data obtained from the copper sulfate and copper iodide samples examined during the experiment are highly sensitive to the effective atomic number of the sample used and have a significant effect on spectral analyses. In the experimental results, which also proved this situation experimentally, it is clearly seen that Compton scattering is dominant in samples with low effective atomic numbers, and conversely, coherent scattering becomes dominant in environments with high effective atomic numbers. Thus, our study, with its meaningful results obtained from theoretical calculations and experimental data, has proven that the effective atomic number can be determined in complex chemical structures using the R/C ratio, as we used in our experiments.

Please cite this paper as follows:

Turşucu, A., & Turhan, M. F. (2026). Refining the effective atomic number of copper compounds: A high-precision analysis via Rayleigh-to-Compton scattering intensity ratios. *Journal of Advanced Applied Sciences*, *5*(1), 1-7. https://doi.org/10.61326/jaasci.v5i1.483

1. Introduction

In today's electronic devices and technological applications, copper and certain important copper compounds, preferred due to their atomic structures, form the basis of research and development studies. Copper and its oxide structures play a significant role in superconductivity studies observed at high temperatures and in some critical chemical engineering processes (B. Singh et al., 2010). Furthermore, in semiconductor physics and electronic device development, copper and industrially important copper compounds are preferred due to their high electron-carrying capacity. In addition, the behavior of electronic and industrial devices made from copper compounds in space environments under high radiation conditions has been a subject of interest, and research has been developed in this area. As mentioned, determining the

✉ Correspondence
E-mail address: ahmettursucu@sirnak.edu.tr

shielding or structural change properties of copper and its compounds under radiation and using them in the improvement of developed systems is both a necessity and a requirement for gaining practicality.

The physical response of these compounds to gamma-ray exposure is primarily dictated by their effective atomic number (Z_{eff}). This parameter serves as a crucial bridge between macroscopic material behavior and microscopic interaction cross-sections. Copper is described as an essential transition metal that is frequently used in fundamental sciences, industry, and electronics applications (Kumar et al., 2007). However, some significant differences from its general behavior are observed when copper bonds with different oxide structures and complex ligand structures (such as sulfates). Its behavior changes significantly when bonded with ligands. In fact, these structure shifting create complex electronic structures that cannot be described by standard atomic tables and require explanation. Consequently, a precise investigation into the Z_{eff} of copper compounds offers a unique window into the electronic density redistributions that occur during chemical bonding.

Applications of radiation physics and various studies conducted in this field in recent years clearly demonstrate the interest in non-destructive testing techniques. Examining these studies reveals that the mass absorption method has become a standardized technique. While traditional and standardized techniques are frequently used, efforts to minimize the direct effects encountered in calculations using standard methods by developing alternative methods are evident in literature. The Rayleigh-Compton (R/C) technique is one of these new methods and is a good example of improved experimental methods. Furthermore, this technique eliminates the fluctuations that are caused by source density and sample geometry, which are discrepancies observed in data obtained using traditional absorption techniques.

In this study, we have used different designed experimental setup compared to other researchers that includes lower-energy (59.54 keV) radiation source for irradiation. In addition, this setup includes a high-resolution semiconductor HPGe detector have used for collecting scattered photons. For atomically environment, the interaction between Rayleigh to Compton scattering is highly sensitive at lower radiation source energies. For this purpose, we have set the scattering angle at 167^0 to maximize the energy seperation at Compton and coherent peaks. This allows for a more precise detection of "chemical effects" on Z_{eff}, providing a level of detail that surpasses the generalized approximations found in current radiation interaction databases.

Many technological and industrial applications, such as medical physics and nuclear engineering, are based on creating the most effective radiation shielding design by taking data collected from the interaction of all types of radiation, especially gamma radiation, with matter (Hubbell, 1982; Knoll, 2010). A wide understanding of these procedures requires precise knowledge of Z_{eff}, a parameter first conceptualized to treat composite materials as if they were a single element (Hine, 1952). While the atomic number Z is constant for pure elements, for compounds, Z_{eff} varies depending on the incident photon energy and the specific interaction process involved (Jackson & Hawkes, 1981).

In recent decades, Z_{eff} determination has mostly relied on the total mass attenuation coefficient (μ/ρ) method. However, studies conducted using the mass absorption technique facing significant technical barriers in terms of homogeneity and thickness accuracy of the samples used in the experiment, as noted by various researchers (Han & Demir, 2009; M. P. Singh et al., 2010). Nevertheless, the R/C scattering density ratio has emerged as a robust alternative because it minimizes the source fluctuations and systematic errors related to sample density encountered in other techniques (Duvauchelle et al., 1999; Tursucu et al., 2013). Despite the importance of copper compounds in modern electronics (Edelstein et al., 1997), experimental data on their Z_{eff} especially regarding chemical environment effects remain scarce. Most available data still rely on theoretical structures like WinXCOM (Gerward et al., 2001), which can be able to overlook the fine electronic shifts at the molecular level. Building on our previous work with rare earth oxides (Turşucu et al., 2023), this study aims to fill this gap by providing a high-precision analysis of copper compounds using the refined R/C scattering technique (Jangir et al., 2026).

With this goal in mind, we focused our analysis on a specific set of copper-based materials. These compounds were not chosen at random; they span a broad range of chemical environments and are strategically important in modern technology, where understanding their response to radiation is a practical necessity. Copper-based materials that are used in experimental studies have some specifications and are investigated in three section. In first section, intermetallic and semiconductor advance compounds mentioned. Cu_5Si (Copper Silicide) intermetallic compound is critical in silicon-based microelectronics. The primary purpose of this compound is to form ohmic contacts, thereby creating diffusion barriers. The comprehension of the radiation's effect on this circuit contact element is also crucial. We did these tests with less radiation to do this. We will learn how it reacts to more radiation by using this information. Cu_3N (Copper Nitride) is metastable semiconductor that has gained extensive interest for optical write-once-read-many (WORM) data storage and as a high-performance electrode material in rechargeable batteries. In nanotechnology, this compound is called a smart material (Demir & Turşucu, 2013). It can stay stable in high temperatures and break down when hit by lasers that are very

precise. In second section, chalcogenides and tellurides are mentioned. CuS (Copper Sulfide): Beyond its natural occurrence, CuS is a vital p-type semiconductor used in photo thermal therapy and as a secondary component in thin-film solar cells (CIGS). $CuTe_2$ (Copper Telluride): Known for its complex phase transitions, it is a key material in thermoelectric devices which convert waste heat into electricity. Its high Z components (Tellurium) provide a significant contrast in our Z_{eff} scattering analysis. $CuSe_45(H_2O)$ and H_4CuO_5Se: Selenium is a kind of metalloid that allows for the analysis of diverse effective atomic number patterns during the transition from metallic to covalent bonding. These selenium-based compounds are essential in glass manufacturing and trace minerals in specialized chemical synthesis. We have mentioned the halides and ionic matrices copper compounds in last section. One of these ionic matrices compound is CuI (Copper Iodide) that is a transparent p-type conductor and mandatory component in perovskite solar cells and organic light-emitting diodes (OLEDs). It is notable for its elevated iodine concentration in assessing the R/C sensitivity of substantial atomic compounds utilized in experiments. The other one is $CuSO_4$ (Copper Sulfate) that is a foundational material for electroplating and agricultural chemistry, serving as our benchmark for ionic crystal structures in radiation interaction studies.

In this study, we have studied the copper and its industrial, technological significance compounds. In addition, we calculated certain atomic parameters both theoretical and experimental associated with them. Finally, the experimentally determined effective atomic numbers have been compared with the values obtained in theoretical calculations, and the chemical effects outcomes on the calculated parameters and the discussions were presented together.

2. Experimental Details

2.1. Instrumentation and Geometry

The experimental setup and the following analysis, calculations, and measurements of the obtained data were carried out by using a specifically engineered for high-resolution spectroscopy investigations at scattering geometry. At the heart of the setup is a 5 Ci ^{241}Am annular radioactive source, which provides a steady, monoenergetic 59.54 keV gamma-ray flux. Annular structured radioactive source was selected deliberately to avoid unexpected background counts and ensure the monochromatic spectrum that is collected by highly sensitive detectors. Also, this selection was protecting the detector from directly counting's originating from source.

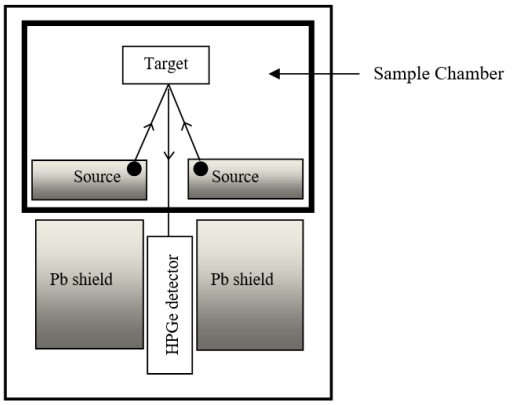

Figure 1. Experimental setup.

The dimensions of the sample holder are presented in Figures 1 and 2. The scattered radiation was measured using a high-purity germanium (HPGe) semiconductor detector. In this experiment, an angle of 167° was selected because at this angle, the difference between the Compton and coherent peaks becomes distinct. To prevent any radiation interference or contamination, lead shields were placed around the sample holder.

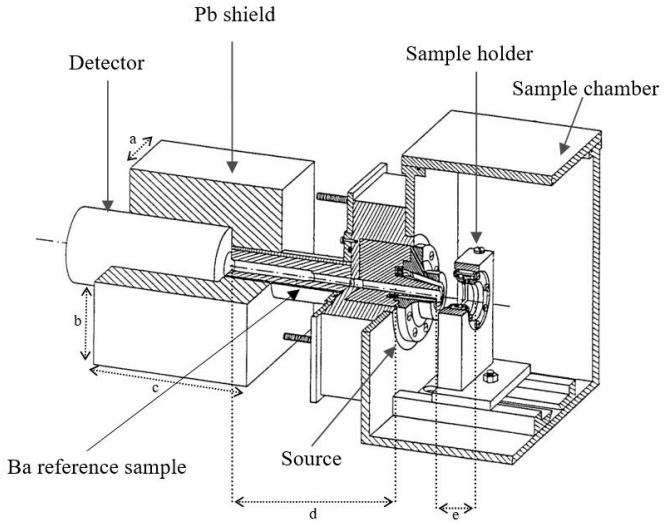

Figure 2. Sample chamber (a=6.5 cm, b=6.3 cm, c=13.5 cm, d=11 cm, e=5 cm).

2.2. Sample Preparation and Data Acquisition

In this experiment, our main emphasis was on the study of pure copper and some significant compounds of copper. For each sample taken, the laboratory-prepared samples were in the form of cylinders. In order to achieve homogeneity of samples, the powder samples were first ground in the mortar to become finely ground. Afterward, these samples were compressed into cylinders through the hydraulic press.

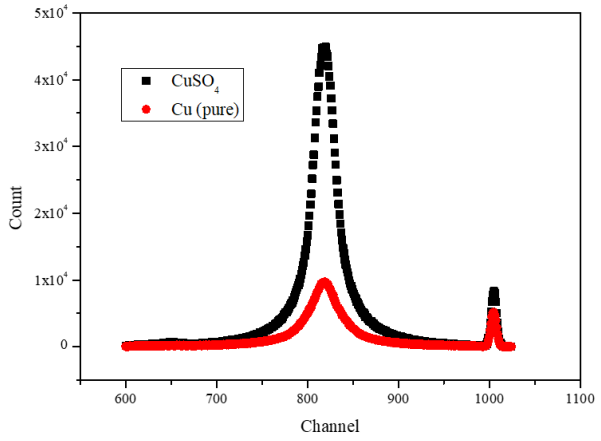

Figure 3. Comparison of scattering spectra for pure Cu and $CuSO_4$ (Experimental pulse height spectra of pure metallic Copper ($Z = 29$) and Copper Sulfate ($CuSO_4, Z_{eff} \cong 21.6$) recorded at a scattering angle of 167°. The plot highlights the transition in scattering intensities as a function of the effective atomic environment.).

The high-resolution detector together with the multi-channel analyzer was used to collect the photons so that spectral data can be achieved (Turhan et al., 2020). Time duration in analysis was set up in such a way that the total number of counts in each spectrum will be 10.000 counts per peak. In this way, we could achieve meaningful and computational data from Rayleigh and Compton spectra. Typical spectra like those presented in Figures 3 and 4 show the difference between coherent and incoherent parts of our selected geometry.

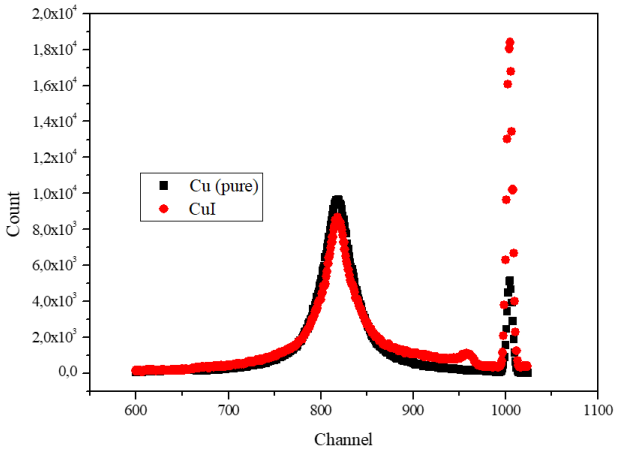

Figure 4. Comparison of scattering spectra for pure Cu and CuI (Pulse height spectra for pure Copper ($Z = 29$) and Copper Iodide ($CuI, Z_{eff} \cong 48.8$). The comparison demonstrates the spectral dominance of high$-Z$ constituents within a copper-based molecular framework.).

2.3. Calibration and Correction Procedures

Accurate Z_{eff} determination requires more than just raw counts; it demands careful correction of the experimental data. It is necessary to consider the following parameters, which include the efficiency of detector photopeak's, the most important of which is considered to be (Zhong et al., 2023). The photopeak efficiency of the HPGe detector (ε) was measured quite accurately according to the calibration sources and pure elements, as shown in the efficiency diagram in Fig. 5. The second parameter is the influence of the attenuation factor. Attenuation caused by the layer of air separating the detector from the sample and by the sample's own absorption was considered.

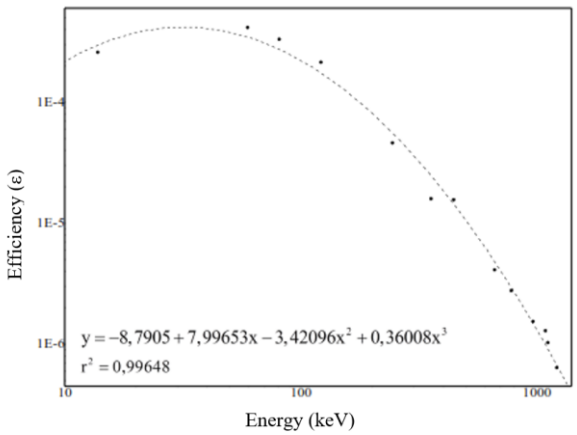

Figure 5. The photopeak efficiency curve for HPGe detector.

Self-absorption correction was handled according to the established transmission-based methodology to ensure that the final R/C ratios reflect the true scattering probabilities of the material. And the last one is the calibration curve that was used in this experiment. A primary calibration was performed using elements (4≤Z≤82). The resulting fit curve (Figure 6) serves as our reference for interpolating the Z_{eff} value of copper compounds.

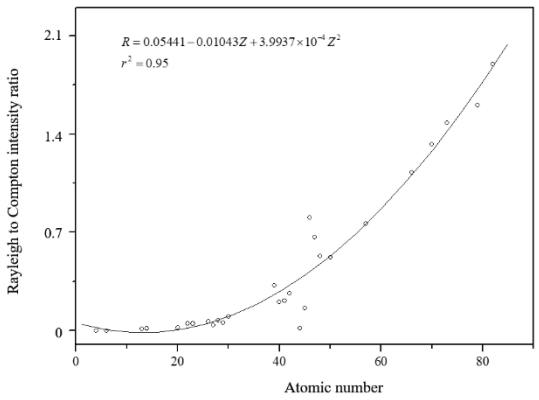

Figure 6. Rayleigh to Compton scattered intensity as a function of atomic number.

3. Theoretical Background

In recent years, the characterization of material properties through the interaction of ionizing radiation has gained significant importance. Specifically, the determination of

effective atomic numbers (Z_{eff}) and electron densities (N_{eff}) for both pure elements and complex compounds depend on the certain measurement of scattering intensity ratios. The above procedure is grounded on the fact that the process of coherent and incoherent scatterings is real physically and exists in the sample itself.

3.1. Coherent (Rayleigh) Scattering

Rayleigh scattering refers to the physical process whereby the incident photon undergoes an elastic collision with the electrons bound in the sample. In this process, both the energy and the wavelength of the photon are conserved, while only the direction changes. The differential cross-section for this elastic process is expressed as:

$$\frac{d\sigma_R}{d\Omega} = \frac{r_0^2}{2}(1 + cos^2\theta)|F(q,Z)|^2 \quad (1)$$

In this expression, $F(q,Z)$ denotes the atomic form factor, which accounts for the distribution of electrons, while q, r_e, and θ represent the momentum transfer, classical electron radius, and scattering angle, respectively.

3.2. Incoherent (Compton) Scattering

The process of Compton scattering consists of an inelastic scattering process of high energy photons on atomic electrons unlike other processes of elastic scattering. The Compton scattering phenomenon is used as empirical evidence that the particles of radiation have properties of momentum transfer and decrease in frequency (Cinan & Yılmaz, 2021). The differential cross-section for such inelastic scattering is governed by the Klein-Nishina formulation:

$$(\frac{d_\sigma}{d_\Omega})_{KN} = \frac{1}{2}r_0^2\left(\frac{E}{E_0}\right)^2(\frac{E_0}{E} + \frac{E}{E_0} - sin^2\theta) \quad (2)$$

Where E_0 and E correspond to the incident and scattered photon energies. The degree of momentum transfer is significantly influenced by the incoherent scattering function, $S(q,Z)$. In high momentum transfer conditions, $S(q,Z)$ approaches the total number of atomic electrons (Z), whereas it decreases as the transfer approaches zero.

3.3. The R/C Ratio and Effective Atomic Number

This study was based on a fundamental principle that namely Rayleigh to Compton scattering cross-section ratio. This principle (R/C) ensures a unique spectral signature that is strictly related to the atomic environment of the target material investigated. The atomic Compton scattering cross-section ($\sigma_{inc,a}$), occurring from bound electrons, is defined as:

$$R = \left(\frac{d\sigma}{d\Omega}\right)_R / \left(\frac{d\sigma}{d\Omega}\right)_{aC} \propto \frac{|F(q,Z)|^2}{S(q,Z)} \quad (3)$$

$$(\frac{d\sigma}{d\Omega})_{aC} = S(q,Z)(\frac{d\sigma}{d\Omega})_{KN} \quad (4)$$

The parameterization of $F(q,Z)$ and $S(q,Z)$ is based on the comprehensive data provided by Hubbell (1982). The effective atomic number, Z_{eff}, is derived from the weighted atomic percentages of the sample constituents. This parameter directly reflects the electronic landscape of the target and is calculated through the following summation:

$$R = \left(\frac{d\sigma}{d\Omega}\right)_R / \left(\frac{d\sigma}{d\Omega}\right)_{aC} \propto \frac{\sum_{j=1}^{n} a_j^{at}|F(q,Z_j)|^2}{\sum_{j=1}^{n} a_j^{at} S(q,Z_j)} \quad (5)$$

$$a_j^{at} = \frac{(W_j/A_j)}{\sum_j (W_j/A_j)} \quad (6)$$

Where W_j represents the fractional weight and A_j represents the atomic mass of the jth element within the molecular structure.

4. Results and Discussion

The experimental R/C ratios, effective atomic numbers (Z_{eff}), and electron densities(N_{eff}) determined for the selected copper compounds are summarized in Table 1. To validate the experimental findings, theoretical Z_{eff} values were calculated using the WinXCOM database, and a high degree of correlation was observed across the studied energy range.

Table 1. Rayleigh to Compton scattered intensity ratio, experimental and theoretical effective atomic numbers of copper compounds.

Copper Compounds	Rayleigh to Compton intensity ratio	Effective Atomic Number Experimental	Other Experimental	Theoretical	Effective Electron Density (Theoretical) (*electrons/g*)
$CuSO_4$	0.0294±0.002	20.995±0.756	--	21.6	8.147E+22
CuS	0.0731±0.002	27.045±0.741	--	26.4	1.662E+23
Cu_5Si	0.1023±0.002	30.529±0.807	--	28.2	4.910E+22
CuI	0.4366±0.002	48.791±0.941	--	47.3	1.495E+23
$CuSe_4.5(H_2O)$	0.0493±0.003	23.877±0.983	--	25.8	2.853E+22
H_4CuO_5Se	0.1253±0.002	32.993±0.864	--	24.9	6.620E+22
$CuTe_2$	0.3922±0.002	47.941±0.798	--	49.8	9.413E+22
Cu_3N	0.0823±0.002	28.194±0852	--	24.4	7.185E+22

The sensitivity of scattering cross-sections to the chemical environment is visually demonstrated in Figures 3 and 4. Figure 3 compares the pulse height spectra of pure Copper (Z=29) and $CuSO_4$ ($Z_{eff} \cong 21.6$). As expected from the Z^n dependence of elastic scattering, the coherent (Rayleigh) peak of pure copper is significantly more intense than that of the sulfate compound. This reduction in Z_{eff} in $CuSO_4$ leads to a relative increase in the Compton profile, confirming that inelastic scattering becomes more prominent in lower-Z molecular environments.

In contrast, Figure 4 illustrates the effect of a high-Z constituent by comparing pure Copper with Copper Iodide (CuI, $Z_{eff} \cong 48.8$). The presence of Iodine ($Z = 53$) results in a dramatic enhancement of the Rayleigh peak, which nearly triples the intensity observed in metallic copper. This sharp contrast provides a robust experimental verification of the R/C method's ability to detect subtle changes in the effective atomic charge of complex materials.

The slight discrepancies observed in some compounds, such as H_4CuO_5Se, between experimental and theoretical Z_{eff} values can be attributed to the influence of molecular bonding effects and the local electronic environment, which are not fully accounted for in the independent atom model (IAM) used by WinXCOM. Overall, the consistent agreement between the measured R/C ratios and the theoretical expectations reinforce the reliability of using HPGe-based gamma-ray spectrometry for material characterization.

5. Conclusion

For the analysis of Cu based high electrical value materials, the present study has been focused on the determination of effective atomic number and effective electron density of these compounds via Rayleigh to Compton scattering ratio technique. The employment of very sensitive HPGe detector helped us obtain pronounced peaks corresponding to Rayleigh and Compton effects.

The main focus of this research work lies in demonstrating the results of the interactions of the radiation through effective atomic number of composite materials. Moreover, some values of effective atomic number of certain copper compounds obtained here constitute previously unknown data, thereby providing significant input to current literature. It is clear that the application of R/C ratio method can be considered useful in radiation protection, materials science, and medicine.

Acknowledgment

This work was supported by Şırnak University Research Fund (BAP): [Grant Number 2025.FNAP.06.02.02].

Conflict of Interest

The authors have no conflict of interest to declare.

Disclosure of Generative AI Use

No generative artificial intelligence tools were used in the preparation of this article.

References

Cinan, E., & Yılmaz, D. (2021). Effective atomic numbers of boron compounds obtained using Rayleigh to compton scattering intensity ratio. *Applied Radiation and Isotopes*, *174*, 109753. https://doi.org/10.1016/j.apradiso.2021.109753

Demir, D., & Turşucu, A. (2013). Measurement of the effective atomic number of Fe_xCr_{1-x} and Fe_xNi_x alloys using scattering of gamma rays. *Journal of Alloys and Compounds*, *581*, 213-216. https://doi.org/10.1016/j.jallcom.2013.07.057

Duvauchelle, P., Peix, G., & Babot, D. (1999). Effective atomic number in the Rayleigh to Compton scattering ratio. *Nuclear Instruments and Methods in Physics Research Section B: Beam Interactions with Materials and Atoms*, *155*(3), 221-228. https://doi.org/10.1016/S0168-583X(99)00450-4

Edelstein, D., Heidenreich, J., Goldblatt, R., Cote, W., Uzoh, C. E., Lustig, N. E., Roper, P., McDevitt, T., Motsiff, W., Simon, A. H., Dukovic, J., Wachnik, R., Rathore, H., Schulz, R., Su, L., Luce, S., & Slattery, J. (1997). *Full copper wiring in a sub-0.25 μm CMOS ULSI technology*. IEEE International Electron Devices Meeting (IEDM). Washington. https://doi.org/10.1109/IEDM.1997.650496

Gerward, L., Guilbert, N., Jensen, K. B., & Levring, H. (2001). X-ray absorption in matter. Reengineering XCOM. *Radiation Physics and Chemistry*, *60*(1-2), 23-24. https://doi.org/10.1016/S0969-806X(00)00324-8

Han, I., & Demir, L. (2009). Mass attenuation coefficients, effective atomic and electron numbers of Ti and Ni alloys. *Radiation Measurements*, *44*(3), 289-294. https://doi.org/10.1016/j.radmeas.2009.03.010

Hine, G. J. (1952). The effective atomic numbers of materials for various gamma-ray interactions. *Physical Review*, *85*(4), 725-725.

Hubbell, J. H. (1982). Photon mass attenuation and energy-absorption coefficients. *The International Journal of Applied Radiation and Isotopes*, *33*(11), 1269-1290. https://doi.org/10.1016/0020-708X(82)90248-4

Jackson, D. F., & Hawkes, D. J. (1981). X-ray attenuation coefficients of elements and mixtures. *Physics Reports*, *70*(3), 169-233. https://doi.org/10.1016/0370-1573(81)90014-4

Jangir, H. K., Mandal, A., & Srinivasan, V. (2026). A parametric study on the dynamic behavior of closed-end floating pipe pile in cohesionless soil: Effect of diameter, stiffness, and interface characteristics under

dynamic excitation. *Ocean Engineering*, *343*, 123596. https://doi.org/10.1016/j.oceaneng.2025.123596

Knoll, G. F. (2010). *Radiation detection and measurement*. John & Wiley Sons Inc.

Kumar, S., Sharma, V., Mehta, D., & Singh, N. (2007). Rayleigh, Compton and K-shell radiative resonant Raman scattering in 83Bi for 88.034 keV γ-rays. *Nuclear Instruments and Methods in Physics Research Section B: Beam Interactions with Materials and Atoms*, *264*(1), 1-8. https://doi.org/10.1016/j.nimb.2007.07.021

Singh, B., Kumar, V., & Sidhu, G. S. (2010). Investigations of mass attenuation coefficients and energy absorption buildup factors of some low-Z gamma-ray shielding materials. *International Journal of Latest Research in Science and Technology*, *2*(5), 73-77.

Singh, M. P., Sharma, A., Singh, B., & Sandhu, B. S. (2010). Non-destructive evaluation of scientific and biological samples by scattering of 145 keV gamma rays. *Radiation Measurements*, *45*(8), 960-965. https://doi.org/10.1016/j.radmeas.2010.01.021

Turhan, M. F., Akman, F., Polat, H., Kaçal, M. R., & Demirkol, İ. (2020). Gamma-ray attenuation behaviors of hematite doped polymer composites. *Progress in Nuclear Energy*, *129*, 103504. https://doi.org/10.1016/j.pnucene.2020.103504

Tursucu, A., Demir, D., & Onder, P. (2013). Effective atomic number determination of rare earth oxides with scattering intensity ratio. *Science and Technology of Nuclear Installations*, *2013*(1), 738978. https://doi.org/10.1155/2013/738978

Turşucu, A., Elmahroug, Y., & Yılmaz, D. (2023). Radiation shielding calculations of some selected rare earth oxides. *Radiation Physics and Chemistry*, *212*, 111066. https://doi.org/10.1016/j.radphyschem.2023.111066

Zhong, J. X., Shih, J. Y., & Wang, F. K. (2023). Four-channel phase and quadrature self-injection-locked (PQSIL) radar for displacement monitoring using a modified principal component analysis (MPCA) method. *IEEE Transactions on Microwave Theory and Techniques*, *72*(1), 822-835. https://doi.org/10.1109/TMTT.2023.3318851

http://jaasci.com
JOURNAL OF ADVANCED APPLIED SCIENCES
e-ISSN: 2979-9759
https://prensip.gen.tr

RESEARCH ARTICLE

Characterization of Positive and Negative Ionospheric Storm Phases Using TNPGN-Active TEC Estimates Spanning Solar Cycles 24 and 25 (2019-2023)*

Secil Karatay[1]✉ • Feza Arikan[2] • Orhan Arikan[3]

[1]Kastamonu University, Faculty of Engineering and Architecture, Department of Electrical Electronics Engineering, Kastamonu/Türkiye
[2]Hacettepe University, Faculty of Engineering, Department of Electrical Electronics Engineering, Ankara/Türkiye
[3]İhsan Doğramacı Bilkent University, Faculty of Engineering, Department of Electrical Electronics Engineering, Ankara/Türkiye

ARTICLE INFO

Article History
Received: 13.04.2026
Accepted: 15.06.2026
First Published: 28.06.2026

Keywords
Geomagnetic storm
GNSS-TEC
Ionospheric storm
Mid-latitude ionosphere
Solar Cycle 24-25
TNPGN-Active

ABSTRACT

Geomagnetic storms induce significant perturbations in the ionosphere, profoundly affecting Total Electron Content (TEC) and consequently the performance of Global Navigation Satellite Systems (GNSS). This study characterizes the positive and negative phases of ionospheric storms over Türkiye during 14 geomagnetically disturbed days (maximum 3-hourly Kp > 6, corresponding to G2–G4 storms on the NOAA scale) spanning January 2019 to June 2023. The period covers the deep minimum of Solar Cycle 24 (SC24) and the ascending phase of Solar Cycle 25 (SC25). High-resolution IONOLAB-TEC estimates at 2.5-minute intervals are derived from nine continuously operating stations of the Turkish National Permanent GNSS Network-Active (TNPGN-Active). These stations, distributed across geodetic latitudes 36.59°N-42.01°N and longitudes 26.33°E-44.34°E, provide comprehensive spatial coverage of the mid-latitude ionosphere over the Eastern Mediterranean and Anatolian region. A single geomagnetically quiet reference day (07 May 2022) is selected and an observation-driven pre-storm scaling procedure is applied to normalize the TEC time series. This approach effectively accounts for seasonal and solar-cycle differences in background ionization levels without dependence on empirical models. Analysis of network-averaged normalized TEC deviations ($r\Delta TEC$) reveals that storm responses are governed by a complex interplay of factors. Storm intensity provides a first-order control on perturbation magnitude, with G4 events generally producing larger peak positive deviations. However, the local time of storm onset strongly modulates phase dominance: near-noon onsets favor prolonged negative phases associated with thermospheric composition changes, while midnight-to-morning onsets promote extended positive phases driven by prompt penetration and disturbance dynamo electric fields. Seasonal dependence is pronounced, with spring events displaying the most consistent positive responses, winter conditions amplifying relative enhancements due to lower baseline TEC and summer suppressing both phases. Pre-storm scaling factors clearly reflect the solar-cycle transition, showing a roughly twofold increase in background TEC from the SC24 minimum to early SC25. These results establish a regional observational baseline for mid-latitude ionospheric storm morphology in an underrepresented longitude sector. They highlight the value of dense GNSS networks and observation-based normalization techniques for advancing space weather understanding and improving GNSS reliability as Solar Cycle 25 approaches its maximum.

Please cite this paper as follows:

Karatay, S., Arikan, F., & Arikan, O. (2026). Characterization of positive and negative ionospheric storm phases using TNPGN-Active TEC estimates spanning Solar Cycles 24 and 25 (2019-2023). *Journal of Advanced Applied Sciences*, *5*(1), 8-23. https://doi.org/10.61326/jaasci.v5i1.481

1. Introduction

The ionosphere, a dynamic layer of Earth's upper atmosphere extending roughly from 60 to 1000 km altitude, plays a critical role in modulating the propagation of radio waves, particularly those used by Global Navigation Satellite Systems (GNSS) (Hernández-Pajares, et al., 2011; Jakowski, et al., 2012; Ren, et al., 2016). Total Electron Content (TEC), defined as the integrated number of free electrons along a signal path through the ionosphere (typically expressed in TEC units, where 1 TECU = 10^{16} electrons/m^2), directly influences the refractive index experienced by L-band GNSS signals (Arikan,

* A supplementary file for this article is available at https://doi.org/10.61326/jaasci.v5i1.481

✉ Correspondence
E-mail address: skaratay@kastamonu.edu.tr

et al., 2003; Nayir, et al., 2007). This leads to group delay and phase advance effects that can introduce positioning errors ranging from meters to tens of meters if not properly modeled or corrected (Arikan, et al., 2008). Under geomagnetically quiet conditions, the ionosphere exhibits predictable diurnal, seasonal, and solar-cycle variations driven primarily by solar Extreme Ultra Violet (EUV) radiation (Vaishnav, et al., 2019), neutral winds (Lu, et al., 1995) and background electric fields (Pudovkin, 1974). However, during periods of heightened geomagnetic activity, triggered by Coronal Mass Ejections (CMEs), high-speed solar wind streams, or other solar wind structures interacting with Earth's magnetosphere, the ionosphere undergoes rapid and often dramatic perturbations known as ionospheric storms (Fuller-Rowell, et al., 1994; Lei, et al., 2008; Lyon, 2000; Ridley, et al., 2006a).

Geomagnetic storms are quantified through indices such as the planetary Kp (measuring global geomagnetic disturbance on a 0–9 scale) (GFZ, 1956), the Disturbance storm time (Dst) index (reflecting the intensity of the equatorial ring current) and the high-resolution SYM-H index (a one-minute analogue of Dst (WDC, 1957) When the Interplanetary Magnetic Field (IMF) turns southward, efficient magnetic reconnection at the dayside magnetopause allows solar wind energy to penetrate the magnetosphere, leading to enhanced convection electric fields, Joule heating in the high-latitude thermosphere and the generation of disturbance dynamo electric fields (Maruyama, et al., 2005; Sojka, et al., 1986; Vasyliūnas & Song, 2005; Yu & Ridley, 2009). These processes cascade downward, altering thermospheric composition (notably the O/N_2 ratio), neutral winds and plasma transport at mid-latitudes (Rishbeth & Garriott, 1969). The resulting ionospheric responses manifest as either positive phases (enhancements in electron density and TEC, often driven by prompt penetration electric fields or equatorward neutral winds that uplift plasma to altitudes of reduced recombination) or negative phases (depletions in TEC, typically linked to changes in thermospheric composition where molecular-rich air is transported equatorward, increasing recombination rates) (Fagundes, et al., 2016; Jin, et al., 2017; Mishin, et al., 2019; Ridley, et al., 2006b). These phases do not occur uniformly; their dominance, timing, duration and spatial extent depend on a complex interplay of factors including the storm's intensity and duration, the local time of onset, season, longitude and the prevailing level of solar activity. Storms commencing near local midnight or in the morning sector at mid-latitudes frequently favor prolonged positive responses due to favorable electric field configurations (Huang, et al., 2005; Wang, et al., 2010), whereas daytime-onset events (especially near local noon) tend to promote composition-driven negative phases (Akala, et al., 2023; Gulyaeva & Stanislawska, 2005). Seasonal asymmetries arise from differences in background thermospheric circulation and background plasma density: winter conditions often amplify relative TEC enhancements because of lower baseline densities (Yasyukevich, et al., 2020), while summer solstice periods can suppress both positive and negative responses due to less favorable neutral composition (Gulyaeva, et al., 2014; Karatay, et al., 2017; Karatay, 2020c). Longitudinal variations further complicate the picture, as the offset between geographic and geomagnetic coordinates influences the efficiency of energy deposition and plasma redistribution (Karatay, 2020a; Karatay, 2020b).

The transition from Solar Cycle 24 (SC24) to Solar Cycle 25 (SC25) offers a particularly valuable observational window for such studies. SC24 was notably weak, with a prolonged and deep minimum characterized by unusually low sunspot numbers, reduced EUV flux and subdued geomagnetic activity (Richardson, 2013; Watari, 2017). In contrast, the ascending phase of SC25 has shown a more robust increase in solar activity, with a higher frequency of intense geomagnetic events in 2021–2023 compared to the preceding minimum years (Hajra, et al., 2021; Javaraiah, 2022; Upton & Hathaway, 2023). This progression allows examination of how ionospheric storm morphology evolves with changing background solar flux levels, as higher EUV illumination elevates the ambient F-region plasma density and alters the ionosphere's susceptibility to external forcing (Yeeram, 2024). Multi-year analyses spanning this transition thus help disentangle solar-cycle modulation from pure geomagnetic drivers.

Mid-latitude regions, situated between the Equatorial Ionization Anomaly (EIA) and auroral zones, serve as sensitive indicators of these coupled magnetosphere–ionosphere–thermosphere processes. Unlike equatorial latitudes, where fountain-effect amplification and plasma bubbles dominate, or high latitudes dominated by particle precipitation and convection, mid-latitudes experience a balanced influence from both prompt penetration fields and longer-lived disturbance dynamo effects, as well as equatorward-propagating thermospheric disturbances (Wehmeyer, et al., 2026; Yi Liu, et al., 2021). Over the Eastern Mediterranean and Anatolian plateau, the ionosphere lies in a transitional zone influenced by European, African and Asian longitudinal sectors, making it responsive to both hemispheric asymmetries and regional geomagnetic field geometry (Doğanalp & Köz, 2024; Ghafar, et al., 2024). Türkiye, spanning geodetic latitudes approximately 36°N to 42°N and longitudes 26°E to 44°E, provides excellent geographic coverage of this mid-latitude domain. Its position allows investigation of spatial gradients across nearly 18° of longitude, capturing variations that may arise from differences in magnetic declination, local time sectors and proximity to the mid-latitude trough during disturbed conditions (Erken, et al., 2019; Karatay, et al., 2017; Karatay, 2020a; Karatay, 2020b; Karatay, 2020c).

Previous regional studies in the Eastern Mediterranean and surrounding areas have documented ionospheric storm effects using various techniques, including ionosondes (Haralambous

& Makrominas, 2024; Paul, et al., 2025; Pietrella, et al., 2018), GNSS networks and satellite observations (Campuzano, et al., 2023; Pica, et al., 2025; Şentürk, 2020). These works have highlighted the occurrence of both positive and negative phases, their dependence on storm onset local time and occasional preconditioning effects during consecutive storm sequences. However, comprehensive analyses employing dense, continuously operating GNSS reference networks, such as the Turkish National Permanent GNSS Network-Active (TNPGN-Active), remain relatively limited for the SC24/SC25 transition period, particularly when focusing on events selected by consistent intensity thresholds (e.g., Kp ≥ 6, corresponding to G2 or stronger on the National Oceanic and Atmospheric Administration (NOAA) scale). Such networks enable high-temporal-resolution (e.g., 2.5-minute) TEC estimation across multiple stations, facilitating network-averaged characterizations that reduce local noise and reveal regional coherence or variability (Arikan, et al., 2016; Koroglu & Arikan, 2025).

Understanding ionospheric responses over Türkiye carries both scientific and practical significance (Karatay, et al., 2017; Karatay, 2020a; Karatay, 2020b; Karatay, 2020c). Scientifically, it contributes to global models of storm-time ionospheric dynamics by filling a data gap in a longitude sector underrepresented in many statistical studies. Practically, reliable TEC characterization is essential for mitigating GNSS errors in applications ranging from precise point positioning and real-time kinematic surveying to aviation, maritime navigation and satellite-based augmentation systems. During geomagnetic storms, unmodeled TEC gradients and scintillations can degrade positioning accuracy, increase cycle slips and even cause signal loss-of-lock, with economic and safety implications (Koroglu & Arikan, 2025). Moreover, as solar activity rises toward the SC25 maximum, the frequency and intensity of such disturbances are expected to increase, underscoring the need for observation-based benchmarks derived from regional GNSS infrastructure.

This study leverages IONOLAB-TEC estimates from nine TNPGN-Active stations distributed across distinct geographic zones of Türkiye to analyze the ionospheric response during 14 geomagnetically disturbed days (selected on the basis of maximum 3-hourly Kp > 6) between January 2019 and June 2023. These events encompass a range of intensities (G2 to G4), seasonal contexts and solar activity backgrounds, spanning the late minimum of SC24 and the ascending phase of SC25. A single geomagnetically quiet reference day is employed in conjunction with an observation-driven pre-storm scaling procedure to normalize IONOLAB-TEC time series, thereby isolating storm-induced deviations while accounting for seasonal and solar-cycle differences in background levels. The analysis examines absolute and relative TEC deviations, network-mean responses, peak positive/negative excursions, phase durations and statistical distributions stratified by storm class and season. By integrating supporting geomagnetic indices (Kp, Dst, SYM-H) (GFZ, 1956; WDC, 1957) and focusing on spatial averaging across the Anatolian network, the work aims to elucidate the dominant controlling factors, storm intensity, onset timing, season and solar background, on mid-latitude ionospheric storm morphology in this region.

2. Materials and Methods

This study analyzes the ionospheric response over Türkiye during geomagnetically disturbed periods using TEC estimates derived from nine continuously operating GNSS reference stations of the TNPGN-Active. The stations are distributed across nine distinct geographic zones of Türkiye, spanning geodetic latitudes from 36.59°N to 42.01°N and longitudes from 26.33°E to 44.34°E (Table 1), thereby providing spatial coverage of the mid-latitude ionosphere over the Eastern Mediterranean and Anatolian region. The geographic locations of the selected stations are shown in Figure 1.

The study period covers January 2019 to June 2023, encompassing the deep minimum of Solar Cycle 24 (SC24) and the ascending phase of Solar Cycle 25 (SC25). Geomagnetically disturbed days are selected based on the planetary Kp index, provided by the German Research Centre for Geosciences (GFZ Potsdam) (GFZ, 1956). Days on which the maximum 3-hourly Kp value exceeded 6, corresponding to at least a G2-class geomagnetic storm on the NOAA scale, are included in the analysis. This criterion yielded 14 disturbed days ranging from G2 to G4 in storm intensity, as listed in Table 2. The selected events include storms occurring across all four seasons and under varying solar activity levels, enabling an assessment of seasonal and solar-cycle effects on the ionospheric storm response (Matzka, et al., 2021). The disturbance storm time (Dst) index and the SYM-H index were obtained from the World Data Center for Geomagnetism, Kyoto (WDC Kyoto) (WDC, 1957).

Table 1. Chosen TNPGN-Active stations located in nine different zones across Türkiye.

Station Name/ID	Latitude (°N)	Longitude (°E)
Adana/ADN2	36.59	35.19
Ardahan/ARDH	41.06	42.41
Boğazlıyan/BOG1	39.11	35.15
Edirne/EDIR	41.40	26.33
Kırkağaç/KIKA	39.06	27.40
Muğla/MUG1	37.12	28.21
Muradiye/MUR1	38.59	43.45
Şemdinli/SEM1	37.18	44.34
Sinop/SINP	42.01	35.09

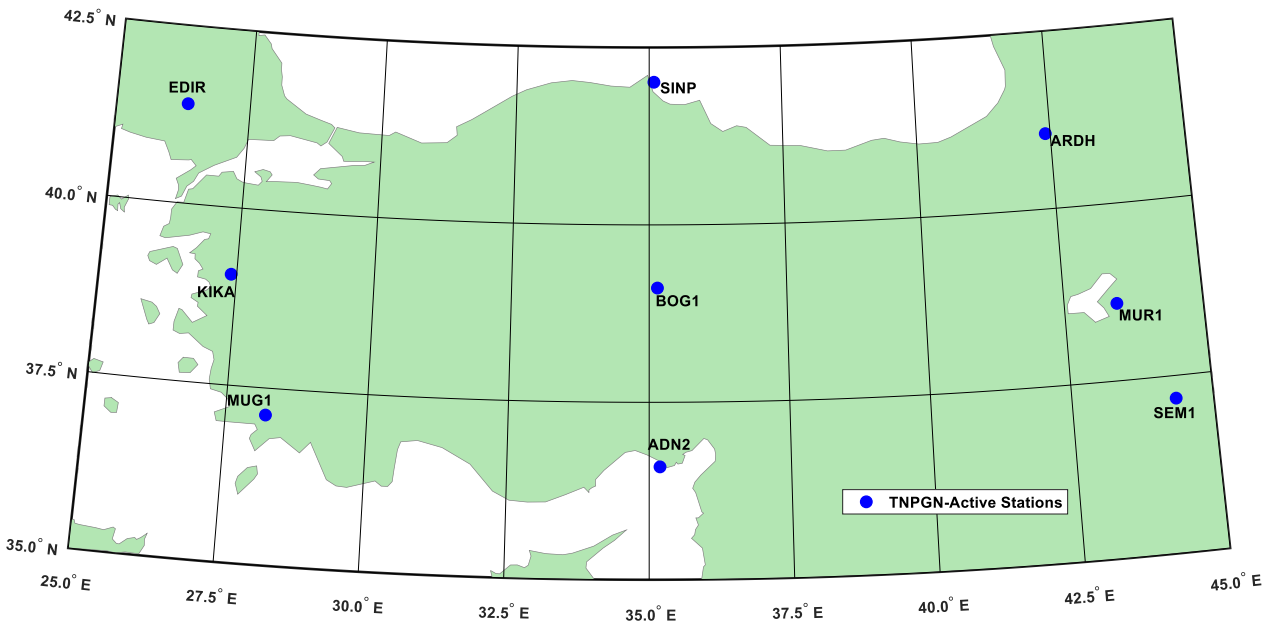

Figure 1. Geographic locations of the TNPGN-Active stations used in the study.

Table 2. Chosen geomagnetically disturbed days and quiet day between 2019-2023.

Geomagnetic Condition	Day	Kp maks.	Class	Season	Onset (UT)
Disturbed days	14 May 2019	6.3	G2	Spring	05:00
	12 May 2021	7.0	G3	Spring	13:00
	12 October 2021	6.3	G2	Autumn	00:00*
	03 November 2021	6.3	G2	Autumn	22:00
	04 November 2021	7.7	G3	Autumn	05:00
	13 March 2022	6.3	G2	Spring	15:00
	10 April 2022	6.6	G2	Spring	06:00
	17 August 2022	6.6	G2	Summer	20:00
	04 September 2022	6.3	G2	Autumn	05:00
	27 February 2023	6.6	G2	Winter	00:00*
	23 March 2023	7.0	G3	Spring	12:00
	24 March 2023	8.0	G4	Spring	00:00
	23 April 2023	8.3	G4	Spring	12:00
	24 April 2023	8.0	G4	Spring	00:00*
Quiet Day	07 May 2022	1.6	—	Spring	05:00

The Class column refers to the NOAA geomagnetic storm scale (G1–G5, Kp ≥ 5); dash indicates no storm condition. Asterisk (*) denotes events for which the storm onset preceded the start of the observational window; a one-hour fallback scaling window was applied as described in Section 2.1.

Dst is a hourly index that quantifies the globally symmetric disturbance of the horizontal geomagnetic field component at equatorial latitudes and is widely used to characterize the intensity and phase of geomagnetic storms (Sugiura, 1964). SYM-H is the one-minute equivalent of Dst, providing higher temporal resolution suitable for identifying the precise onset timing of each storm event (Nakano & Iyemori, 2005). The Kp and Dst time series for all 14 disturbed days, together with the quiet reference day, are presented in Figure 2. The corresponding SYM-H time series are shown in Figure 3. A single geomagnetically quiet day (07 May 2022, $Kp_{max} = 1.33$, $Dst_{min} = -10\ nT$) is selected as the reference baseline for the normalization procedure described in Section 2.1.

2.1. Normalization of IONOLAB-TEC Time Series and Derivation of Ionospheric Storm Response

The IONOLAB-TEC algorithm computes VTEC from dual-frequency GPS observations by forming the geometry-free linear combination of the L1 (1575.42 MHz) and L2 (1227.60 MHz) carrier phase and pseudorange measurements, which eliminates the first-order ionospheric delay while retaining the TEC signal. Differential Code Biases (DCBs) for both satellites and receivers are estimated simultaneously within the

regularization framework of the algorithm, following the approach described in Arikan et al. (2003, 2008), thereby avoiding reliance on externally provided DCB products. The 2.5-minute output cadence corresponds to the highest temporal resolution achievable from standard 30-second RINEX observation files through the smoothed carrier-phase leveling procedure implemented in the algorithm and is particularly advantageous for resolving the rapid onset and recovery dynamics of ionospheric storm phases, which can evolve on timescales of tens of minutes.

IONOLAB-TEC provides TEC estimates at 2.5-minute intervals for each station and day. For station u, storm d_s and quiet reference day d_q, the IONOLAB-TEC time series is represented as the column vector:

$$\boldsymbol{x}_{u;d_s,d_q} = \left[x_{u;d_s,d_q}(1) \dots x_{u;d_s,d_q}(n) \dots x_{u;d_s,d_q}(N)\right]^T \quad (1)$$

where $N = 576$ is the total number of samples per day (24 h × 60 min / 2.5 min) and $n = 1,2,\dots,N$ denotes the sample index.

Since the 14 storm events span multiple years and seasons, the absolute IONOLAB-TEC level of the single quiet reference day (07 May 2022) differs from the pre-storm background of each event due to seasonal variation and solar activity changes across Solar Cycle 25. To account for these differences without relying on empirical models, a pre-storm window scaling factor is computed from observations alone.

For each storm event d_s and station u, the storm onset sample index n_{onset} is determined as the first hourly interval at which the Dst index falls below -30 nT. For events where Dst already satisfies this criterion at $n = 1$ (i.e., the storm commenced on the preceding day), a one-hour window ($n_{onset} = 24$ samples) s used instead. The scaling factor is then defined as:

$$k_{u;d_s} = \frac{\frac{1}{n_{onset}}\sum_{n=1}^{n_{onset}} x_{u;d_s}(n)}{\frac{1}{n_{onset}}\sum_{n=1}^{n_{onset}} x_{u;d_q}(n)} \quad (2)$$

where the numerator and denominator are the pre-storm means of the storm day and quiet reference day, respectively, computed over the same time window. The one-hour fallback window is a deliberate conservative choice: it retains the largest possible pre-storm sample while remaining strictly prior to any storm-driven TEC perturbation. However, its application to four events (12 October 2021, 27 February 2023, 24 March 2023, 24 April 2023), in which geomagnetic activity had already commenced before the start of the observational window, introduces a potential source of scaling uncertainty. If storm-driven TEC enhancements are already present within this one-hour window, the computed k will be slightly overestimated relative to the true quiet background, leading to a marginally higher TEC_{ref} and consequently a modest underestimation of the positive $r\Delta TEC$ for those events. Conversely, if a negative phase is already underway, k will be slightly underestimated, amplifying the apparent positive deviation. The direction and magnitude of this effect are event-dependent and cannot be fully quantified without multi-day pre-storm TEC data. Nevertheless, the impact on the primary conclusions of this study, storm phase polarity, duration and the relative ordering of events by intensity class and season, is expected to be minor, as the one-hour window captures the diurnal TEC shape sufficiently to constrain the scaling ratio.

The scaled quiet-day reference vector for station u and storm event d_s is then:

$$\boldsymbol{x}^{ref}_{u;d_s} = k_{u;d_s} \cdot \boldsymbol{x}_{u;d_q} \quad (3)$$

The absolute IONOLAB-TEC deviation is computed as:

$$\Delta\boldsymbol{x}_{u;d_s} = \boldsymbol{x}_{u;d_s} - \boldsymbol{x}^{ref}_{u;d_s} \quad (4)$$

and the normalized relative deviation, expressed as a percentage, is:

$$r\Delta x_{u;d_s}(n) = \frac{x_{u;d_s}(n) - x^{ref}_{u;d_s}(n)}{x^{ref}_{u;d_s}(n)} \times 100 \quad (5)$$

Values of $r\Delta x_{u;d_s}(n) > 0$ indicate a positive ionospheric storm phase (IONOLAB-TEC enhancement), while $r\Delta x_{u;d_s}(n) < 0$ indicate a negative phase (IONOLAB-TEC depletion).

To characterize the spatially averaged ionospheric response over Türkiye, the network mean and standard deviation of the relative deviation are computed across all $U = 9$ stations at each time sample:

$$\overline{r\Delta x_{d_s}}(n) = \frac{1}{U}\sum_{u=1}^{U} r\Delta x_{u;d_s}(n) \quad (6)$$

$$\sigma_{r\Delta x_{d_s}}(n) = \sqrt{\frac{1}{U}\sum_{u=1}^{U}\left[r\Delta x_{u;d_s}(n) - \overline{r\Delta x_{d_s}}(n)\right]^2} \quad (7)$$

For each storm event and station, the peak positive and peak negative deviations are defined as:

$$r\Delta x^{+}_{u;d_s} = \max_n\left[r\Delta x_{u;d_s}(n)\right], \quad r\Delta x^{-}_{u;d_s} = \min_n\left[r\Delta x_{u;d_s}(n)\right] \quad (8)$$

These peak values are subsequently used to compare storm responses across geomagnetic storm intensity classes (G2, G3, G4) and seasons.

3. Results and Discussion

This section presents the analysis of ionospheric TEC response over Türkiye during the 14 geomagnetically disturbed days identified in Table 2. The geomagnetic conditions characterizing each event are first examined through the Kp, Dst and SYM-H indices (Figures 2 and 3). The storm-time IONOLAB-TEC estimates and the scaled quiet-day reference are then compared for the most intense event of the study period (Figure 4), followed by a network-wide characterization of the

normalized TEC deviation $r\Delta TEC$ (%) across all 14 events (Figure 5). The pre-storm scaling factors, which quantify the seasonal and solar activity differences between each storm day and the quiet reference day, are presented in Figure 6. Finally, the statistical distribution of peak positive and negative ionospheric responses is assessed as a function of storm intensity class and season (Figure 7).

Figure 2 presents the Kp and Dst indices for the 14 selected geomagnetically disturbed days alongside the quiet reference day (07 May 2022) over the period 2019–2023. The selected events span the deep minimum of Solar Cycle 24 and the ascending phase of Solar Cycle 25, with only one event recorded in 2019 (14 May 2019, G2) and no events meeting the Kp > 6 criterion in 2020, reflecting the historically low geomagnetic activity level during the SC24/SC25 transition minimum. Activity progressively increased from 2021 onward, consistent with the rising phase of SC25, with the most intense events concentrated in early 2023.

Of the 14 events, eight are classified as G2 ($Kp_{max} = 6.3 - 6.6$), three as G3 ($Kp_{max} = 7.0 - 7.7$) and three as G4 ($Kp_{max} = 8.0 - 8.3$). The Dst index reinforces this classification: the G2 storms produce minimum Dst values ranging from -18 nT to -85 nT, while the G3 and G4 events yield substantially deeper depressions, with the most intense event, 23 April 2023 ($Kp_{max} = 8.3$, G4), reaching a Dst minimum of -165 nT and the consecutive event on 24 April 2023 attaining the deepest depression of the entire study period at -213 nT. The March–April 2023 sequence is particularly noteworthy, as four G3–G4 class storms occurred within a span of 32 days, indicative of a period of elevated solar activity near the SC25 maximum.

A notable exception is the 03 November 2021 event, which satisfies the Kp > 6 criterion ($Kp_{max} = 6.3$, G2) yet the Dst index does not drop below -30 nT throughout the day, with a minimum of only -18 nT. This discrepancy suggests that the ring current enhancement associated with this event was relatively weak despite the elevated Kp, likely reflecting a storm driven primarily by substorm-related auroral currents rather than a sustained ring current injection. Accordingly, storm onset for this event is defined by the Dst minimum hour rather than the standard -30 nT threshold, as described in Section 2.1. The seasonal distribution of events, with seven occurring in spring, two in autumn, two in summer, one in winter and two spanning the summer/autumn transition, reflects the well-known Russell–McPherron effect, whereby the southward component of the interplanetary magnetic field is statistically enhanced near the equinoxes, increasing the geoeffectiveness of solar wind structures (Russell & McPherron, 1973). The quiet reference day (07 May 2022) exhibits Kp values not exceeding 1.66 throughout the day and Dst values remaining within the range -10 to -1 nT, confirming its suitability as a geomagnetically undisturbed baseline for the normalization procedure.

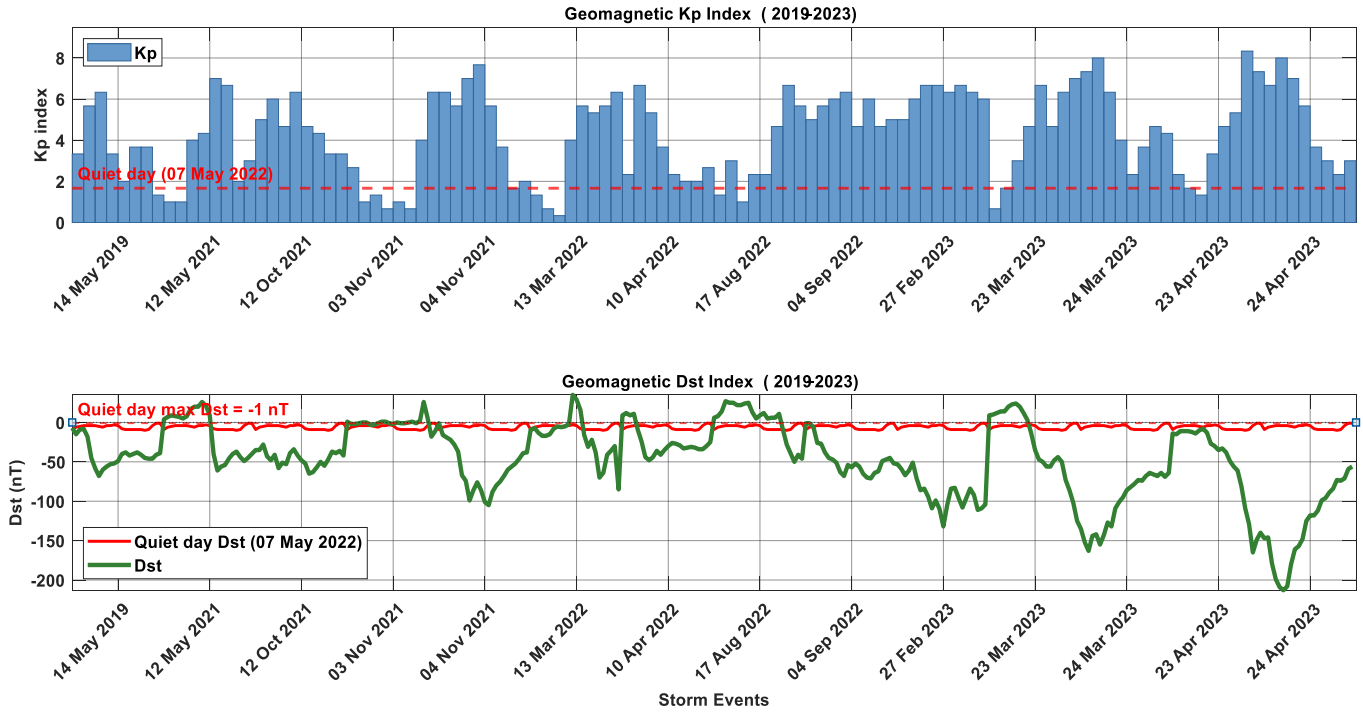

Figure 2. Kp (top panel) and Dst (bottom panel) indices for the geomagnetically disturbed days and one quiet day between 2019 and 2023.

Figure 3 presents the SYM-H index at 1-minute resolution for the same 14 disturbed days and the quiet reference day. Compared to the hourly Dst shown in Figure 2, the SYM-H index reveals finer temporal structure in the storm

development, particularly during the sudden storm commencement (SSC) and the main phase onset. For the G4 events of March–April 2023, the SYM-H time series shows rapid main phase deepening rates, with the 23 April 2023 event exhibiting a decrease of approximately 130 nT within a few hours following onset near 12:00 UT and the 24 April 2023 event reaching a minimum SYM-H of -213 nT, the deepest value recorded in the study period. The high cadence of SYM-H also captures brief positive excursions during the initial phase of several events, most notably in the 12 May 2021 and 10 April 2022 storms, reflecting sudden commencement signatures associated with interplanetary shock arrival. For the 03 November 2021 event, consistent with the Dst analysis, the SYM-H trace remains close to baseline throughout the day, with only a modest perturbation in the late evening hours, further supporting the interpretation that this event represents a weak ring current response. The quiet reference day SYM-H values fluctuate within ±10 nT, confirming the absence of any significant geomagnetic disturbance.

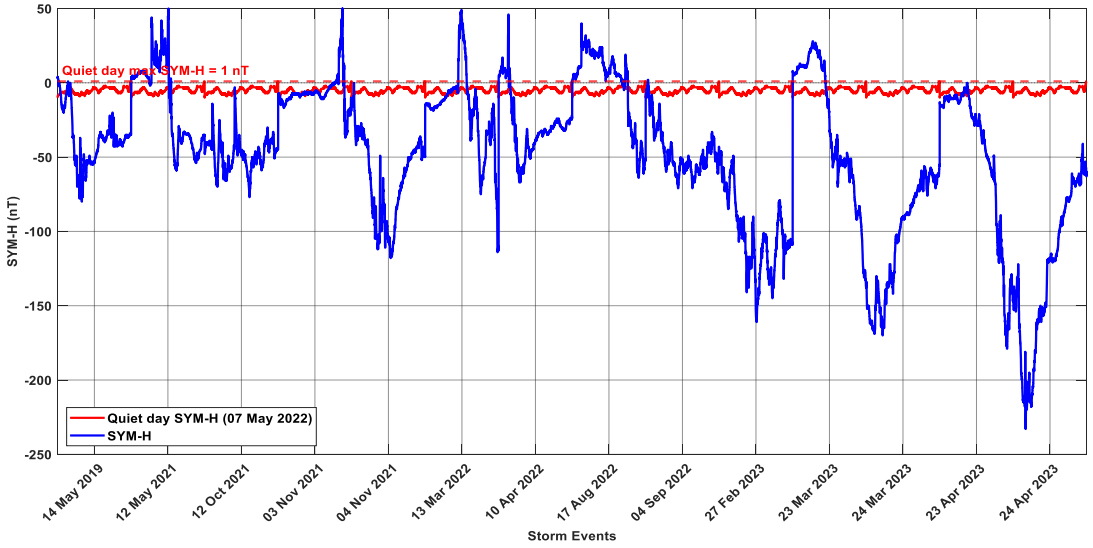

Figure 3. SYM-H index for the geomagnetically disturbed days and one quiet day between 2019 and 2023.

Figure 4 compares the storm-time IONOLAB-TEC ($\boldsymbol{x}_{u;d_s}$, solid blue) with the scaled quiet-day reference ($\boldsymbol{x}^{ref}_{u;d_s}$, dashed red) for all nine stations during the 23 April 2023 geomagnetic storm (G4, $Kp_{max} = 8.3$). Prior to storm onset at approximately 12:00 UT, the two curves are in close agreement across the entire network, validating the pre-storm scaling approach. Following onset, a network-wide positive deviation is initially observed, followed by a transition to predominantly negative values in the post-onset hours, yielding a peak positive $r\Delta TEC$ of +20.5% and a peak negative of −30.9% (Table 3). The negative phase dominates the remainder of the day, with a total negative-phase duration of 13.9 hours compared to only 10.1 hours of positive phase, the most negative-phase-dominant event in the study period despite its G4 classification. This apparently paradoxical result, whereby the most intense storm by Kp does not produce the largest positive TEC enhancement, is consistent with the well-established dependence of the ionospheric storm response on the local time of onset. The storm on 23 April 2023 commenced near local noon over Türkiye (12:00 UT ≈ 14:00–15:00 LT), a timing that favors the composition-driven negative phase over the electric field-driven positive phase, since the disturbance dynamo electric fields that produce TEC enhancements are most effective during post-midnight and morning hours (Fejer & Scherliess, 1997). In contrast, the consecutive event of 24 April 2023, which commenced near midnight (onset_h ≈ 00:00 UT), produced a peak positive $r\Delta TEC$ of +167.6% and a positive phase duration of 19.3 hours, directly illustrating the onset local-time control on storm phase dominance. The supplementary figures for the remaining 13 events confirm this pattern across the full event set.

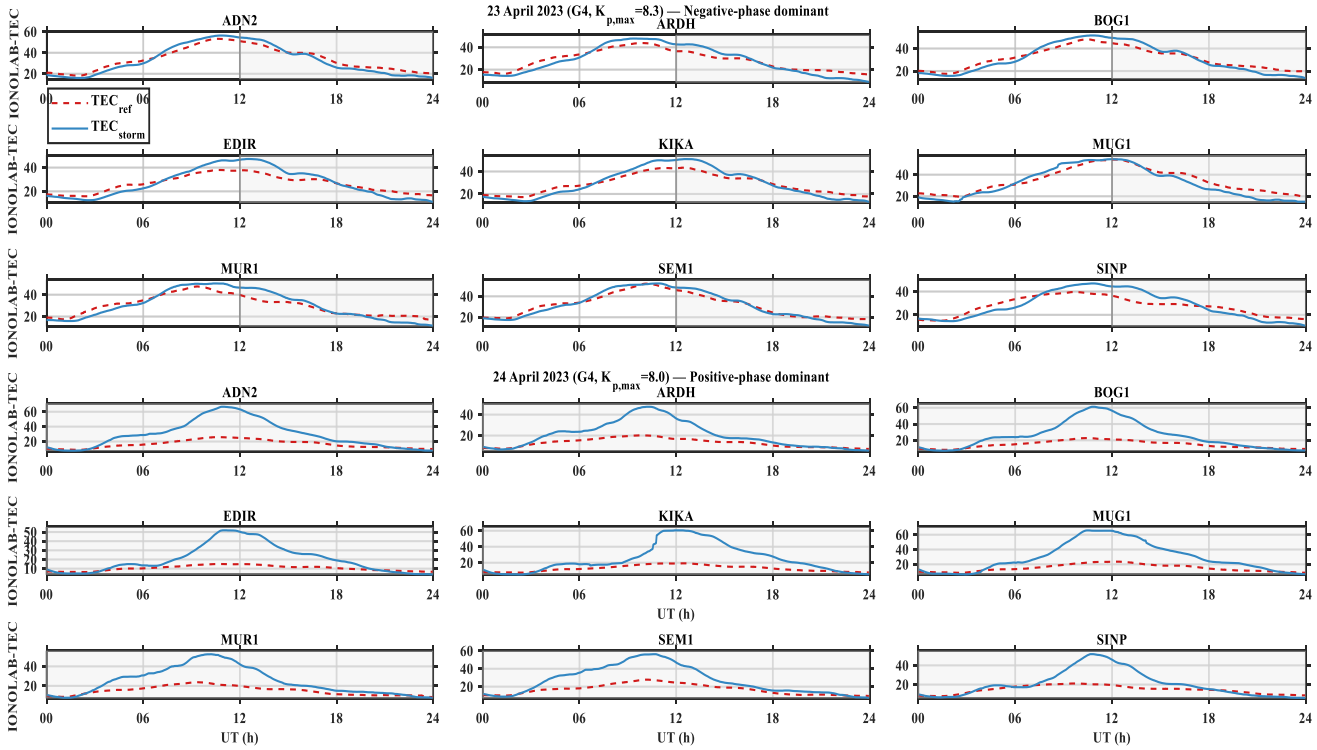

Figure 4. Comparison of storm-time IONOLAB-TEC (TEC_{storm}, solid blue) and scaled quiet-day reference IONOLAB-TEC (TEC_{ref}, dashed red) for the nine GNSS stations during two consecutive G4 geomagnetic storms illustrating contrasting storm phase dominance. Upper panels: 23 April 2023 (G4, Kpmax = 8.3), a negative-phase-dominant event with storm onset near local noon (~12:00 UT). Lower panels: 24 April 2023 (G4, Kpmax = 8.0), a positive-phase-dominant event with storm onset near local midnight (~00:00 UT). Grey shading indicates the post-onset period and the vertical grey line marks the storm onset in each panel. The contrasting behaviors of these consecutive events, which differ only in onset local time, directly illustrate the dominant role of onset timing in controlling ionospheric storm phase dominance.

Table 3. Summary statistics of the ionospheric storm response for each event.

Date	Class	Season	Peak $r\Delta TEC^{+}$ (%)	Peak $r\Delta TEC^{-}$ (%)	Dur^{+} (h)	Dur^{-} (h)	k (mean ± σ)
14 May 2019	G2	Spring	+28.9	−26.1	13.2	10.8	0.469 ± 0.044
12 May 2021	G3	Spring	+64.6	−19.8	11.1	12.9	0.533 ± 0.048
12 Oct 2021	G2	Autumn	+41.0	−25.6	12.3	11.7	0.526 ± 0.051
03 Nov 2021	G2	Autumn	+34.8	−31.2	14.1	9.9	0.465 ± 0.034
04 Nov 2021	G3	Autumn	+118.7	−21.7	20.0	4.0	0.504 ± 0.052
13 Mar 2022	G2	Spring	+31.6	−33.7	12.9	11.1	0.717 ± 0.062
10 Apr 2022	G2	Spring	+41.3	−33.6	12.6	11.4	0.913 ± 0.080
17 Aug 2022	G2	Summer	+27.7	−16.4	13.4	10.6	0.857 ± 0.070
04 Sep 2022	G2	Autumn	+30.3	−15.7	18.8	5.2	0.757 ± 0.086
27 Feb 2023	G2	Winter	+197.4	−32.8	21.0	3.0	0.644 ± 0.079
23 Mar 2023	G3	Spring	+42.4	−41.8	10.2	13.8	1.372 ± 0.119
24 Mar 2023	G4	Spring	+140.9	−55.3	12.7	11.3	0.762 ± 0.103
23 Apr 2023	G4	Spring	+20.5	−30.9	10.1	13.9	1.184 ± 0.126
24 Apr 2023	G4	Spring	+167.6	−25.2	19.3	4.7	0.560 ± 0.071

Peak positive and peak negative $r\Delta TEC$ values represent network-mean maxima and minima, respectively. Phase durations are computed as the total time (hours) for which the network-mean $r\Delta TEC$ remains positive or negative. The pre-storm scaling factor k is reported as the mean ± standard deviation across the nine stations.

Figure 5 presents the network-averaged normalized TEC deviation $\overline{r\Delta x_{d_s}}(n)$ with ±1σ envelope for all 14 storm events. Several key features emerge from a systematic inspection of the panels. First, positive storm phases dominate the daytime hours in the majority of events, but the magnitude varies by more than an order of magnitude across the study period. The most

extreme positive deviations are recorded on 27 February 2023 (G2, Winter; peak +197.4%) and 24 April 2023 (G4, Spring; peak +167.6%), while the weakest positive response is observed on 17 August 2022 (G2, Summer; peak +27.7%) and 23 April 2023 (G4, Spring; peak +20.5%). This range illustrates that storm intensity class alone is a poor predictor of TEC enhancement magnitude and that onset timing, season and solar activity level all contribute substantially to the observed response. The anomalously large positive deviation of +197.4% on 27 February 2023 warrants particular attention. This event, despite being classified as G2 ($Kp_{max} = 6.6$), occurred in winter with a storm that was already in progress at 00:00 UT (Dst < -30 nT from the start of the observational window), yielding a k-scale factor of 0.644. The low k value reflects the depressed winter ionosphere over Türkiye relative to the May quiet reference day, so that even a moderate positive TEC perturbation appears amplified when expressed as a percentage relative to the scaled reference. This result highlights both the physical role of seasonal background TEC in modulating the apparent storm response magnitude and a methodological sensitivity of the $r\Delta TEC$ metric to events where the storm onset precedes the observational window, a limitation acknowledged for the four events (12 October 2021, 27 February 2023, 24 March 2023, 24 April 2023) for which the one-hour fallback scaling window was applied.

Second, the negative storm phase is most prominent and sustained in the March–April 2023 G3–G4 sequence. The 24 March 2023 event (G4) produces the deepest network-mean negative deviation of the entire study period at -55.3%, with a negative-phase duration of 11.3 hours. The 23 March 2023 event (G3), which preceded it by one day, also exhibits a pronounced negative phase (-41.8%, 13.8 hours), suggesting that residual thermospheric composition changes from the 23 March event may have preconditioned the ionosphere for a deeper negative response on 24 March. Such storm-on-storm compositional conditioning has been documented in previous multi-day storm sequences (Prölss, 1995).

Third, the 04 November 2021 event (G3, Autumn) stands out with an exceptionally long positive phase duration of 20.0 hours and a peak $r\Delta TEC$ of +118.7%, with a correspondingly short negative phase of only 4.0 hours. The storm onset occurred at approximately 05:00 UT (≈ 07:00–08:00 LT over Türkiye), placing it in the early morning sector where prompt penetration electric fields are known to produce sustained daytime positive phases over mid-latitudes (Tsurutani, et al., 2004). The ±1σ envelope is notably narrow for this event compared to the G4 storms, suggesting a spatially coherent positive response across the Anatolian network.

Fourth, the 03 November 2021 event (G2, Autumn; panel d) is the only event in the study period for which the Dst index did not reach the -30 nT threshold, with a minimum Dst of only -18 nT. Despite this weak ring current signature, the ionospheric TEC response is non-negligible at the network level, with a peak positive deviation of +34.8% and a peak negative deviation of -31.2%. The positive phase (14.1 h) dominates, suggesting that magnetospheric energy input via mechanisms other than the symmetric ring current, such as substorm-driven prompt penetration electric fields, may have contributed to the observed TEC enhancement even in the absence of a pronounced main-phase Dst depression. The retention of this event in the analysis is justified on three grounds. First, the event selection criterion adopted in this study is based exclusively on the maximum 3-hourly Kp index exceeding 6, a threshold that this event satisfies (Kpmax = 6.3). Excluding it post hoc on the basis of the Dst threshold would introduce an inconsistency in the selection procedure and constitute a form of confirmation bias toward events with strong ring current signatures. Second, the Kp-Dst decoupling observed here is a well-documented phenomenon in the literature: intense substorm activity can drive Kp to high values through auroral electrojet enhancement without necessarily producing a sustained symmetric ring current injection sufficient to depress Dst below -30 nT (Gonzalez, et al., 1994; Matzka, et al., 2021). This event therefore represents a physically distinct class of geomagnetic disturbance that is legitimately captured by the Kp-based selection criterion. Third, the ionospheric TEC response to this event is non-negligible, with a network-mean peak positive deviation of +34.8% and a peak negative deviation of -31.2%, confirming that magnetospheric energy input, likely via substorm-driven prompt penetration electric fields, did reach the mid-latitude ionosphere over Türkiye despite the weak ring current signature.

Figure 6 presents the pre-storm scaling factor $k_{u;d_s}$ for all station–event pairs. The heatmap reveals two distinct and physically interpretable patterns: a solar cycle trend along the horizontal axis and a seasonal modulation within each year. Regarding the solar cycle trend, all events from 2019 to mid-2021 yield k values in the range 0.46–0.53, well below unity, indicating that the pre-storm TEC background during these SC24-minimum years was roughly half that of the May 2022 quiet reference day. This is consistent with the substantially reduced solar EUV flux during the SC24/SC25 transition minimum, which suppressed photo-ionization rates and depressed the background ionospheric plasma density (Huang, et al., 2016; Liu, et al., 2006). By 2022, k values rise to 0.72–0.91, reflecting the increasing solar flux during the ascending phase of SC25. In early 2023, two events (23 March 2023, $k = 1.372$; 23 April 2023, $k = 1.184$) yield k values exceeding unity, meaning that the pre-storm TEC on those days was already higher than the May 2022 quiet reference, a consequence of the elevated solar activity near the SC25 maximum, which had surpassed the activity level of the reference day by early 2023.

The inter-station spread of k within a given event is small ($\sigma_k = 0.036 - 0.134$, Table 3), confirming spatial coherence of the background TEC across the Anatolian network at the pre-storm timescale. The largest inter-station spread occurs for the 23 March 2023 event ($\sigma_k = 0.126$) and 23 April 2023 ($\sigma_k = 0.134$), both during the late-storm-sequence period when the ionosphere may have been spatially non-uniform due to preceding geomagnetic activity.

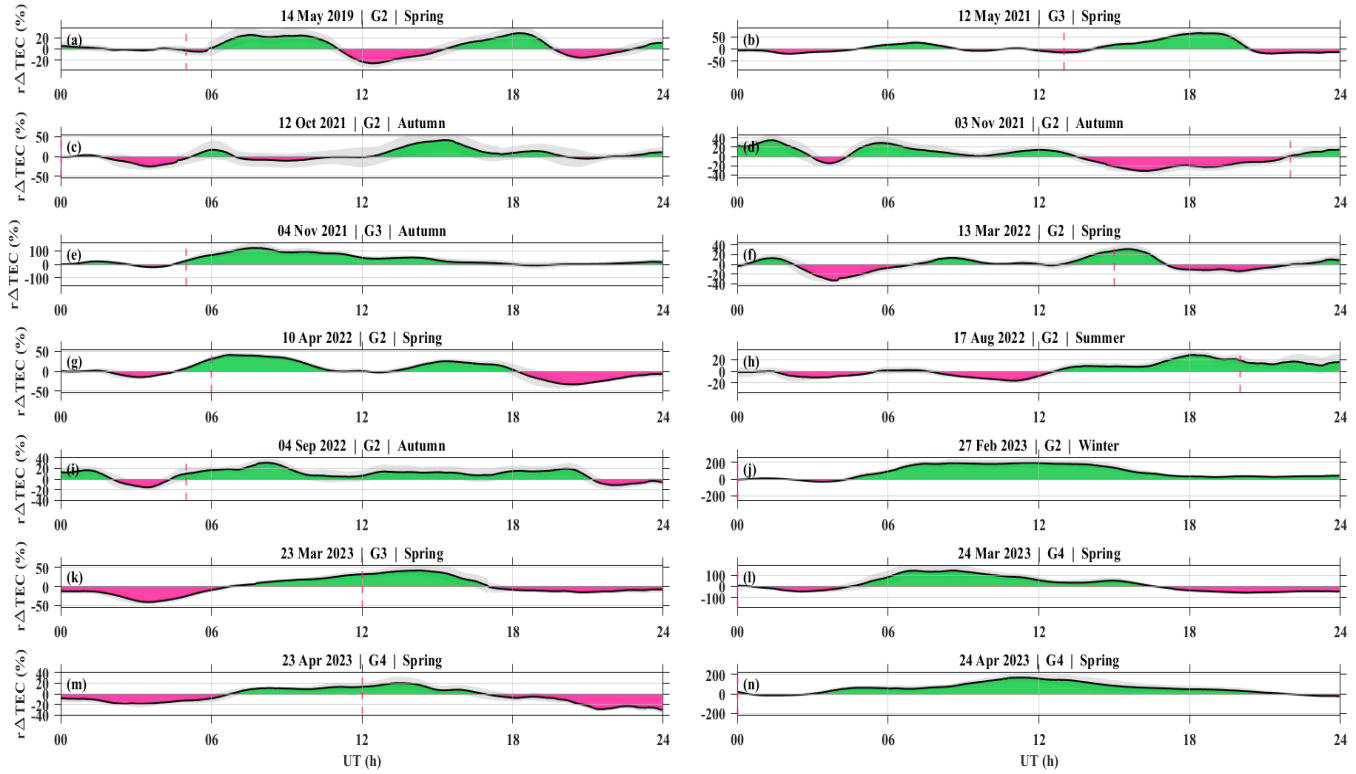

Figure 5. Normalized IONOLAB-TEC deviation, $r\Delta TEC$ (%), for all 14 storm events, computed as the network mean over nine stations (solid black line) with ±1σ envelope (grey shading). Green and red shadings denote positive and negative ionospheric storm phases, respectively. The red dashed vertical line marks the storm onset in each panel.

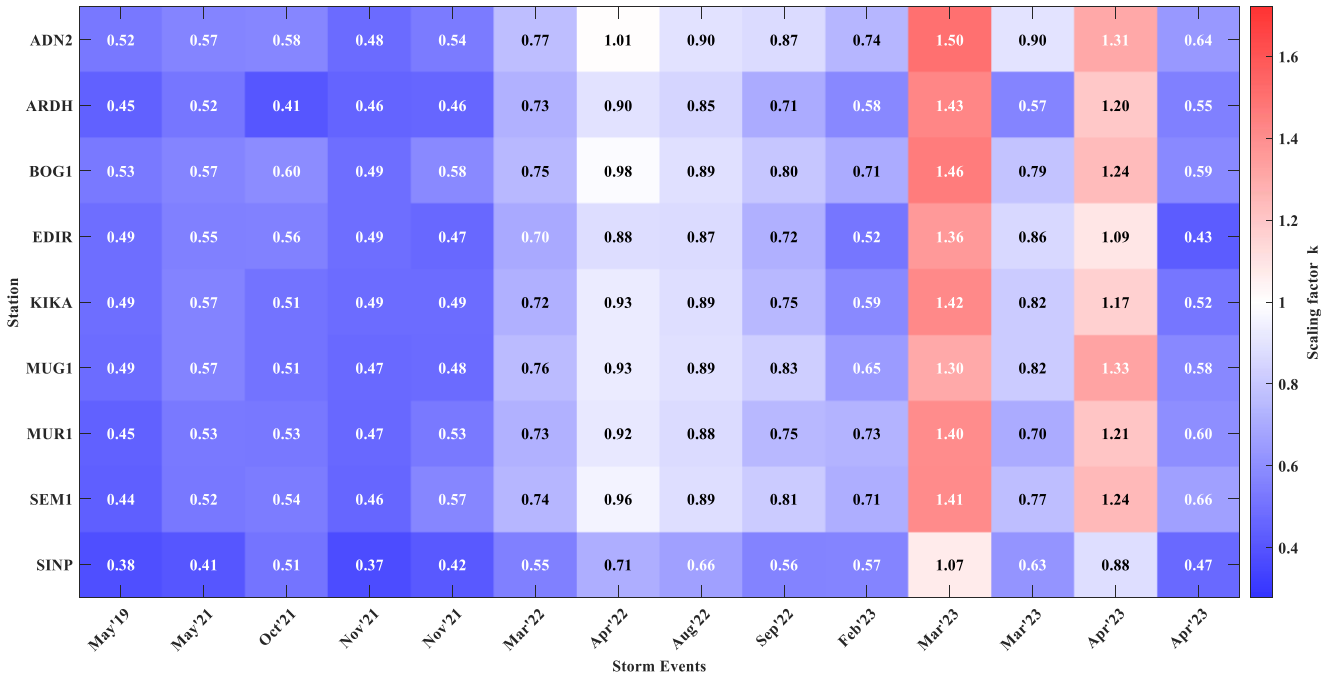

Figure 6. Pre-storm scaling factor k for each station–event pair. Values greater than 1 indicate higher TEC background during the storm day relative to the quiet reference day (07 May 2022), reflecting seasonal and solar activity differences.

The robustness of the single quiet reference day approach is further supported by the pre-storm agreement observed across the supplementary figures (Figures S1–S13). In each event, the storm-time IONOLAB-TEC and the scaled quiet-day reference converge closely during the pre-onset window, confirming that the scaling factor k effectively absorbs the seasonal and solar-cycle differences in background TEC regardless of the reference day chosen. While a formal sensitivity analysis using alternative quiet days would require additional IONOLAB-TEC retrievals beyond the scope of the present study, the physical consistency of k with independently known solar EUV trends across SC24-SC25 (Huang, et al., 2016; Liu, et al., 2006) provides implicit validation of the normalization procedure. The acknowledged limitation of the percentage-based $r\Delta TEC$ metric for low-k events (2019–2021) does not affect the qualitative characterization of storm phase polarity or duration, which are the primary observational quantities reported herein.

The systematic underestimation of k for the 2019–2021 events has a direct implication for the $r\Delta TEC$ metric: since $TEC_{ref} = k \cdot \boldsymbol{x}_{u;d_q}$ is scaled to a low baseline for these early events, any given absolute TEC perturbation translates into a larger percentage deviation than it would for a 2022–2023 event with a higher background. This cross-cycle asymmetry should be borne in mind when interpreting peak $r\Delta TEC$ values across events from different phases of the solar cycle and underscores the utility of the pre-storm scaling approach adopted in Section 2.1, which anchors the normalization to the observed pre-storm TEC level rather than to a fixed solar activity proxy.

Figure 7 presents the statistical distribution of the peak positive and peak negative deviations across all nine stations, stratified by storm intensity class (panels a–b) and season (panels c–d). Storm intensity dependence (panels a–b): A statistically meaningful progression with storm class is observed for the positive phase: the median peak positive $r\Delta TEC$ increases from +37.1% for G2 events to +66.8% for G3 and +140.1% for G4 and the mean values follow the same ordering (+59.1%, +78.8%, +114.7%). The interquartile range widens substantially from G2 to G4, reflecting the greater event-to-event and station-to-station variability during intense storms. For the negative phase (panel b), the class ordering is less monotonic: G2 events yield a median peak of -31.4%, G3 events -26.0% and G4 events -34.9%. The comparatively shallow G3 negative median is influenced by the 04 November 2021 event, which had an exceptionally dominant positive phase and a very short negative phase (4.0 h), pulling the G3 distribution upward. The wide spread of the G4 box reflects the contrasting behavior of the three G4 events: 24 March 2023 produced the deepest negative phase (-55.3%), while 24 April 2023 produced only -25.2%, with 23 April 2023 intermediate at -30.9%.

It should be noted that the seasonal groups are unequally sampled: spring comprises seven events (n=63 station-event pairs), while summer and autumn each comprise two events (n=18) and winter only one event (n=9). Accordingly, seasonal interpretations for the summer, autumn and winter groups should be treated as indicative rather than statistically definitive and the spring group provides the most robust seasonal characterization. Seasonal dependence (panels c–d): The positive phase analysis (panel c) reveals that winter events exhibit the highest median positive peak (+189.2%), followed by spring (+46.1%), autumn (+41.6%) and summer (+29.6%). However, the winter median is dominated by the single 27 February 2023 event (+197.4%), and the associated box spans an exceptionally wide range due to the combination of the large percentage deviation and the low background TEC discussed in the context of Figure 6. Spring events, by contrast, show the broadest seasonal sample (seven events) and a more representative median. The relatively weak positive response in summer is consistent with the lower occurrence probability of positive ionospheric storms during solstitial periods over mid-latitudes, where the thermospheric composition is less favorable for density enhancements driven by equatorward neutral winds (Mendillo, 2006; Prölss, 1993).

For the negative phase (panel d), spring produces the deepest median (-33.9%) and winter the deepest mean (-38.2%), while summer shows the weakest negative response (median -19.7%). This seasonal ordering is consistent with the greater susceptibility of the spring and winter ionosphere to negative-phase composition changes, where the increased O/N_2 depletion driven by storm-time Joule heating and Lorentz forcing at high latitudes propagates equatorward more efficiently during winter and spring due to the prevailing thermospheric circulation patterns (Fuller-Rowell, et al., 1994). The summer suppression of both phases is in agreement with findings from previous studies of mid-latitude ionospheric storms in the Eastern Mediterranean and Balkan region (Karatay, et al., 2017; Karatay, 2020a; Karatay, 2020b; Karatay, 2020c).

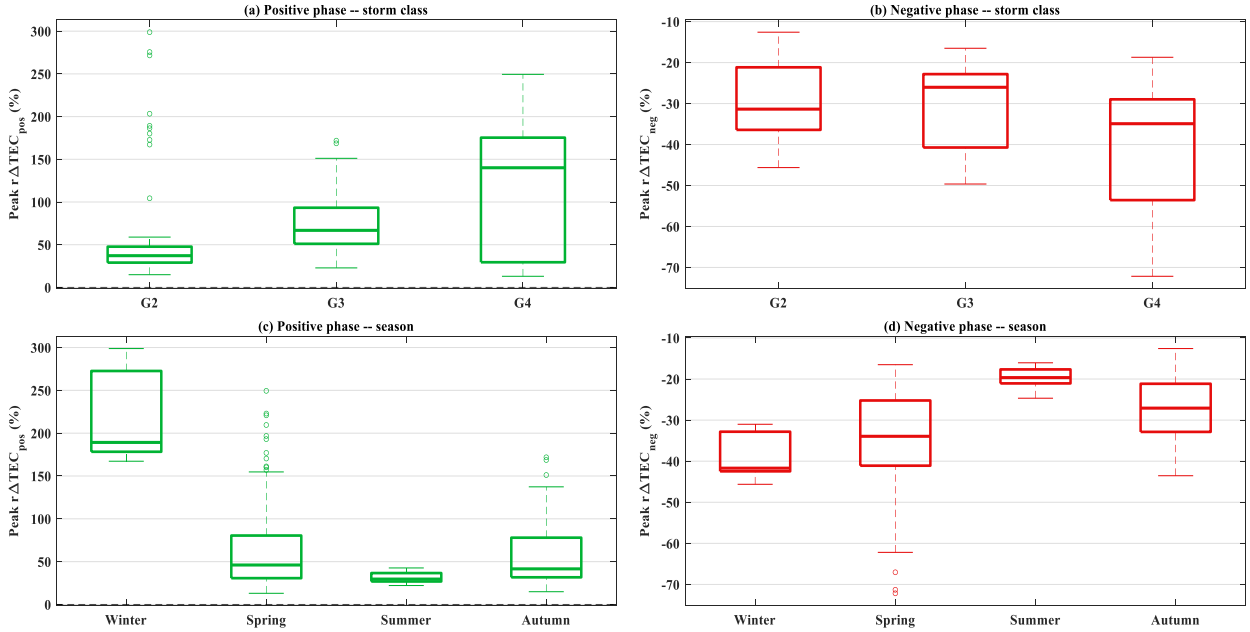

Figure 7. Box plots of peak positive (a, c) and peak negative (b, d) $r\Delta TEC$ (%) grouped by storm intensity class (a, b) and season (c, d). Each box represents the distribution across all nine stations within the group. The number of station-event data points contributing to each box is as follows, storm class: G2: n=72, G3: n=27, G4: n=27; season: Spring: n=63, Summer: n=18, Autumn: n=18, Winter: n=9. Whiskers extend to 1.5 times the interquartile range.

Collectively, the results presented in this section demonstrate that the ionospheric response over Türkiye during geomagnetic storms is governed by a complex interplay of storm intensity, onset local time, season and background solar activity level, none of which acts independently. While storm intensity class provides a first-order indicator of the expected TEC perturbation magnitude, with G4 events producing median peak positive deviations approximately four times larger than G2 events, the wide intra-class variability observed in both the positive and negative phases confirms that Kp or storm class alone is insufficient to characterize the ionospheric storm response at a specific location. The onset local time emerges as a particularly critical modulator, as illustrated by the contrasting behavior of the consecutive 23 and 24 April 2023 G4 events, where a difference of approximately 12 hours in onset timing reversed the dominant storm phase from negative to positive. Seasonal effects further modulate the response through changes in thermospheric composition, background plasma density and the efficiency of prompt penetration electric fields, with spring events producing the most pronounced and consistent positive phases over the Anatolian network. The pre-storm scaling analysis reveals a clear solar cycle imprint on the background TEC, with k values increasing from approximately 0.47 during the SC24 minimum to above 1.3 during the SC25 ascending phase, a factor that directly influences the apparent magnitude of normalized TEC deviations and must be accounted for in any multi-year comparative study. Taken together, these findings provide a comprehensive observational baseline for mid-latitude ionospheric storm morphology over Türkiye during the SC24–SC25 transition period and highlight the value of spatially distributed GNSS networks combined with observation-based normalization for characterizing storm-time ionospheric variability.

4. Conclusion

This study provides a detailed characterization of the ionospheric storm response over Türkiye during 14 geomagnetically disturbed days (G2–G4 class) between January 2019 and June 2023, using high-resolution IONOLAB-TEC estimates derived from nine TNPGN-Active GNSS stations. By applying an observation-driven pre-storm scaling procedure anchored to a single quiet reference day (07 May 2022), the analysis successfully isolated storm-induced TEC deviations while effectively accounting for seasonal and solar-cycle differences in background ionization levels across the SC24 minimum to SC25 ascending phase transition.

The results demonstrate that the mid-latitude ionosphere over the Anatolian region exhibits highly variable responses governed by a complex interplay of multiple drivers. Storm intensity (Kp/Dst) offers a first-order control on the magnitude of perturbations, with G4 events generally producing larger peak positive deviations than G2 events. However, intra-class variability is substantial, underscoring that geomagnetic indices alone are insufficient predictors. The local time of storm onset emerges as a dominant modulator: events commencing near local noon favor composition-driven negative phases, whereas midnight-to-morning onsets promote prolonged electric field-driven positive phases, as clearly illustrated by the contrasting behaviors of the consecutive 23 and 24 April 2023 G4 storms.

Seasonal effects further shape the response, with spring events showing the most consistent and pronounced positive phases, winter conditions amplifying relative enhancements due to lower background TEC and summer periods suppressing both phases due to unfavorable thermospheric composition.

The pre-storm scaling factor analysis reveals a clear solar-cycle imprint, with background TEC roughly doubling from the deep SC24 minimum (2019–mid-2021) to the more active early SC25 period (2022–2023). This background modulation directly influences the apparent percentage deviations ($r\Delta TEC$), highlighting the importance of observation-based normalization over reliance on fixed solar proxies in multi-year studies. Network-averaged statistics and phase-duration metrics further confirm spatial coherence across the nine stations while capturing regional gradients over nearly 18° of longitude in the Eastern Mediterranean sector. These findings contribute to a better understanding of mid-latitude ionospheric dynamics in a longitude sector that has been relatively underrepresented in global storm-time statistics. Practically, the observed TEC perturbations and their dependence on onset timing and season have direct implications for GNSS error mitigation, precise positioning and space weather forecasting services in Türkiye and surrounding regions. As Solar Cycle 25 progresses toward its maximum, the frequency of intense geomagnetic events is expected to rise, increasing the operational relevance of such regional benchmarks.

Future work could extend this analysis by incorporating additional TNPGN-Active stations for finer spatial resolution, integrating ionosonde and satellite data for multi-instrument validation, or developing empirical models that incorporate onset local time and pre-storm background as explicit inputs. Overall, this study demonstrates the value of dense, continuously operating GNSS networks combined with robust normalization techniques for advancing both scientific insight and practical space weather applications in mid-latitude regions.

Conflict of Interest

The authors declare that they have no conflict of interest.

Disclosure of Generative AI Use

The authors used a generative artificial intelligence (AI) tool solely to assist in improving the language and drafting of the Introduction section of this manuscript. The AI tool was not used for study design, data collection, data analysis, interpretation of results, or the generation of scientific conclusions. All content was carefully reviewed, revised where necessary, and approved by the authors, who take full responsibility for the final content of the manuscript.

References

Akala, A., Afolabi, R., & Otsuka, Y. (2023). Responses of the African-European equatorial-, low-, mid-, and high-latitude ionosphere to geomagnetic storms of 2013, 2015 St Patrick's Days, 1 June 2013, and 7 October 2015. *Advances in Space Research*, *72*(3), 775-789. https://doi.org/10.1016/j.asr.2022.10.029

Arikan, F., Erol, C. B., & Arikan, O. (2003). Regularized estimation of vertical total electron content from Global Positioning System data. *Journal of Geophysical Research: Space Physics*, *108*(A12), 1-20. https://doi.org/10.1029/2002JA009605

Arikan, F., Nayir, H., Sezen, U., & Arikan, O. (2008). Estimation of single station interfrequency receiver bias using GPS-TEC. *Radio Science*, *43*(4), 1-13. https://doi.org/10.1029/2007RS003785

Arikan, F., Shukurov, S., Tuna, H., Arikan, O., & Gulyaeva, T. (2016). Performance of GPS slant total electron content and IRI-Plas-STEC for days with ionospheric disturbance. *Geodesy and Geodynamics*, *7*(1), 1-10. https://doi.org/10.1016/j.geog.2015.12.009

Campuzano, S., Delgado-Gómez, F., Migoya-Orué, Y., Rodríguez-Caderot, G., Herraiz-Sarachaga, M., & Radicella, S. (2023). Study of ionosphere irregularities over the iberian peninsula during two moderate geomagnetic storms using GNSS and ionosonde observations. *Atmosphere*, *14*(2), 1-16. https://doi.org/10.3390/atmos14020233

Doğanalp, S., & Köz, İ. (2024). Monitoring ionospheric and atmospheric conditions during the 2023 Kahramanmaraş earthquake period. *Atmosphere*, *15*(12), 1542. https://doi.org/10.3390/atmos15121542

Erken, F., Karatay, S., & Cinar, A. (2019). Spatio-temporal prediction of ionospheric total electron content using an adaptive data fusion technique. *Geomagnetism and Aeronomy*, *59*, 971-979. https://doi.org/10.1134/S001679321908005X

Fagundes, P. R., Cardoso, F. A., Fejer, B. G., Venkatesh, K., Ribeiro, B. A., & Pillat, V. G. (2016). Positive and negative GPS-TEC ionospheric storm effects during the extreme space weather event of March 2015 over the Brazilian sector. *Journal of Geophysical Research: Space Physics*, *121*(6), 5613-5625. https://doi.org/10.1002/2015JA022214

Fejer, B. G., & Scherliess, L. (1997). Empirical models of storm time equatorial zonal electric fields. *Journal of Geophysical Research: Space Physics*, *102*(A11), 24047-24056. https://doi.org/10.1029/97JA02164

Fuller-Rowell, T. J., Codrescu, M. V., & R. J. Moffett, S. Q. (1994). Response of the thermosphere and ionosphere to geomagnetic storms. *Journal of Geophysical Research: Space Physics*, *99*(A3), 3893-3914. https://doi.org/10.1029/93JA02015

GFZ. (1956). *GFZ helmholtz centre for geosciences*. Retrieved Aug 04, 2025, from https://www-app3.gfz-potsdam.de/kp_index/Kp_ap_since_1932.txt

Ghafar, M. M., Mohammed, D. H., Salh, H., Dleer, S., & Külahcı, S. M. (2024). Ionospheric Whispers of the Earth's tremors: Decoding TEC Mysteries in the East Anatolian Fault Zone. *Geomagnetism and Aeronomy*, *64*, 772-780. https://doi.org/10.1134/S0016793223600960

Gonzalez, W. D., Joselyn, J. A., Kamide,Y. H., Kroehl,W., Rostoker,G., Tsurutani,B. T., & Vasyliunas, V. M. (1994). What is a geomagnetic storm? *Journal of Geophysical Research: Space Physics*, *99*(A4), 5771-5792. https://doi.org/10.1029/93JA02867

Gulyaeva, T. L., Arikan, F., Hernandez-Pajares, M., & Veselovsky, I. S. (2014). North-south components of the annual asymmetry in the ionosphere. *Radio Science*, *49*(7), 485-496. https://doi.org/10.1002/2014RS005401

Gulyaeva, T., & Stanislawska, I. (2005). Night−day imprints of ionospheric slab thickness during geomagnetic storm. *Journal of Atmospheric and Solar-Terrestrial Physics*, *67*(14), 1307-1314. https://doi.org/10.1016/j.jastp.2005.07.006

Hajra, R., Franco, A. M., Echer, E., & Bolzan, M. J. (2021). Long-Term variations of the geomagnetic activity: A comparison between the strong and weak solar activity cycles and implications for the space climate. *Journal of Geophysical Research: Space Physics*, *126*(4), 1-14. https://doi.org/10.1029/2020JA028695

Haralambous, H., & Makrominas, M. (2024). Validation of the European Ionosonde Service nowcasting foF2 maps over the eastern Mediterranean. *Advances in Space Research*, *73*(3), 1799-1813. https://doi.org/10.1016/j.asr.2023.10.035

Hernández-Pajares, M., Juan, J. M., Sanz, J., Aragón-Àngel, À., García-Rigo, A., Salazar, D., & Escudero, M. (2011). The ionosphere: Effects, GPS modeling and the benefits for space geodetic techniques. *Journal of Geodesy*, *85*, 887-907. https://doi.org/10.1007/s00190-011-0508-5

Huang, C.-S., Foster, J. C., & Kelley, M. C. (2005). Long-duration penetration of the interplanetary electric field to the low-latitude ionosphere during the main phase of magnetic storms. *Journal of Geophysical Research: Space Physics*, *110*(A11), 1-13. https://doi.org/10.1029/2005JA011202

Huang, J., Hao, Y., Zhang, D., & Xiao, Z. (2016). Changes of solar extreme ultraviolet spectrum in solar cycle 24. *Journal of Geophysical Research: Space Physics*, *121*(7), 6844-6854. https://doi.org/10.1002/2015JA022231

Jakowski, N., Béniguel, Y., & Franceschi, G. D. (2012). Monitoring, tracking and forecasting ionospheric perturbations using GNSS techniques. *Journal of Space Weather and Space Climate*, *2*(A22), 1-14. https://doi.org/10.1051/swsc/2012022

Javaraiah, J. (2022). Long-term variations in solar activity: Predictions for amplitude and north–south asymmetry of solar cycle 25. *Solar Physics*, *297*, 33. https://doi.org/10.1007/s11207-022-01956-z

Jin, S., Jin, R., & Kutoglu, H. (2017). Positive and negative ionospheric responses to the March 2015 geomagnetic storm from BDS observations. *Journal of Geodesy*, *91*, 613-626. https://doi.org/10.1007/s00190-016-0988-4

Karatay, S. (2020a). Detection of the ionospheric disturbances on GPS-TEC using Differential Rate Of TEC (DROT) algorithm. *Advances in Space Research*, *65*(10), 2372-2390. https://doi.org/10.1016/j.asr.2020.01.042

Karatay, S. (2020b). Estimation of frequency and duration of ionospheric disturbances over Turkey with IONOLAB-FFT algorithm. *Journal of Geodesy*, *94*, 89. https://doi.org/10.1007/s00190-020-01416-1

Karatay, S. (2020c). Temporal variations of the ionospheric disturbances due to the seasonal variability over Turkey using IONOLAB-FFT algorithm. *Geodesy and Geodynamics*, *11*(3), 182-191. https://doi.org/10.1016/j.geog.2019.12.002

Karatay, S., Cinar, A., & Arikan, F. (2017). Ionospheric responses during equinox and solstice periods over Turkey. *Advances in Space Research*, *60*(9), 1958-1967. https://doi.org/10.1016/j.asr.2017.07.038

Koroglu, M., & Arikan, F. (2025). Statistical analysis of regional STEC gradient trends for midlatitude ionosphere. *Geodesy and Geodynamics*, *16*(1), 7-28. https://doi.org/10.1016/j.geog.2024.04.006

Lei, J., Thayer, J. P., Forbes, J. M., Wu, Q., She, C., Wan, W., & Wang, W. (2008). Ionosphere response to solar wind high-speed streams. *Geophysical Research Letters*, *35*(19), 1-5. https://doi.org/10.1029/2008GL035208

Liu, L., Wan, W., Ning, B., Pirog, O. M., & Kurkin, V. I. (2006). Solar activity variations of the ionospheric peak electron density. *Journal of Geophysical Research: Space Physics*, *111*(A8), 1-13. https://doi.org/10.1029/2006JA011598

Lu, G., Richmond, A. D., Emery, B. A., & Roble, R. G. (1995). Magnetosphere-ionosphere-thermosphere coupling: Effect of neutral winds on energy transfer and field-aligned current. *Journal of Geophysical Research: Space Physics*, *100*(A10), 19643-19659. https://doi.org/10.1029/95JA00766

Lyon, J. G. (2000). The solar wind-magnetosphere-ionosphere system. *Science*, *288*(5473), 1987-1991. https://doi.org/10.1126/science.288.5473.1987

Maruyama, N., Richmond, A. D., Fuller-Rowell, T. J., Codrescu, M. V., Sazykin, S., Toffoletto, F. R., Spiro, R. W., & Millward, G. H. (2005). Interaction between

direct penetration and disturbance dynamo electric fields in the storm-time equatorial ionosphere. *Geophysical Research Letters*, *32*(17), 1-4. https://doi.org/10.1029/2005GL023763

Matzka, J., Stolle, C., Yamazaki, Y., Bronkalla, O., & Morschhauser, A. (2021). The geomagnetic kp index and derived indices of geomagnetic activity. *Space Weather*, *19*(5), e2020SW002641. https://doi.org/10.1029/2020SW002641

Mendillo, M. (2006). Storms in the ionosphere: Patterns and processes for total electron content. *Reviews of Geophysics*, *44*(4), 1-47. https://doi.org/10.1029/2005RG000193

Mishin, V. M., Mishin, V. V., Kurikalova, M. A., Sapronova, L. A., & Karavaev, Y. A. (2019). Positive and negative feedbacks in the magnetosphere-ionosphere coupling. *Journal of Atmospheric and Solar-Terrestrial Physics*, *187*, 10-21. https://doi.org/10.1016/j.jastp.2019.03.002

Nakano, S., & Iyemori, T. (2005). Storm-time field-aligned currents on the nightside inferred from ground-based magnetic data at midlatitudes: Relationships with the interplanetary magnetic field and substorms. *Journal of Geophysical Research: Space Physics*, *110*(A7), 1-13. https://doi.org/10.1029/2004JA010737

Nayir, H., Arikan, F., Arikan, O., & Erol, C. B. (2007). Total electron content estimation with reg-est. *Journal of Geophysical Research: Space Physics*, *112*(A11), 1-11. https://doi.org/10.1029/2007JA012459

Paul, K. S., Haralambous, H., Moses, M., & Tripathi, S. C. (2025). Effects of the October 2024 storm over the global ionosphere. *Remote Sensing*, *17*(13), 2329. https://doi.org/10.3390/rs17132329

Pica, E., Spogli, L., Cesaroni, C., Alfonsi, L., Haralambous, H., Vallianatos, F., De Franceschi, G., Romano, V., & Marcocci, C. (2025). Assessing the ionospheric scintillations occurrence on L-band in the southern Mediterranean sector. *Advances in Space Research*, *75*(1), 837-855. https://doi.org/10.1016/j.asr.2024.10.032

Pietrella, M., Pignalberi, A., Pezzopane, M., Pignatelli, A., Azzarone, A., & Rizzi, R. (2018). A comparative study of ionospheric IRIEup and ISP assimilative models during some intense and severe geomagnetic storms. *Advances in Space Research*, *61*(10), 2569-2584. https://doi.org/10.1016/j.asr.2018.02.026

Prölss, G. W. (1993). Common origin of positive ionospheric storms at middle latitudes and the geomagnetic activity effect at low latitudes. *Journal of Geophysical Research: Space Physics*, *98*(A4), 5981-5991. https://doi.org/10.1029/92JA02777

Prölss, G. W. (1995). Ionospheric F-region storms. In H. Volland (Ed.), *Handbook of atmospheric electrodynamics* (pp. 195-248). CRC Press.

Pudovkin, M. I. (1974). Electric fields and currents in the ionosphere. *Space Science Reviews*, *16*, 727-770. https://doi.org/10.1007/BF00182599

Ren, X., Zhang, X., Xie, W., Zhang, K., Yuan, Y., & Li, X. (2016). Global ionospheric modelling using multi-GNSS: BeiDou, Galileo, GLONASS and GPS. *Scientific Reports*, *6*, 33499. https://doi.org/10.1038/srep33499

Richardson, I. G. (2013). Geomagnetic activity during the rising phase of solar cycle 24. *Journal of Space Weather and Space Climate*, *3*, 1-11. https://doi.org/10.1051/swsc/2013031

Ridley, A., Deng, Y., & Tóth, G. (2006b). The global ionosphere–thermosphere model. *Journal of Atmospheric and Solar-Terrestrial Physics*, *68*(8), 839-864. https://doi.org/10.1016/j.jastp.2006.01.008

Ridley, A., Zeeuw, D. D., Manchester, W., & Hansen, K. (2006a). The magnetospheric and ionospheric response to a very strong interplanetary shock and coronal mass ejection. *Advances in Space Research*, *38*(2), 263-272. https://doi.org/10.1016/j.asr.2006.06.010

Rishbeth, H., & Garriott, O. K. (1969). *Introduction to ionospheric physics.* Academic Press.

Russell, C. T., & McPherron, R. L. (1973). Semiannual variation of geomagnetic activity. *Journal of Geophysical Research*, *78*(1), 92-108. https://doi.org/10.1029/JA078i001p00092

Şentürk, E. (2020). Investigation of global ionospheric response of the severe geomagnetic storm on June 22-23, 2015 by GNSS-based TEC observations. *Astrophysics and Space Science*, *365*, 110. https://doi.org/10.1007/s10509-020-03828-z

Sojka, J. J., Rasmussen, C. E., & Schunk, R. W. (1986). An interplanetary magnetic field dependent model of the ionospheric convection electric field. *Journal of Geophysical Research: Space Physics*, *91*(A10), 11281-11290. https://doi.org/10.1029/JA091iA10p11281

Sugiura, M. (1964). *Hourly values of equatorial Dst for the IGY.* Pergamon Press.

Tsurutani, B., Mannucci, A., Iijima, B., Abdu, M. A., Sobral, J. H., Gonzalez, W., & Vasyliunas, V. M. (2004). Global dayside ionospheric uplift and enhancement associated with interplanetary electric fields. *Journal of Geophysical Research: Space Physics*, *109*(A8), 1-16. https://doi.org/10.1029/2003JA010342

Upton, L. A., & Hathaway, D. H. (2023). Solar cycle precursors and the outlook for cycle 25. *Journal of Geophysical Research: Space Physics*, *128*(10), e2023JA031681. https://doi.org/10.1029/2023JA031681

Vaishnav, R., Jacobi, C., & Berdermann, J. (2019). Long-term trends in the ionospheric response to solar extreme-ultraviolet variations. *Annales Geophysicae*, *37*(6),

1141-1159. https://doi.org/10.5194/angeo-37-1141-2019

Vasyliūnas, V. M., & Song, P. (2005). Meaning of ionospheric Joule heating. *Journal of Geophysical Research: Space Physics*, *110*(A2), 1-8. https://doi.org/10.1029/2004JA010615

Wang, W., Lei, J., Burns, A. G., Solomon, S. C., Wiltberger, M., Xu, J., Zhang, Y., Paxton, L., & Coster, A. (2010). Ionospheric response to the initial phase of geomagnetic storms: Common features. *Journal of Geophysical Research: Space Physics*, *115*(A7), 1-18. https://doi.org/10.1029/2009JA014461

Watari, S. (2017). Geomagnetic storms of cycle 24 and their solar sources. *Earth, Planets and Space*, *69*, 70. https://doi.org/10.1186/s40623-017-0653-z

WDC. (1957). *WDC for geomagnetism, Kyoto*. Retrieved Aug 04, 2025, from https://wdc.kugi.kyoto-u.ac.jp///dstae///wwwtmp/WWW_dstae03340870.dat

Wehmeyer, J., Tomikawa, Y., Nishiyama, T., Ogawa, Y., & Franco-Diaz, E. (2026). Poleward disturbances in thermospheric winds during the 3–4 November 2021 geomagnetic storm. *Journal of Geophysical Research: Space Physics*, *131*(2), e2025JA034544. https://doi.org/10.1029/2025JA034544

Yasyukevich, A., Medvedeva, I., Sivtseva, V., Chernigovskaya, M., Ammosov, P., & Gavrilyeva, G. (2020). Strong interrelation between the short-term variability in the ionosphere, upper mesosphere, and winter polar stratosphere. *Remote Sensing*, *12*(10), 1588. https://doi.org/10.3390/rs12101588

Yeeram, T. (2024). The effects of solar radiation and geomagnetic disturbance during consecutive 27-day recurrent geomagnetic storms on variations of equatorial ionospheric parameters and spread F. *Astrophysics and Space Science*, *369*, 62. https://doi.org/10.1007/s10509-024-04327-1

Yi Liu, C. Z., Xu, T., Tang, Q., Deng, Z., Chen, G., & Wang, Z. (2021). Review of ionospheric irregularities and ionospheric electrodynamic coupling in the middle latitude region. *Earth and Planetary Physics*, *5*(5), 462-482. https://doi.org/10.26464/epp2021025

Yu, Y., & Ridley, A. J. (2009). Response of the magnetosphere-ionosphere system to a sudden southward turning of interplanetary magnetic field. *Journal of Geophysical Research: Space Physics*, *114*(A3), 1-10. https://doi.org/10.1029/2008JA013292

JAASCI
http://jaasci.com
JOURNAL OF ADVANCED APPLIED SCIENCES
e-ISSN: 2979-9759
PRENSİP
https://prensip.gen.tr

RESEARCH ARTICLE

Decoupling Intergranular Weak-Links and Intragranular Flux Pinning in Bulk Bi-2212 Superconductors: A Two-Component Exponential Model Approach

Mehmet Ali Aksan[1]✉ • Gokhan Kirat[2]

[1]İnönü University, Faculty of Arts and Sciences, Department of Physics, Malatya/Türkiye
[2]İnonü University, Scientific and Technological Research Center, Malatya/Türkiye

ARTICLE INFO

Article History
Received: 28.05.2026
Accepted: 15.06.2026
First Published: 28.06.2026

Keywords
Bi-2212 superconductors
Critical current density
Flux pinning
Intergranular - intragranular J_c
Two-component exponential model

ABSTRACT

In this study, the influence of sintering time on the structural, microstructural and magneto-transport properties of bulk $Bi_2Sr_2CaCu_2O_{8+\delta}$ (Bi-2212) HT_c superconductors synthesized by the solid-state reaction method was investigated using Two-Component Exponential Model. The samples prepared were heat treated at 840 ºC for two different sintering durations: 60 h (S60) and 120 h (S120). XRD analyses showed that both samples have tetragonal symmetry and increasing the sintering duration to 120 h markedly reduced secondary impurity phases, such as $BiSr_3O_{5.4}$ and $Bi_2Ca_2O_5$, thereby enhancing phase purity and crystallographic order. Furthermore, thermally activated oxygen desorption during prolonged heat treatment caused an expansion of the *c*-axis lattice parameter (from 30.62 Å to 30.68 Å), indicating a transition from the overdoped regime to the optimally doped region. The average crystallite size, estimated using the Scherrer method, increased from 38 nm to 45 nm, while Williamson–Hall analysis revealed a significant reduction in internal strain and defect density. SEM micrographs demonstrated the formation of characteristic platelet-like grain morphology and improved grain interlocking resulting from anisotropic grain growth. Analysis of the transport mechanism based on a semi empirical Two-Component Exponential Model showed that the 120 h sintering protocol not only enhanced the Josephson current transport capability (J_c^{wl}) at the macroscopic level through grain-boundary purification, but also improved the stability of flux pinning centers (H_{int}) at the microscopic level by optimizing nanoscale intragrain defects and oxygen stoichiometry, thereby yielding a dual improvement in high-field magnetic performance.

Please cite this paper as follows:

Aksan, M. A., & Kirat, G. (2026). Decoupling intergranular weak-links and intragranular flux pinning in bulk Bi-2212 superconductors: A two-component exponential model approach. *Journal of Advanced Applied Sciences*, *5*(1), 24-33. https://doi.org/10.61326/jaasci.v5i1.495

1. Introduction

The discovery of high-temperature (HT_c) superconductivity in 1986 became a milestone in scientific world. Subsequently, the discovery of superconductivity in the rare-earth-free Bi–Sr–Ca–Cu–O (BSCCO) system attracted considerable interest (Maeda et al., 1988). Among the various phases of the BSCCO system, $Bi_2Sr_2CaCu_2O_{8+\delta}$ (Bi-2212) system has emerged as one of the most technologically important cuprate superconductors. Although its critical transition temperature ($T_c \approx 80$ K) is lower than that of several other cuprate systems, its superior thermodynamic phase stability, relatively broad synthesis window, ease of processing into bulk, wire and ribbon forms, and remarkable performance under high external magnetic fields have made it a key material for both fundamental quantum-mechanical studies and industrial high-field magnet applications.

✉ Correspondence
E-mail address: mehmet.aksan@inonu.edu.tr

The applicability of bulk polycrystalline Bi-2212 superconductors in high-current engineering applications is critically constrained by the granular nature of the material, weak mechanical properties and pronounced crystallographic anisotropy. In such polycrystalline systems, grain boundaries formed between randomly oriented adjacent grains, along with amorphous secondary phases preferentially segregated at these interfaces during synthesis, markedly degrade the superconducting transport characteristics (Hilgenkamp & Mannhart, 2002). Such grain boundaries act as Josephson weak-link barriers that hinder the continuous circulation of macroscopic supercurrent and limit quantum-mechanical tunneling between adjacent grains. Under an external magnetic field, superconducting phase coherence across the weak-link structures rapidly deteriorates, resulting in a pronounced suppression of the critical current density (J_c) even at low magnetic fields (Peterson & Ekin, 1988). In this regard, precise control of heat-treatment (sintering) parameters to optimize solid-state diffusion kinetics and grain-boundary migration (Ostwald ripening) plays a crucial role in promoting morphological grain interlocking, enhancing crystallographic texturing and narrowing the effective thickness of Josephson weak-link barriers.

Beyond the structural and microstructural morphology, the interstitial oxygen content within the Bi-2212 crystal lattice plays a critical role in determining the electronic properties of the system. Bi-2212 systems prepared by conventional routes in an ambient air atmosphere inherently tend to stay in an overdoped regime, where the hole concentration in the CuO_2 planes deviates from its optimal level, leading to a suppression of Cooper pair density and consequently a reduction in the superconducting transition temperature (T_c) (Ross, 2005). Extended sintering duration facilitates controlled oxygen desorption from the crystal lattice via thermally activated processes. The accompanying expansion of the *c*-axis shifts the system from the overdoped regime to the optimally doped state, consequently improving both the intrinsic (intra-grain) superconducting characteristics of the material and the macroscopic Meissner shielding fraction.

The layered crystal structure of Bi-2212 gives rise to highly complex magnetic vortex (flux-line) dynamics. Due to the large anisotropy parameter, independent two-dimensional (2D) pancake vortex structures confined within individual CuO_2 planes dominate instead of continuous three-dimensional (3D) flux lines throughout the material (Clem, 1991). At high-temperatures and high-magnetic-fields, these 2D pancake vortices readily decouple due to thermal fluctuations and Lorentz-force-driven dynamics, resulting in significant flux creep and consequently strong energy dissipation within the superconducting matrix (Blatter et al., 1994). Maintaining the current-carrying capability of the system requires a transition of the vortex matter from a weakly pinned, ordered Bragg glass phase into a disordered but collectively pinned vortex glass phase with strong flux-pinning centers (Fisher et al., 1991). This transition and stability are directly governed by the optimization of homogeneously distributed nanoscale point defects and oxygen vacancies within the crystal lattice.

In the literature, numerous studies have qualitatively investigated the influence of sintering time on the structural properties of Bi-2212 superconductors (Yang et al., 2016; Zhang et al., 2010), however, the quantitative decoupling of macroscopic weak-link transport and microscopic flux-pinning dynamics in relation to time-dependent thermal processing kinetics remains limited (Kametani et al., 2011; Wang et al., 2018). To elucidate this complex transport mechanism, the experimental magnetic-field dependence of the critical current density ($J_c - H$) can be analyzed with a semi-empirical double-exponential model that simultaneously accounts for intergranular (weak-link) and intragranular contributions. This model enables the quantitative decoupling of the Josephson coherence field (H_{wl}), which characterizes the magnetic-field sensitivity of weak links and the intragranular flux-pinning parameter (H_{int}), which represents the high-field pinning strength within grains.

In this study, bulk Bi-2212 superconducting samples were sintered at a constant temperature of 840 °C for two different durations, 60 h (S60) and 120 h (S120). The primary objective of the work is not only to investigate the effects of extended solid-state diffusion time on crystallographic lattice parameters, microstructural grain-boundary evolution and magnetic shielding capability, but also to quantitatively elucidate the corresponding variations in the model parameters H_{wl} and H_{int}. In this way, the multi-scale impact of sintering time on quantum mechanical phase locking and vortex glass stability is presented within an integrated modeling framework, providing a new physical perspective for predicting the high-field performance limits of bulk cuprate superconductors.

2. Experimental

In this work, the $Bi_2Sr_2CaCu_2O_{8+\delta}$ (Bi-2212) superconducting system was prepared by the conventional solid-state reaction route using high-purity Bi_2O_3, $SrCO_3$, $CaCO_3$ and CuO precursor powders (99.99%). After weighing according to the desired stoichiometric ratios and thorough mixing in an agate mortar, the powders were subjected to calcination at 800 °C for 24 h. The calcined powders were then finely ground, followed by a second calcination treatment at 820 °C for 24 h. The calcined powders were pelletized into circular disk-shaped pellets. Finally, the samples were placed inside a quartz tube and the pellets were subsequently sintered at a constant temperature of 840 °C for two different durations, 60 h and 120 h, to investigate the influence of thermal processing time on structural, magnetic and critical current density properties. It should be emphasized that a pressure of 10 tons was applied during the pelleting process.

The crystallographic structure of the sintered samples was analyzed by X-ray diffraction (XRD) using a Rigaku Miniflex 600 diffractometer equipped with Cu-K_α radiation (λ = 1.5406 Å). The surface morphology, anisotropic grain formations and microstructural characteristics were investigated using a Leo-Evo 40 scanning electron microscope (SEM). Superconducting properties were evaluated by temperature-dependent magnetization (M–T) under a constant external magnetic field of 50 Oe following the Zero-Field-Cooled (ZFC) protocol and magnetic-field-dependent magnetization (M–H) measurements performed with a vibrating sample magnetometer (VSM) integrated into a 9 T Quantum Design Physical Property Measurement System (PPMS).

The magnetic-field dependence of the critical current density ($J_c - H$), obtained from the magnetic hysteresis loops, was analyzed with a semi-empirical Two-Component Exponential Model to elucidate the complex transport behavior of the superconducting matrix. The applied modeling approach made it possible to quantitatively decouple the multi-scale effects of prolonged heat treatment on macroscopic weak-link transport and microscopic flux-pinning dynamics.

3. Results and Discussion

Figure 1 shows the XRD patterns of $Bi_2Sr_2CaCu_2O_{8+\delta}$ (Bi-2212) superconducting samples sintered at 840 ºC for 60 h (S60) and 120 h (S120). Diffraction peak indexing was performed using the standard JCPDS card for the Bi-2212 phase (No. 80-0396), confirming that all major reflections correspond to a tetragonal crystal structure in agreement with previous studies (Maeda et al., 1988; Tarascon et al., 1988). Bi-2212 crystallizes in a body-centered tetragonal sub-cell with the space group I4/mmm (No. 139) (Liang et al., 1988).

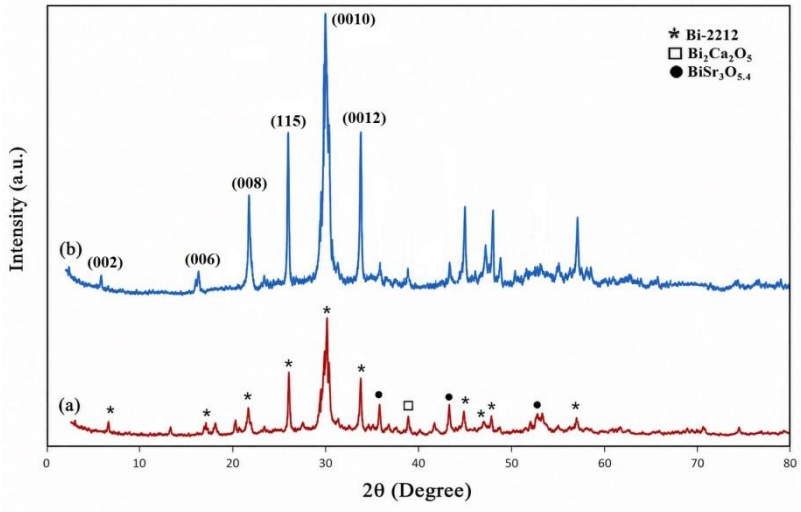

Figure 1. XRD patterns of Bi-2212 samples sintered at 840 ºC for (a) 60 h (S60) and (b) 120 h (S120).

Using the least-squares refinement method, the unit cell parameters of the S60 sample were calculated to be $a = b \approx 3.814$ Å and $c \approx 30.62$ Å ($c/a \approx 8.03$), consistent with the ideal tetragonal unit-cell structure of Bi-2212 (Tarascon et al., 1988). For the S120 sample, the lattice parameters were determined to be $a = b \approx 3.816$ Å and $c \approx 30.68$ Å ($c/a \approx 8.04$). The slight expansion of the *c*-axis obtained in S120 sample is attributed to thermally induced oxygen desorption during prolonged heat treatment. A decrease in the interstitial oxygen concentration in the Bi–O layers weakens the interlayer electrostatic interactions, thereby leading to *c*-axis expansion and shifting the system from the overdoped regime to the optimally doped superconducting regime (Argyriou et al., 1996; Ross, 2005). The optimization of oxygen stoichiometry shifts the hole concentration in the CuO_2 planes toward its optimal level in the superconducting phase diagram, thereby increasing both the density of states at the Fermi level and the Cooper pair density. This electronically stabilized lattice state is the main reason for the enhancements in superconducting transition temperature (T_c) and critical current density (J_c), which will be discussed in later sections. The unit-cell volumes were found to be approximately 445.42 Å³ for the S60 sample and 446.76 Å³ for the S120 sample. These results obviously show that prolonged sintering does not lead to any significant structural degradation or lattice distortion.

The strongest reflections indexed to the (0 0 2), (0 0 6), (0 0 8), (0 0 10), (0 0 12) and (1 1 5) planes are characteristic signatures of the layered perovskite structure of Bi-2212. Compared with the S60 sample, the S120 sample exhibits noticeably increased peak intensities, reflecting improved phase purity and a higher degree of crystallographic ordering achieved due to prolonged sintering. This behavior is consistent with the kinetic framework in which prolonged sintering promotes solid-state diffusion and reaction kinetics, resulting in the gradual reduction of residual intermediate and secondary

phases and consequently enhancing the crystallographic ordering of the system (Heeb et al., 1993).

In the S60 sample, the diffraction peaks attributed to secondary impurity phases such as $BiSr_3O_{5.4}$ and $Bi_2Ca_2O_5$ were obtained, arising from incomplete reactions. However, in the S120 sample, the volume fraction of these secondary phases is significantly suppressed. This suggests that Bi-2212 phase formation at 840 ºC is governed by slow reaction kinetics and that a prolonged sintering protocol of 120 h is essential to drive the system toward a thermodynamically more stable, nearly single-phase Bi-2212 state.

The average crystallite size (D) was calculated using the Scherrer equation (Scherrer, 1918):

$$D = K\lambda/\beta_{hkl}Cos\theta \quad (1)$$

where K is a dimensionless shape factor, with a value close to unity in general, λ is the wavelength of the incident X-ray radiation (1.5406 Å), β_{hkl} is the line broadening at half the maximum intensity (FWHM) and θ is the Bragg angle. Considering the anisotropic crystal structure, the (0 0 10) reflection was selected to estimate the crystallite size along the *c*-axis (i.e., perpendicular to the CuO_2 planes). The resulting values were D ≈ 38 nm for the S60 sample and D ≈ 45 nm for the S120 sample. The increase in crystallite size confirms grain growth during prolonged sintering, which enhances intergranular connectivity. To systematically distinguish the individual contributions of crystallite size and lattice microstrain to the diffraction peak broadening, Williamson–Hall (W-H) analysis was implemented according to the uniform deformation model (UDM) framework. The mathematical formulation is expressed as:

$$\beta_{hkl}Cos\theta = \frac{K\lambda}{D} + 4\varepsilon Sin\theta \quad (2)$$

where ε is the lattice microstrain. The calculated microstrain (ε) values obtained from Williamson–Hall analysis decrease from $\varepsilon \approx 2.1 \times 10^{-3}$ for S60 to $\varepsilon \approx 1.6 \times 10^{-3}$ for S120. This substantial reduction directly reflects the relaxation of internal stresses and lattice defects generated during the solid-state synthesis, confirming a significant enhancement in the long-range crystallographic order and overall crystallinity with prolonged sintering time.

The surface morphology and microstructural characteristics of both Bi-2212 samples were examined using the SEM micrographs presented in Figure 2. The images clearly reveal characteristic platelet-like grain morphology, which is a well-known feature of Bi-based cuprate superconductors. This morphology originates from the highly anisotropic crystal structure of the Bi-2212 phase, in which strong covalent bonding within the CuO_2 planes promotes preferential and faster growth along the *ab*-plane.

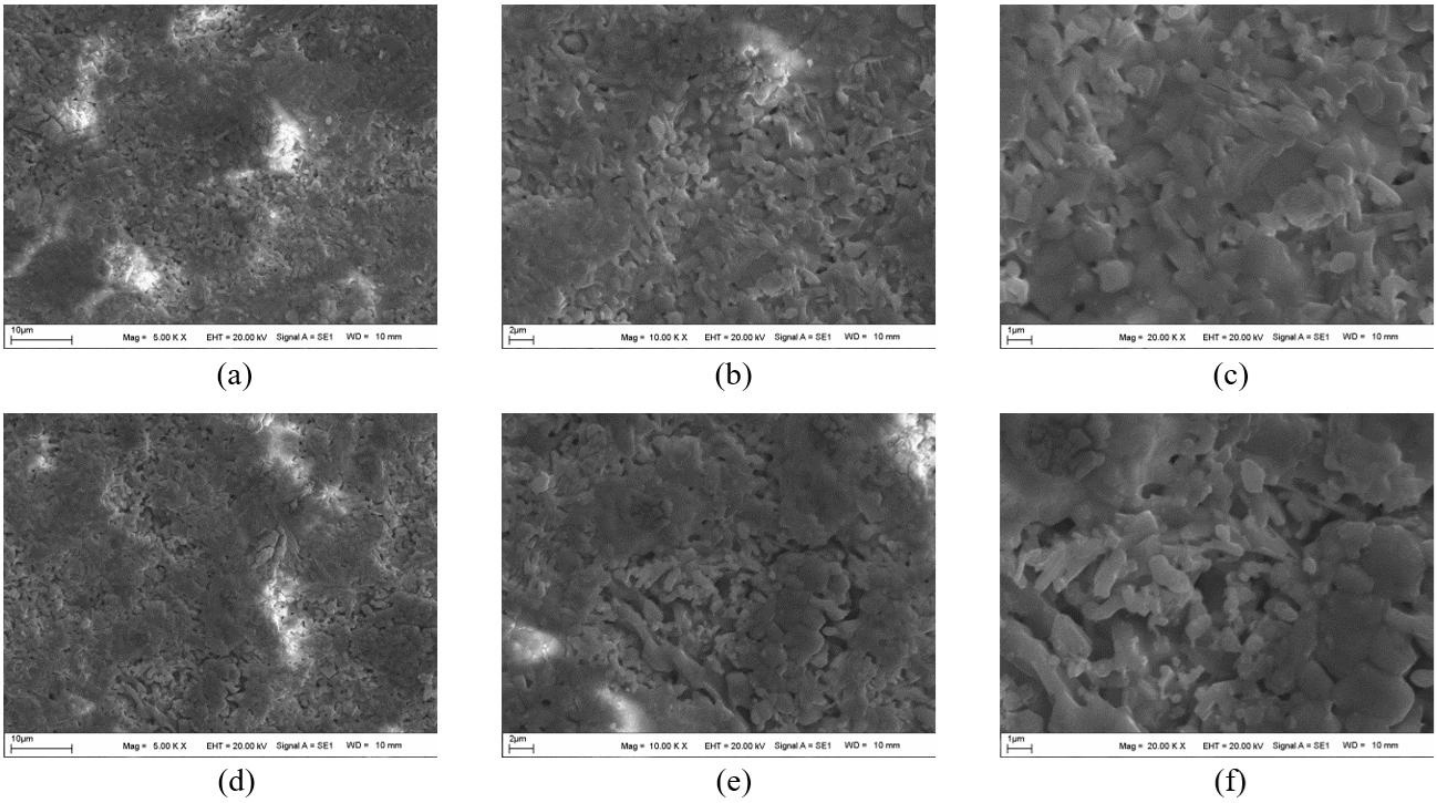

Figure 2. SEM micrographs of Bi-2212 samples sintered at 840 ºC for 60 h (a–c) and 120 h (d–f), recorded at magnifications of 5000×, 10000× and 20000×, respectively.

The SEM micrographs of the S60 sample (Figure 2a–c) show a microstructure consisting of thin platelet-like grains with lateral dimensions in the range of approximately 0.5–2 μm. The grains exhibit a highly random orientation, while uniformly distributed micro-porosities are observed on the sample surface. Although sintering of 60 h is sufficient for the formation of the Bi-2212 phase, mass transport, densification and grain growth processes remain incomplete. Moreover, the irregular nanoscale inclusions which are generally observed at grain boundaries are associated with secondary impurity phases such as $BiSr_3O_{5.4}$ and $Bi_2Ca_2O_5$, detected in the XRD analyses (Garnier et al., 1999).

In the S120 sample sintered for 120 h, a pronounced microstructural evolution is observed (Figure 2d–f). The grains grow along the *ab*-plane, reaching lateral dimensions of approximately 1–4 μm. This morphological improvement directly confirms the increase in crystallite size along the *c*-axis calculated using the Scherrer equation. The prolonged sintering promotes solid-state diffusion kinetics and grain-boundary migration, leading to enhanced intergranular interlocking and the formation of a larger effective contact area, thereby reducing weak-link effects in superconducting transport (Garnier et al., 1999). The improved crystallographic texturing and the reduction of secondary phases effectively decrease the thickness of the Josephson tunneling barrier. This microstructural improvement hinders the rapid decrease of the critical current density, J_c , at low magnetic fields and constitutes a key factor responsible for the increase in the intergranular weak-link characteristic field (H_{wl}), as given in the model parameters.

On the other hand, prolonged sintering leads to the coalescence of small pores into larger, localized macropores (Figure 2f). Despite the presence of such macropores in the S120 sample, the significantly enhanced diamagnetic signal observed in the M–T measurements indicates a higher shielding volume, which can be attributed to the increased grain size, stronger intergranular mechanical interlocking and higher phase purity. The localization of pores within the microstructure, without interrupting continuous current percolation paths, together with the improved grain quality, ultimately leads to an overall improvement in superconducting performance.

The temperature-dependent DC magnetization (M–T) results are showed in Figure 3. Both samples exhibit a pronounced diamagnetic transition characteristic of superconductivity; however, notable differences are observed between the S60 and S120 samples with respect to the superconducting transition temperature (T_c) and the Meissner shielding fraction.

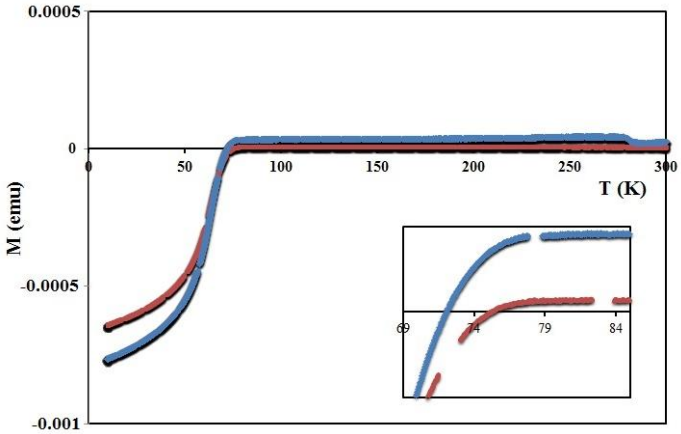

Figure 3. Temperature-dependent magnetization (M–T) curves of the samples sintered at 840 ºC for (a) 60 h (red curve) and (b) 120 h (blue curve).

As shown in the inset of Figure 3, which shows the reduced temperature range between 69 and 84 K, the onset superconducting transition temperature ($T_{c,onset}$) for the S60 sample (red curve) is found to be ~75 K. This value is below the maximum T_c value (~85 K) reported for optimally doped Bi-2212 compounds. For the S120 sample (blue curve), however, $T_{c,onset}$ increases to approximately 80 K upon prolonging the sintering duration to 120 h.

The observed increase in T_c is directly associated with the lattice parameter variations obtained from the XRD analysis. Bi-2212 system synthesized in ambient air typically exhibits an overdoped oxygen state, which suppresses the T_c temperature. Prolonged heat treatment of 120 h facilitates controlled oxygen desorption from the crystal lattice, consistent with the *c*-axis expansion observed in the XRD results. As a consequence, the system shifts from the overdoped regime toward the optimally doped regime, leading to an increase in the $T_{c,onset}$ value (Ross, 2005). Moreover, the sharper and steeper diamagnetic transition exhibited by the S120 sample, characterized by a narrower transition width (ΔT_c), indicates a closer convergence between the intrinsic intra-grain superconducting transition

temperature and the intergranular Josephson phase-locking temperature, suggesting the formation of a more homogeneous superconducting matrix. This result provides strong experimental evidence that grain-boundary purification enhances macroscopic quantum coherence and allows it to remain robust against external magnetic fields even at elevated temperatures.

In addition, the low-temperature diamagnetic response of the S120 sample is larger than that of the S60 sample. This behavior provides clear evidence of a significant increase in the effective superconducting volume fraction (shielding fraction) in the S120 sample. The pronounced difference in diamagnetic response between the S60 and S120 samples is fully consistent with the microstructural evolution observed in the SEM analysis. In granular superconductors, the magnitude of the ZFC signal strongly depends on the quality of intergranular connectivity and on the ability of macroscopic shielding currents to establish continuous current loops throughout the structure (Malozemoff, 1989). As shown in the SEM micrographs, the fine-grained morphology and microporosity in the S60 sample hinder the macroscopic circulation of shielding currents, thereby restricting the diamagnetic response predominantly to individual intragranular contributions. By contrast, in the S120 sample, prolonged sintering promotes the growth of platelet-like grains, resulting in enlarged intergranular contact regions and strengthened weak-link coupling, despite the presence of localized macropores in the microstructure. The enhanced intergranular connectivity allows the induced superconducting currents to establish continuous closed-loop over larger effective volumes, thereby substantially improving the overall diamagnetic response and Meissner shielding capability of the S120 sample.

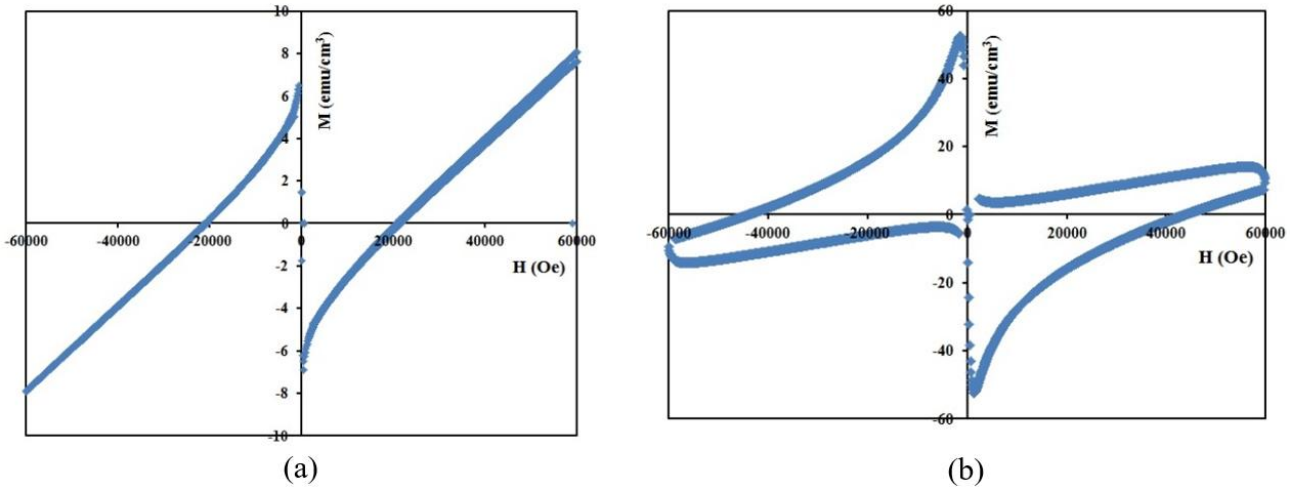

Figure 4. M–H loops measured at (a) 50 K and (b) 10 K for the sample (S60) sintered at 840 ºC for 60 h.

The magnetic-field dependence of magnetization, M(H), for both S60 and S120 samples was measured at 50 K and 10 K in an applied magnetic-field range of ±60,000 Oe (6 T) and the corresponding hysteresis loops are shown in Figures 4 and 5. These measurements provide key information regarding the flux-pinning properties and critical current densities (J_c) of the samples.

M-H loops at 50 K clearly reveal the differences in superconducting behavior between the samples. As shown in the M–H loop of the S60 sample (Figure 4a), the magnetization is small and the high-field response becomes nearly linear with a positive slope, indicating a dominant paramagnetic contribution. At this temperature, thermal fluctuations strongly increases due to the pronounced anisotropy of Bi-2212. The low superconducting volume fraction and weak pinning behavior in the S60 sample lead to a suppressed diamagnetic response, such that the measured signal is largely governed by background contributions arising from non-superconducting paramagnetic impurities and/or unreacted secondary phases.

In the M–H loop of the S120 sample at 50 K (Figure 5a), paramagnetic contribution to magnetization is still dominant. However, the magnetization magnitude is approximately two orders of magnitude higher than that of the S60 sample. This result shows that although the sintering process of 120 h significantly improves intergranular links, thermal fluctuations at 50 K suppress the superconducting fraction.

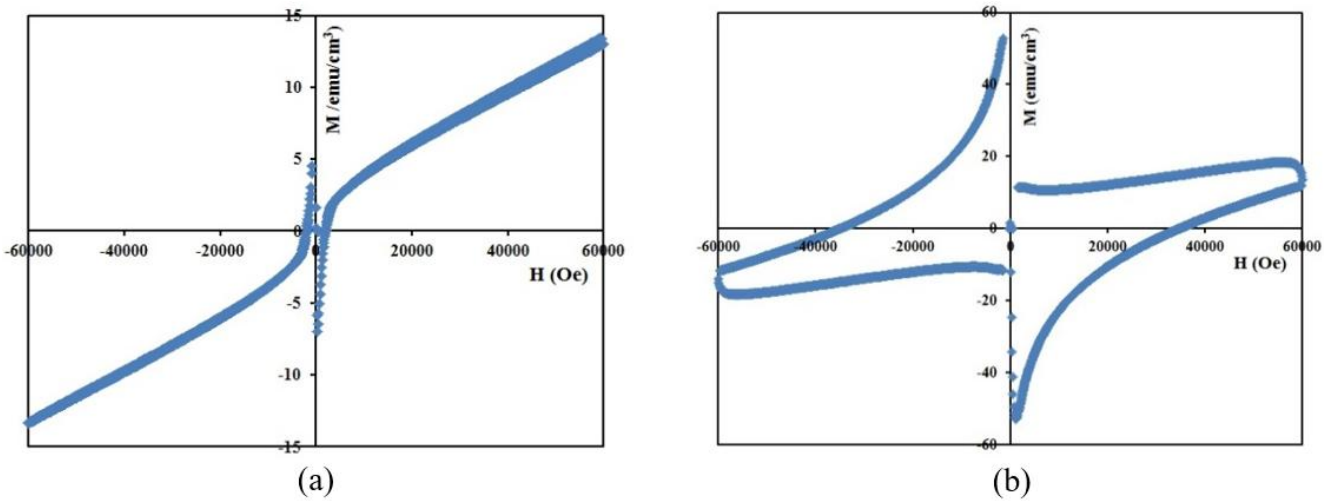

Figure 5. M–H loops measured at (a) 50 K and (b) 10 K for the sample (S120) sintered at 840 °C for 120 h.

At 10 K, thermal activation is strongly suppressed and the superconducting diamagnetic response in both samples completely dominates the paramagnetic background, giving rise to the characteristic symmetric "butterfly-shaped" hysteresis loops which are typical for type-II superconductors (Figures 4b and 5b). The non-closure of the loops up to 60000 Oe (6 T) indicates that the irreversibility field (H_{irr}) at 10 K is well above 6 T for both samples.

The critical current density (J_c) values were calculated according to the Bean formula (Bean, 1964; Gyorgy et al., 1989) and the variation of J_c with the applied magnetic field ($J_c - H$) is shown in Figure 6.

$$J_c = \frac{20\Delta M}{a\left(1-\frac{a}{3b}\right)} \quad (3)$$

where $\Delta M = M^+ - M^-$, a and b are sample dimensions. The a and b dimensions are 3.8 mm and 2.65 mm for S60 sample and 4.1 mm and 2.3 mm for S120 sample, respectively.

According to the Bean critical state model ($J_c \propto \Delta M$), ΔM is directly proportional to both the flux-pinning strength and the critical current-carrying capability. It was found that the ΔM value of the S120 sample near H=0 in the M–H loop at 10 K is larger than that of the S60 sample. The increase in ΔM at 10 K clearly indicates an increase in the critical current density (J_c) in the S120 sample. This trend is in excellent agreement with SEM results, where grain growth and the development of a denser, better-connected microstructure induced by prolonged sintering significantly enhance vortex pinning efficiency.

In polycrystalline HT_c cuprate superconductors, the magnetic-field dependence of J_c can be modeled as the linear superposition of two distinct transport regimes, represented by exponential functions (Peterson & Ekin, 1988): At low magnetic fields, superconducting transport is predominantly governed by the weak-link behavior of intergranular Josephson junctions. At higher fields, however, the phase coherence across these junctions is progressively destroyed, causing the transport mechanism to become dominated by intragranular flux-pinning processes (Hilgenkamp & Mannhart, 2002). To mathematically simulate this complex transport behavior and quantitatively separate individual contributions, the Two-Component Exponential Model is employed (Müller & Matthews, 1993; Peterson & Ekin, 1988). The equation of the model is given by

$$J_c = J_c^{wl}(0)\exp\left(-\frac{H}{H_{wl}}\right) + J_c^{int}(0)\exp\left(-\frac{H}{H_{int}}\right) \quad (4)$$

where $J_c^{wl}(0)$ and $J_c^{int}(0)$ are the zero-field intergranular and intragranular critical current density components, respectively, while H_{wl} and H_{int} denote the characteristic decay fields associated with weak-link coupling and intragranular flux pinning (Ekin et al., 1989; Huang et al., 1998).

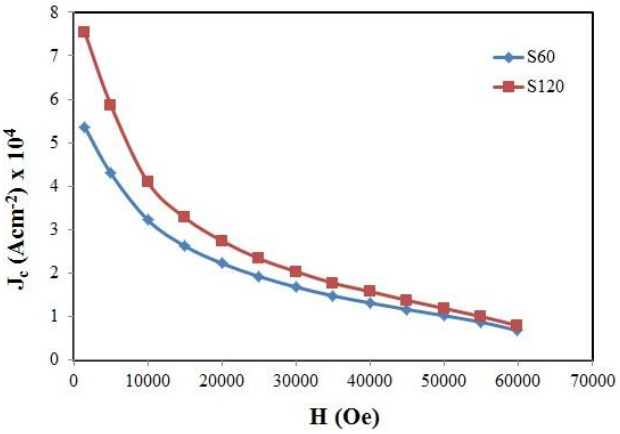

Figure 6. Magnetic-field dependence of the critical current density ($J_c - H$) for Bi-2212 samples sintered at 840 °C for 60 h (S60) and 120 h (S120).

When this semi-empirical model is applied to the experimental $J_c - H$ curves, the resulting parametric data for

the S60 and S120 samples clearly elucidate the microstructural and chemical evolution of the fabricated materials (see Table 1).

Table 1. Semi-empirical fitting parameters obtained from the $J_c - H$ analysis of the S60 and S120 samples at 10 K.

Material	$J_c^{wl}(0)$ (Acm^{-2})	$J_c^{int}(0)$ (Acm^{-2})	H_{wl} (Oe)	H_{int} (Oe)
S60	1.6×10^4	4.1×10^4	1200	38000
S120	2.3×10^4	5.6×10^4	1850	47000

3.1. Low-Field Region (0 < H < 5000 Oe) and Weak-Link Characteristics

As shown in Figure 6, both samples exhibit an extremely sharp and dramatic decrease in J_c with increasing the magnetic field from H = 0. This behavior can be successfully explained within the framework of the first term of the model, namely the J_c^{wl} component, which represents intergranular weak-link transport. In the S60 sample, the grain boundaries formed after a sintering of 60 h are not yet fully optimized in terms of crystallographic coherence and chemical homogeneity. During shorter sintering treatments, the accumulation of secondary phases at grain boundaries suppresses the superconducting order parameter in these regions (Hilgenkamp & Mannhart, 2002). The low H_{wl} value (~1200 Oe) obtained from the model indicates that even relatively small applied magnetic fields rapidly destroy the intergranular Josephson phase coherence, thereby blocking the macroscopic supercurrent flowing through the weak-link network.

Upon prolonging the sintering to 120 h (S120), the total theoretical zero-field critical current $J_c(0)$ increases from ~5.7 × 10^4 Acm^{-2} to 7.9 × 10^4 Acm^{-2}. Notably, both the weak-link term $J_c^{wl}(0)$ and the characteristic field H_{wl} (~1850 Oe) show a pronounced increase. This behavior indicates that the solid-state diffusion occurring during prolonged sintering effectively reduces intergranular voids, suppresses grain-boundary impurity phases and enhances *c*-axis texturing. The consequent reduction in grain misorientation angle strengthens Josephson tunneling across grain boundaries, thereby improving the low-field robustness of the superconducting state (Hilgenkamp & Mannhart, 2002).

3.2. High-Field Region (H > 10000 Oe) and Flux-Pinning Mechanism

In contrast to the sharp degradation observed at low magnetic fields, J_c exhibits a gradual and slower suppression rate in the high magnetic field region (H > 1000 Oe). In high-field region, the intergranular weak-link network becomes effectively dephased, $\exp(-H/H_{wl}) \to 0$ and superconducting current transport is dominated entirely by the second term of the model, the intragranular current-carrying component (J_c^{int}) (Ekin et al., 1989). The slower decreasing trend implies a strong resistance of effective vortex-pinning centers in the microstructure against applied magnetic fields. The superior J_c performance of the S120 sample in the high-field region indicates an enhanced flux pinning capability. According to the semi-empirical model, the higher H_{int} value obtained for the S120 sample (47000 Oe) compared to the S60 sample (38000 Oe) provides strong evidence that prolonged sintering not only enhances grain-boundary quality but also substantially improves the intragranular crystal matrix.

The results derived from the semi-empirical modeling are closely linked to the solid-state reaction kinetics and vortices in Bi-2212 superconductors. Due to the extremely large anisotropy of the Bi-2212 phase (γ>50), magnetic flux lines do not form continuous 3D-vortex structures in the material; instead, they become confined as quasi-2D "pancake vortices" localized in the CuO_2 planes (Blatter et al., 1994). At low temperatures such as 10 K, thermal fluctuations are insufficient to mobilize these pancake vortices, causing them to remain trapped at point-like defects in the superconducting matrix. If these vortices are not effectively pinned, the Lorentz force generated by the macroscopic transport current drives vortex motion (flux flow), resulting in dissipative energy losses and the local destruction of the superconducting state (Blatter et al., 1994; Fisher et al., 1991).

The higher $J_c^{int}(0)$ and H_{int} values obtained for the S120 sample indicate that prolonged sintering leads to an optimized and spatially homogeneous distribution of cationic disorder and oxygen vacancies (δ) in the crystal lattice. Point-like lattice defects and microscopic dislocations with characteristic dimensions comparable to the extremely short coherence length of Bi-2212 (ξ_{ab} ~2 nm) act as strong potential wells (pinning centers) for pancake vortices. The stable and slowly decreasing behavior observed in the high-field region of Figure 6 suggests that the vortex system is not in a weakly pinned and ordered Bragg glass phase, but rather becomes in a strongly disordered vortex glass phase capable of maintaining superconducting integrity under high magnetic fields (Fisher et al., 1991). The high intragranular flux-pinning field (H_{int}) extracted from the semi-empirical model shows that the point-like defects optimized with a sintering of 120 h reinforce the Josephson coupling between 2D pancake vortices, thereby stabilizing coherent 3D vortex-line formations. This strong collective pinning substantially enhances the resistance of the vortex system against the Lorentz force under high magnetic fields,

while significantly suppressing thermally and current-activated vortex creep. As a result, the locking of the system into the vortex glass phase directly guarantees superior current-carrying stability under the high magnetic fields.

3.3. Vortex Glass Phase and the Role of Point Defects

Semi-empirical analysis of the $J_c - H$ characteristics of the S60 and S120 samples at 10 K indicates that prolonged sintering improves superconducting performance through a dual mechanism:

Macroscopic Level: Chemical purification of grain boundaries and improved structural texturing enhance the Josephson weak-link current-carrying capacity (J_c^{wl}), leading to an increase in zero-field critical current density and an improvement in stability in the low-field region (Hilgenkamp & Mannhart, 2002).

Microscopic Level: The optimization of intragranular defect structures and oxygen stoichiometry enhances the stability of pinning centers (H_{int}). In the high-field region, it strengthens the resistance of 2D pancake vortices against the Lorentz force, resulting in a significantly reduced critical current decreasing rate (Blatter et al., 1994; Fisher et al., 1991).

These results provide semi-empirical and theoretical evidence that prolonged sintering is a critical processing parameter for Bi-2212 bulk superconductors in practical high-field magnet applications, as it simultaneously enhances intergranular weak-link connectivity and stabilizes intragranular vortex dynamics.

4. Conclusion

In this study, the effects of sintering time (60 h and 120 h) on the structural, microstructural and magneto-transport properties of bulk $Bi_2Sr_2CaCu_2O_{8+\delta}$ (Bi-2212) HT_c superconductors were investigated by experimental characterization and a semi-empirical Two-Component Exponential Model in detail. The results clearly show that the sintering of 120 h at 840 °C optimizes the superconducting properties of the material through a dual-scale improvement, affecting both macroscopic and microscopic levels. Structural analyses revealed that prolonging the sintering duration from 60 h to 120 h largely eliminates performance-limiting secondary impurity phases, such as $BiSr_3O_{5.4}$ and $Bi_2Ca_2O_5$, thereby improving phase purity. The thermally activated and controlled oxygen desorption occurring during the heat treatment expands the *c*-axis, shifting the system from the overdoped regime to the optimally doped regime associated with enhanced superconducting performance. This optimization balances the carrier concentration in the CuO_2 planes, thereby establishing a microscopic origin for the enhancement of the critical current density. Furthermore, the increase in crystallite size accompanied by the decrease in microstrain indicates the reduction of lattice defects and the improvement of crystalline quality. SEM micrographs confirmed that prolonged sintering develops the anisotropic platelet-like grain morphology characteristic of the Bi-2212 system, while simultaneously promoting stronger mechanical interlocking between adjacent grains. Two-component exponential modelling analysis of the transport mechanism further revealed that the 120 h sintering treatment improves low-field stability and enhances the Josephson weak-link current-carrying capacity (J_c^{wl}) through effective grain-boundary purification at the macroscopic level. At the microscopic scale, the optimization of intragranular nanoscale defects and oxygen vacancies increases the stability of flux-pinning centers (H_{int}), thereby providing strong resistance against the field-induced motion of 2D pancake vortices under high magnetic fields. In conclusion, the optimization of the solid-state reaction duration has been identified as a critical processing parameter for enhancing the application potential of Bi-2212-based bulk superconductors in large-scale engineering applications, including practical high-field magnet technologies, superconducting wires and tape industries.

Conflict of Interest

The authors declare that they have no conflict of interest.

Disclosure of Generative AI Use

An AI tool was used partially during the translation process.

References

Argyriou, D. N., Garcia, J. A., Mitchell, J. F., Jorgensen, J. D., & Hinks, D. G. (1996). Phase development of Bi-2212 superconductor: A time-resolved neutron powder diffraction investigation. *Journal of Materials Research*, *11*(2), 277-280. https://doi.org/10.1557/JMR.1996.0032

Bean, C. P. (1964). Magnetization of high-field superconductors. *Reviews of Modern Physics*, *36*(1), 31. https://doi.org/10.1103/RevModPhys.36.31

Blatter, G., Feigel'man, M. V., Geshkenbein, V. B., Larkin, A. I., & Vinokur, V. M. (1994). Vortices in high-temperature superconductors. *Reviews of Modern Physics*, *66*(4), 1125. https://doi.org/10.1103/RevModPhys.66.1125

Clem, J. R. (1991). Two-dimensional vortices in a stack of thin superconducting films: A model for high-temperature superconducting multilayers. *Physical Review B*, *43*(10), 7837. https://doi.org/10.1103/PhysRevB.43.7837

Ekin, J. W., Larson, T. M., Hermann, A. M., Sheng, Z. Z., Togano, K., & Kumakura, H. (1989). Double-step behavior of critical current vs. magnetic field in Y-, Bi- and Tl-based bulk high-T_c superconductors. *Physica C:*

Superconductivity, *160*(5-6), 489-496. https://doi.org/10.1016/0921-4534(89)90425-5

Fisher, D. S., Fisher, M. P., & Huse, D. A. (1991). Thermal fluctuations, quenched disorder, phase transitions, and transport in type-II superconductors. *Physical Review B*, *43*(1), 130. https://doi.org/10.1103/PhysRevB.43.130

Garnier, V., Caillard, R., Sotelo, A., & Desgardin, G. (1999). Relationship among synthesis, microstructure and properties in sinter-forged Bi-2212 ceramics. *Physica C: Superconductivity*, *319*(3-4), 197-208. https://doi.org/10.1016/S0921-4534(99)00308-1

Gyorgy, E. M., Van Dover, R. B., Jackson, K. A., Schneemeyer, L. F., & Waszczak, J. V. (1989). Anisotropic critical currents in Ba2YCu3O7 analyzed using an extended Bean model. *Applied Physics Letters*, *55*(3), 283-285. https://doi.org/10.1063/1.102387

Heeb, B., Gauckler, L. J., Heinrich, H., & Kostorz, G. (1993). From imperfect to perfect $Bi_2Sr_2CaCu_2O_x$ (Bi–2212) grains. *Journal of Materials Research*, *8*(9), 2170-2176. https://doi.org/10.1557/JMR.1993.2170

Hilgenkamp, H., & Mannhart, J. (2002). Grain boundaries in high-T_c superconductors. *Reviews of Modern Physics*, *74*(2), 485. https://doi.org/10.1103/RevModPhys.74.485

Huang, Y. K., ten Haken, B., & ten Kate, H. H. (1998). Critical current of high T_c superconducting Bi2223/Ag tapes. *Physica C: Superconductivity*, *309*(3-4), 197-202. https://doi.org/10.1016/S0921-4534(98)00608-X

Kametani, F., Shen, T., Jiang, J., Scheuerlein, C., Malagoli, A., Di Michiel, M., Huang, Y., Miao, H., Parrell, J. A., Hellstrom, E. E., & Larbalestier, D. C. (2011). Bubble formation within filaments of melt-processed Bi2212 wires and its strongly negative effect on the critical current density. *Superconductor Science and Technology*, *24*(7), 075009. https://doi.org/10.1088/0953-2048/24/7/075009

Liang, J. K., Xie, S. S., Che, G. C., Huang, J. Q., Zhang, Y. L., & Zhao, Z. X. (1988). Crystal structure and superconductivity of $Bi_2Sr_2CaCu_2O_8$ compound. *Modern Physics Letters B*, *2*(01), 483-489. https://doi.org/10.1142/S0217984988000059

Maeda, H., Tanaka, Y., Fukutomi, M., & Asano, T. (1988). A new high-T_c oxide superconductor without a rare earth element. *Japanese Journal of Applied Physics*, *27*(2A), L209. https://doi.org/10.1143/JJAP.27.L209

Malozemoff, A. P. (1989). Macroscopic magnetic properties of high temperature superconductors. In D. M. Ginsberg (Ed.), *Physical properties of high temperature superconductors I* (pp. 71-150). World Scientific. https://doi.org/10.1142/0675

Müller, K. H., & Matthews, D. N. (1993). A model for the hysteretic critical current density in polycrystalline high-temperature superconductors. *Physica C: Superconductivity*, *206*(3-4), 275-284. https://doi.org/10.1016/0921-4534(93)90526-V

Özçelik, B., Özkurt, B., Yakıncı, M. E., Sotelo, A., & Madre, M. A. (2013). Relationship between annealing time and magnetic properties in Bi-2212 textured composites. *Journal of Superconductivity and Novel Magnetism*, *26*(4), 873-878. https://doi.org/10.1007/s10948-012-1874-9

Peterson, R. L., & Ekin, J. W. (1988). Josephson-junction model of critical current in granular $Y_1Ba_2Cu_3O_{7-\delta}$ superconductors. *Physical Review B*, *37*(16), 9848. https://doi.org/10.1103/PhysRevB.37.9848

Ross, D. K. (2005). A determination of the variation in the lattice parameters of $Bi_2Sr_2CaCu_2O_{8+x}$ (Bi-2212) as a function of temperature and oxygen content. *Physica C: Superconductivity*, *425*(3-4), 130-134. https://doi.org/10.1016/j.physc.2005.06.016

Scherrer, P. (1918). Estimation of the size and internal structure of colloidal particles by means of röntgen. *Nachrichten von der Gesellschaft der Wissenschaften zu Göttingen*, *2*, 96-100.

Tarascon, J. M., McKinnon, W. R., Barboux, P., Hwang, D. M., Bagley, B. G., Greene, L. H., Hull, G. W., LePage, Y., Stoffel, N., & Giroud, M. (1988). Preparation, structure, and properties of the superconducting compound series $Bi_2Sr_2Ca_{n-1}Cu_nO_y$ with n=1,2, and 3. *Physical Review B*, *38*(13), 8885. https://doi.org/10.1103/PhysRevB.38.8885

Wang, G., Raine, M. J., & Hampshire, D. P. (2018). The cause of 'weak-link'grain boundary behaviour in polycrystalline $Bi_2Sr_2CaCu_2O_8$ and $Bi_2Sr_2Ca_2Cu_3O_{10}$ superconductors. *Superconductor Science and Technology*, *31*(2), 024001. https://doi.org/10.1088/1361-6668/aaa1b8

Yang, H., Shahzad, M. B., Yu, X., & Qi, Y. (2016). Influence mechanism of secondary gel technique on Bi-2212 superconducting phase: Gel model simulation and verification. *Materials & Design*, *99*, 115-119. https://doi.org/10.1016/j.matdes.2016.03.051

Zhang, Y., Yang, H., Li, M., Sun, B., & Qi, Y. (2010). Improvement of multiple oxide properties: Effect of gel processes on the quality of $Bi_2Sr_2CaCu_2O_{8+\delta}$ superconducting powders. *CrystEngComm*, *12*(10), 3046-3051. https://doi.org/10.1039/B927276C

JAASCI
http://jaasci.com
JOURNAL OF ADVANCED APPLIED SCIENCES
e-ISSN: 2979-9759
PRENSIP
https://prensip.gen.tr

RESEARCH ARTICLE

Influence of Blast Furnace Slag Content on the Density, Microstructure, Hardness, and Wear Behavior of Pure Aluminum Matrix Composites Fabricated by Powder Metallurgy

Hakan Ada[1,2]✉ • Sadiye Yazır[2]

[1]Gazi University, Faculty of Technology, Department of Metallurgical and Materials Engineering, Ankara/Türkiye
[2]Kastamonu University, Faculty of Engineering and Architecture, Department of Mechanical Engineering, Kastamonu/Türkiye

ARTICLE INFO

Article History
Received: 09.06.2026
Accepted: 19.06.2026
First Published: 28.06.2026

Keywords
Aluminum matrix composites
Blast furnace slag (BFS)
Hardness
Microstructure
Powder metallurgy
Wear behavior

ABSTRACT

This study investigates the effects of blast furnace slag (BFS) reinforcement on the microstructural, physical, mechanical, and tribological properties of pure aluminum matrix composites. Composite samples containing 0.125, 0.25, 0.5, 1, 2, 4, 8, 12, and 16 wt.% BFS were fabricated by powder metallurgy. Theoretical and experimental densities were determined, relative density and porosity values were calculated, and the samples were characterized using optical microscopy, hardness measurements, and pin-on-disk wear tests. The results showed that the addition of BFS had a limited influence on the theoretical density due to the similar densities of aluminum and BFS. However, experimental and relative density values decreased at higher reinforcement levels, while porosity increased noticeably. Although all composites exhibited relative densities above 95%, increasing BFS content adversely affected densification behavior. Optical microscopy revealed a relatively homogeneous microstructure at BFS contents of 2–4 wt.%, whereas particle agglomeration and pore formation became more pronounced at higher reinforcement levels. Hardness results indicated that the effect of BFS reinforcement was not linear. Hardness values remained comparable to those of unreinforced aluminum at BFS contents of 2–4 wt.% but decreased significantly at higher reinforcement levels due to increased porosity and particle agglomeration. A similar trend was observed in the wear tests. The unreinforced aluminum sample exhibited the lowest weight loss, while wear loss increased with increasing BFS content. In particular, composites containing 8–16 wt.% BFS showed considerably higher weight loss, which was associated with increased porosity, microstructural heterogeneity, and reduced hardness. The findings demonstrate that blast furnace slag can be used as a low-cost, environmentally friendly reinforcement material in aluminum matrix composites. However, excessive BFS additions promote porosity and agglomeration, which adversely affect densification, hardness, and wear performance. Considering the combined results of density, microstructure, hardness, and wear behavior, BFS contents of 2–4 wt.% provided the most balanced overall performance among the investigated composites.

Please cite this paper as follows:

Ada, H., & Yazır, S. (2026). Influence of blast furnace slag content on the density, microstructure, hardness, and wear behavior of pure aluminum matrix composites fabricated by powder metallurgy. *Journal of Advanced Applied Sciences*, *5*(1), 34-44. https://doi.org/10.61326/jaasci.v5i1.501

1. Introduction

Powder metallurgy (PM) is an advanced manufacturing technique that enables the production of components with simple or complex geometries while maintaining dimensional accuracy and tight tolerances. Owing to its relatively low energy consumption, reduced material waste, and cost-effectiveness, PM has become one of the most widely adopted processing routes for fabricating metal matrix composites (MMCs). In recent years, PM-produced ceramic-reinforced composites have demonstrated significant advantages over

✉ Correspondence
E-mail address: hakanada@gazi.edu.tr

conventionally cast materials, particularly in microstructural control and mechanical performance (Chintada et al., 2022; Kok, 2005; Nayak et al., 2022; Usca et al., 2021). Consequently, numerous composite components employed in aerospace, automotive, defense, and electronics industries are currently manufactured using PM techniques (Kumar et al., 2011). Furthermore, the rapid development of additive manufacturing technologies has further increased the importance of powder-based processing methods in modern manufacturing systems (Gräbner et al., 2022).

Metal matrix composites fabricated by PM generally exhibit lower densities and higher hardness values than their cast counterparts. However, residual porosity is a characteristic feature of the PM process. Despite this limitation, PM offers a significant advantage by facilitating a more homogeneous distribution of reinforcement particles within the matrix (Abdizadeh et al., 2014). In conventional casting methods, reinforcement particles often agglomerate and settle, leading to local variations in physical and mechanical properties. In particular, the agglomeration of ceramic particles in cast aluminum matrix composites may weaken matrix–reinforcement interfacial bonding and adversely affect the composite's overall mechanical performance (Chen & Zhang, 1993).

Aluminum and its alloys are among the most widely used matrix materials for MMCs because of their low density, high specific strength, excellent corrosion resistance, good ductility, and economic availability. Nevertheless, the relatively poor hardness and wear resistance of aluminum limit its use in demanding engineering applications. To overcome these shortcomings, various ceramic reinforcements have been incorporated into aluminum matrices. Silicon carbide (SiC) and alumina (Al_2O_3) are among the most commonly employed reinforcements owing to their high elastic modulus, excellent high-temperature stability, superior strength, and thermal shock resistance (Hull, 1998; Şap et al., 2021a; Şap et al., 2021b; Usca et al., 2022). In addition, their ability to form strong interfacial bonds with aluminum and provide enhanced wear resistance significantly improves the mechanical and tribological properties of aluminum-based composites.

Blast furnace slag (BFS) is an industrial by-product generated during iron production in blast furnaces and consists primarily of CaO, SiO_2, and Al_2O_3 compounds (Dorum et al., 2009; Erdoğdu & Kurbetçi, 2003; Tokyay & Erdoğdu, 2002; Yalçın & Gürü, 2006). Its chemical composition and crystalline structure largely govern the performance of BFS. Depending on the cooling conditions, BFS may exhibit different microstructural characteristics. Rapid cooling of molten slag produces granulated blast furnace slag with a predominantly amorphous (glassy) structure, which exhibits pozzolanic activity when finely ground (Bilim & Atiş, 2011; Erdoğan, 1995). Owing to these characteristics, BFS has been widely used in the construction industry for decades as an additive that improves strength, durability, and long-term service performance (Babu & Kumar, 2000; Douglas & Brvestetr, 1990; Malolepszy & Petri, 1986; Özkan, 2007; Shi & Day, 1992).

The high contents of SiO_2, Al_2O_3, and CaO make BFS a promising low-cost and environmentally friendly ceramic-based reinforcement material. With the growing emphasis on sustainable manufacturing, the utilization of industrial waste products as reinforcements in MMCs has attracted considerable attention from both economic and environmental perspectives. Nevertheless, studies concerning the use of BFS as a reinforcement material in metal matrix composites remain extremely limited. In particular, the effects of BFS on the microstructural evolution, densification behavior, hardness, and wear performance of aluminum matrix composites have not yet been comprehensively investigated.

Dorum et al. (2009) examined the physical, chemical, and mineralogical characteristics of ground granulated blast-furnace slag-blended cements and reported that BFS significantly influenced the hydration behavior and microstructural development. Similarly, Binici et al. (2016) demonstrated that incorporating BFS improved the wear resistance and impermeability of concrete. Saran (2007) reported that ground granulated blast-furnace slag enhanced the durability of concrete and contributed positively to corrosion resistance. These studies collectively indicate that BFS can serve as a performance-enhancing constituent in engineering materials.

Despite these promising findings, research focusing on BFS-reinforced metal matrix composites remains scarce. One of the few studies directly related to MMCs was conducted by Şanlı (2017), who employed Al6061 alloy as the matrix material and investigated the use of blast furnace slag alongside conventional ceramic reinforcements such as SiC and Al_2O_3. The composites were fabricated using a two-stage stir casting process, and their porosity, hardness, microstructure, and fatigue behavior were evaluated. The results revealed that BFS significantly improved hardness and enhanced fatigue strength up to certain reinforcement levels. However, BFS-reinforced composites exhibited higher porosity than composites reinforced with conventional SiC and Al_2O_3 particles. Furthermore, the study focused on an Al6061 alloy matrix, leaving the interaction between BFS and pure aluminum, as well as its influence on microstructural and mechanical properties, largely unexplored.

To the best of the authors' knowledge, studies investigating BFS as the sole reinforcement in pure aluminum matrix composites fabricated by powder metallurgy are not available in the open literature. In addition, the combined influence of BFS content on densification behavior, microstructural evolution, hardness, and wear performance has not been

systematically evaluated. Therefore, a significant knowledge gap remains regarding the effectiveness of BFS as a sustainable reinforcement material for pure aluminum-based composites.

In addition, numerous studies have investigated the effects of ceramic reinforcements on aluminum matrix composites. Şenel (2020) produced aluminum matrix composites reinforced with varying amounts of B_4C and Al_2O_3 via powder metallurgy and reported significant increases in hardness and compressive strength with increasing reinforcement content. In particular, B_4C-reinforced composites exhibited a denser microstructure and superior mechanical performance. These findings confirm the effectiveness of ceramic reinforcements in enhancing the properties of aluminum-based composites.

Similarly, Özer et al. (2024) investigated the influence of different sintering techniques on the density, hardness, and wear behavior of Al-15Si-2.5Cu-0.5Mg/B_4C composites produced by powder metallurgy. The authors reported that porosity was critical to the mechanical and tribological performance of the composites and demonstrated that increased porosity adversely affected both hardness and wear resistance. Their findings highlighted the strong relationship between densification behavior, microstructural integrity, and wear performance in particle-reinforced aluminum matrix composites.

Based on the available literature, although blast furnace slag has been extensively used in construction materials, its application as a reinforcement in metal matrix composites has received limited attention. The microstructural modifications induced by BFS and their effects on the density, hardness, and wear behavior of aluminum matrix composites remain poorly understood. Moreover, most existing studies have focused on aluminum alloys rather than pure aluminum matrices.

Unlike the limited number of available studies that mainly employed aluminum alloys and casting-based production routes, the present work focuses on pure aluminum matrix composites produced by powder metallurgy and reinforced exclusively with varying BFS contents. This approach enables a systematic evaluation of the relationship between BFS addition, densification characteristics, microstructural development, hardness, and wear resistance.

Therefore, investigating the behavior of BFS in pure aluminum matrix composites is of both scientific and practical significance. In the present study, pure aluminum matrix composites with varying BFS contents were fabricated via powder metallurgy. The effects of BFS content on relative density, microstructure, hardness, and wear behavior were systematically investigated. The novelty of this study lies in the use of blast furnace slag, an industrial waste material, as a low-cost, environmentally sustainable reinforcement in pure aluminum matrix composites, and in the comprehensive assessment of its effects on both physical and tribological properties. Furthermore, the feasibility of using blast-furnace slag as a low-cost, sustainable reinforcement material for aluminum matrix composites was evaluated, and the optimal reinforcement level was determined.

2. Experimental Studies

2.1. Material

In this study, aluminum (Al) powder was used as the matrix material, and blast-furnace slag (BFS) was employed as the reinforcement for the fabrication of aluminum matrix composites. The Al powder used as the matrix material had a purity of 99.9%, a particle size smaller than 75 μm, and was supplied by Nanokar. The BFS used as the reinforcement material had a particle size smaller than 45 μm, a density of 2.80 g/cm³, and was obtained from Ereğli Iron and Steel Works (ERDEMİR). The chemical composition of the blast furnace slag used as the reinforcement material is presented in Table 1.

Table 1. Chemical composition of the BFS used as reinforcement material.

Compound	SiO_2	Fe_2O_3	Al_2O_3	CaO	MgO	Na_2O	K_2O	SO_3	TiO_2	P_2O_5
Wt. %	38.26	1.07	16.44	33.9	7.29	0.58	1.1	0.35	1.01	-

2.2. Fabrication of Composite Samples

Different reinforcement contents were selected to investigate the effect of blast furnace slag (BFS) on the properties of pure aluminum matrix composites over a wide composition range. Accordingly, composite samples containing 0.125, 0.25, 0.50, 1, 2, 4, 8, 12, and 16 wt.% BFS was prepared by powder metallurgy. The composition ratios of the fabricated Al–BFS composite samples are presented in Table 2.

The Al and BFS powders were weighed according to the predetermined compositions and mixed in a Retsch PM100 planetary ball mill at a rotational speed of 300 rpm for 90 min using a powder-to-ball weight ratio of 1:10. Following the mixing process, the powder mixtures were compacted into cylindrical specimens with a diameter of 10 mm and a height of 15 mm. Compaction was performed by uniaxial cold pressing under a pressure of 600 MPa.

The green compacts obtained after pressing were subsequently sintered at 600 °C for 90 min under an argon atmosphere. The processing parameters employed for the fabrication of the composite materials are summarized in Table 3.

Table 2. Composition ratios of the Al–BFS composite samples.

Specimens	Al %	BFS %
S0	100	-
S1	99.875	0.125
S2	99.750	0.250
S3	99.500	0.500
S4	99.000	1.000
S5	98.000	2.000
S6	96.000	4.000
S7	92.000	8.000
S8	88.000	12.000
S9	84.000	16.000

Table 3. Processing parameters used for the fabrication of Al–BFS composite samples.

Parameter	Value
Powder-to-ball ratio	1/10
Mixing speed	300 rpm
Mixing time	90 min
Compaction pressure	600 MPa
Sintering atmosphere	Argon atmosphere
Sintering temperature	600°C
Sintering time	90 min

Figure 1. Macroscopic appearance of the Al–BFS composite samples produced with different BFS reinforcement contents.

Figure 1 shows the macroscopic appearance of the Al–BFS composite samples produced using the processing parameters given in Table 3. Visual examination revealed no evidence of macroscopic defects, including cracks, fractures, or shape distortions, indicating that the selected powder metallurgy processing parameters were sufficient to produce sound composite specimens across the entire composition range.

2.3. Microstructural and Mechanical Characterization

Prior to microstructural and mechanical characterization, the fabricated composite samples were prepared in accordance with standard metallographic procedures. The samples were mounted using an APM Opal 460 mounting machine and subsequently ground on an APM Saphir 330 grinding and polishing system with SiC abrasive papers of grit sizes 120, 240, 400, 800, 1200, and 2500. Final polishing was performed using 6 µm and 3 µm monocrystalline diamond suspensions. To reveal the microstructure, the polished surfaces were etched using a reagent consisting of 5 mL HNO_3, 3 mL HCl, 2 mL HF, and 190 mL distilled water.

The theoretical densities of the Al–BFS composite samples were calculated using the rule of mixtures. In contrast, the experimental densities were determined using the liquid displacement method, in accordance with Archimedes' principle. Relative density and porosity values were subsequently calculated from the theoretical and experimental density results. The equations used to determine the theoretical density, experimental density, relative density, and porosity are presented in Eqs. (1)–(4), respectively.

$$\rho_T = [(\%w_m.\rho_m) + (\%w_R.\rho_R)] \quad (1)$$

$$\rho_E = [m_D/(m_S - m_{SIW})]\rho_W \quad (2)$$

$$\rho_R = (\rho_E/\rho_T) \times 100 \quad (3)$$

$$\%P = [1 - (\rho_E/\rho_T)] \times 100 \quad (4)$$

In these equations, ρ_T, ρ_E, ρ_R, and P represent the theoretical density, experimental density, relative density, and porosity,

respectively. The terms ρ_m and ρ_r denote the densities of the matrix and reinforcement materials, while w_m and w_r represent the weight fractions of the matrix and reinforcement, respectively. Furthermore, m_D, m_S, and m_{SIW} correspond to the dry mass, saturated mass, and suspended mass in water of the composite specimen, respectively, whereas ρ_W represents the density of water.

Microstructural examinations were carried out using a Leica DMI5000M optical microscope equipped with a Leica DFC 320 digital camera. Optical micrographs were obtained at a magnification of 100×.

The macrohardness values of the composite samples were determined using an Emcotest DuraVision 200 hardness tester. For each sample, measurements were taken from five different locations, and the average values were reported. Hardness tests were performed according to the Brinell method using a 2.5-mm-diameter ball indenter under an applied load of 31.25 kg.

The wear behavior of the composite samples was evaluated using a UTS T10/20 tribometer operating in a pin-on-disk configuration. A Hardox 450 steel disk with a diameter of 120 mm and a thickness of 10 mm was used as the counterface material. Wear tests were conducted under an applied load of 10 N, a sliding speed of 1 m/s, and a sliding distance of 1000 m.

3. Results and Discussion

The effects of blast furnace slag (BFS) reinforcement on the physical, microstructural, mechanical, and tribological properties of aluminum matrix composites were systematically investigated. Relative density, optical microscopy, hardness, and wear test results were analyzed to evaluate the influence of reinforcement content on composite performance. The experimental findings are presented and discussed in the following sections with reference to relevant literature.

3.1. Density Measurements

The theoretical and experimental densities of the Al–BFS composite samples were determined using Eqs. (1) and (2), respectively, and the corresponding results are presented in Figure 2. Based on these density values, the relative density and porosity of the composites were calculated according to Eqs. (3) and (4). The calculated relative density and porosity values are shown in Figure 3.

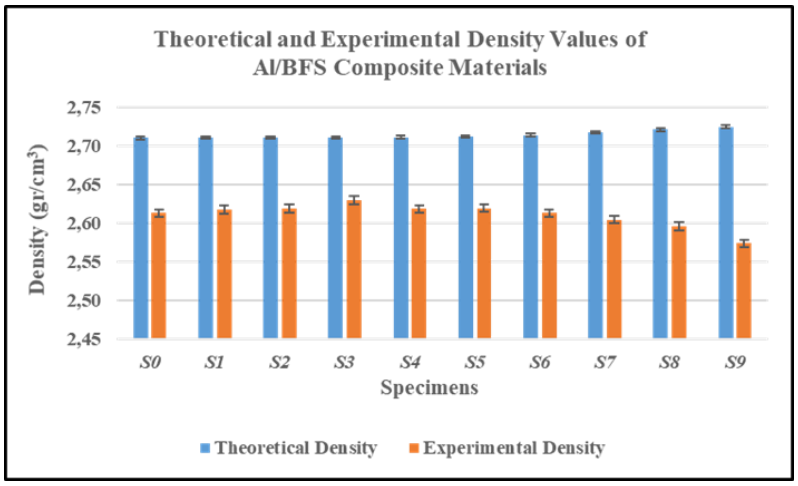

Figure 2. Variation of theoretical and experimental densities of Al–BFS composites as a function of BFS reinforcement content.

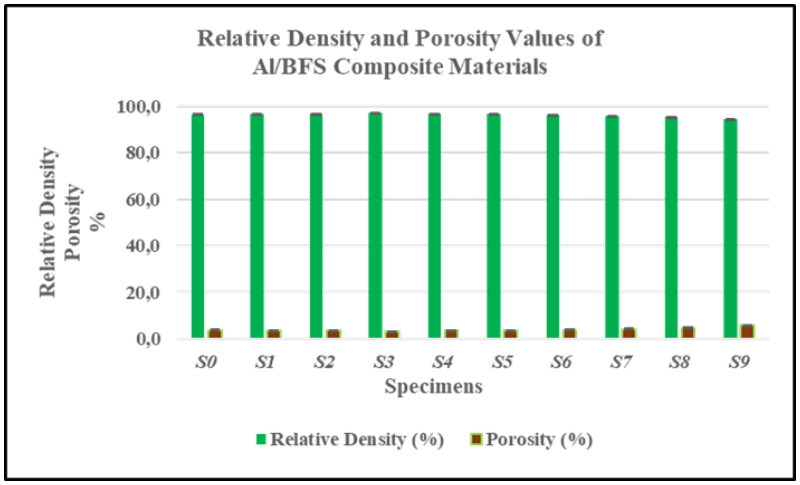

Figure 3. Relative density and porosity values of the Al–BFS composite samples.

Figure 2 shows the theoretical and experimental density values of the Al–BFS composites. As shown, the theoretical and experimental densities exhibited similar trends across the investigated composition range. Since the density of BFS (2.80 g/cm³) is very close to that of the aluminum matrix (2.71 g/cm³), increasing the BFS content resulted in only a slight increase in the theoretical density. Accordingly, the theoretical density values varied within a narrow range of approximately 2.71–2.73 g/cm³ for all compositions.

Examination of the experimental density results revealed that the density values remained relatively close to the theoretical values at BFS contents of 2–4 wt.%. However, a noticeable decrease in experimental density was observed as the BFS content increased beyond this range. In particular, composites containing 8, 12, and 16 wt.% BFS exhibited lower experimental density values, indicating a deterioration in densification behavior as reinforcement content increased. This behavior can be attributed to intensified particle–particle interactions, the formation of interfacial voids between the aluminum matrix and BFS particles, and restricted diffusion during sintering. Consequently, higher BFS contents hindered effective particle bonding and reduced the overall densification efficiency of the composites.

Furthermore, the experimental density values were lower than the corresponding theoretical values for all compositions. This difference indicates residual porosity that could not be eliminated despite the compaction and sintering inherent to powder metallurgy. The increasing discrepancy between theoretical and experimental density values at higher BFS contents suggests increased porosity in the composite structure. These findings are consistent with the relative density, porosity, and optical microscopy results presented in the subsequent sections and indicate that increasing BFS content adversely affects densification and microstructural integrity.

The relative density and porosity values of the Al–BFS composites are presented in Figure 3. The results show that all samples exhibited relatively high relative density values, ranging from approximately 95% to 98%. The high relative density of the unreinforced aluminum sample indicates that the selected compaction and sintering parameters achieved effective densification. In addition, the relative density values remained largely low to moderate for BFS contents (%2–4), and some compositions exhibited values comparable to those of the unreinforced sample. This behavior suggests that BFS particles were successfully incorporated into the aluminum matrix without significantly impairing densification.

Nevertheless, a gradual decrease in relative density, accompanied by an increase in porosity, was observed as BFS content increased. This trend became more pronounced in composites containing 8–16 wt—% BFS. The increase in porosity can be attributed to enhanced particle–particle interactions, the formation of interfacial voids, and the partial restriction of densification mechanisms during sintering. Moreover, the reduction in matrix continuity and the tendency of reinforcement particles to agglomerate at high BFS contents may further promote pore formation.

Overall, the relative density values exceeding 95% demonstrate the effectiveness of the selected powder metallurgy processing parameters. However, the increase in porosity and the reduction in relative density observed at high BFS contents are consistent with the agglomeration tendencies identified in the optical microscopy analysis. They are expected to play a significant role in the subsequent hardness and wear behavior of the composites. These findings indicate that the addition of BFS does not significantly affect densification up to a certain reinforcement level. In contrast, excessive BFS content leads to a partial deterioration in the microstructural integrity of the composites.

3.2. Microstructural Analysis of Al–BFS Composite Materials

Figure 4 presents optical microscopy (OM) images at 100× magnification of the Al–BFS composite materials. These micrographs were used to evaluate the effect of BFS reinforcement content on the microstructural evolution of the composites.

Examination of the optical micrographs presented in Figure 4 reveals that BFS reinforcement significantly influenced the microstructure of the aluminum matrix. The unreinforced Al sample (S0) exhibited a relatively homogeneous microstructure with well-defined grain boundaries and high matrix continuity. With the addition of BFS, dark-colored regions corresponding to the reinforcement phase became visible within the matrix, and their volume fraction gradually increased as BFS content increased. At low reinforcement levels (0.125–1 wt.% BFS), the BFS particles appeared to be generally well distributed throughout the matrix, while matrix continuity was largely preserved, and no significant agglomeration tendency was observed. These observations indicate that the BFS particles were effectively surrounded by the aluminum matrix at low reinforcement contents, resulting in good microstructural integrity.

With increasing BFS content (2–4 wt.% BFS), the reinforcement phase became more pronounced within the microstructure, and localized particle accumulations began to appear as a result of the higher reinforcement concentration. In these samples, the interaction between the matrix and reinforcement phases appeared to increase, while the overall microstructural homogeneity was largely maintained. Nevertheless, the increase in reinforcement content made densification during sintering more challenging, resulting in the formation of small, isolated pores in certain regions of the microstructure.

A more pronounced change in the microstructure was observed in the composites containing high BFS contents (8–16 wt.% BFS). In particular, samples S7, S8, and S9 exhibited a substantial increase in the volume fraction of the dark reinforcement regions. In addition, the reinforcement particles tended to cluster in certain areas, leading to agglomerates and a partial reduction in matrix continuity. The decrease in the interparticle spacing at high reinforcement levels, together with insufficient diffusion during sintering, is believed to promote pore formation within the composite structure. The irregular voids and dark, clustered regions observed in the micrographs indicate that densification was adversely affected at high BFS contents. This interpretation is further supported by the experimental density and porosity results presented in the previous section.

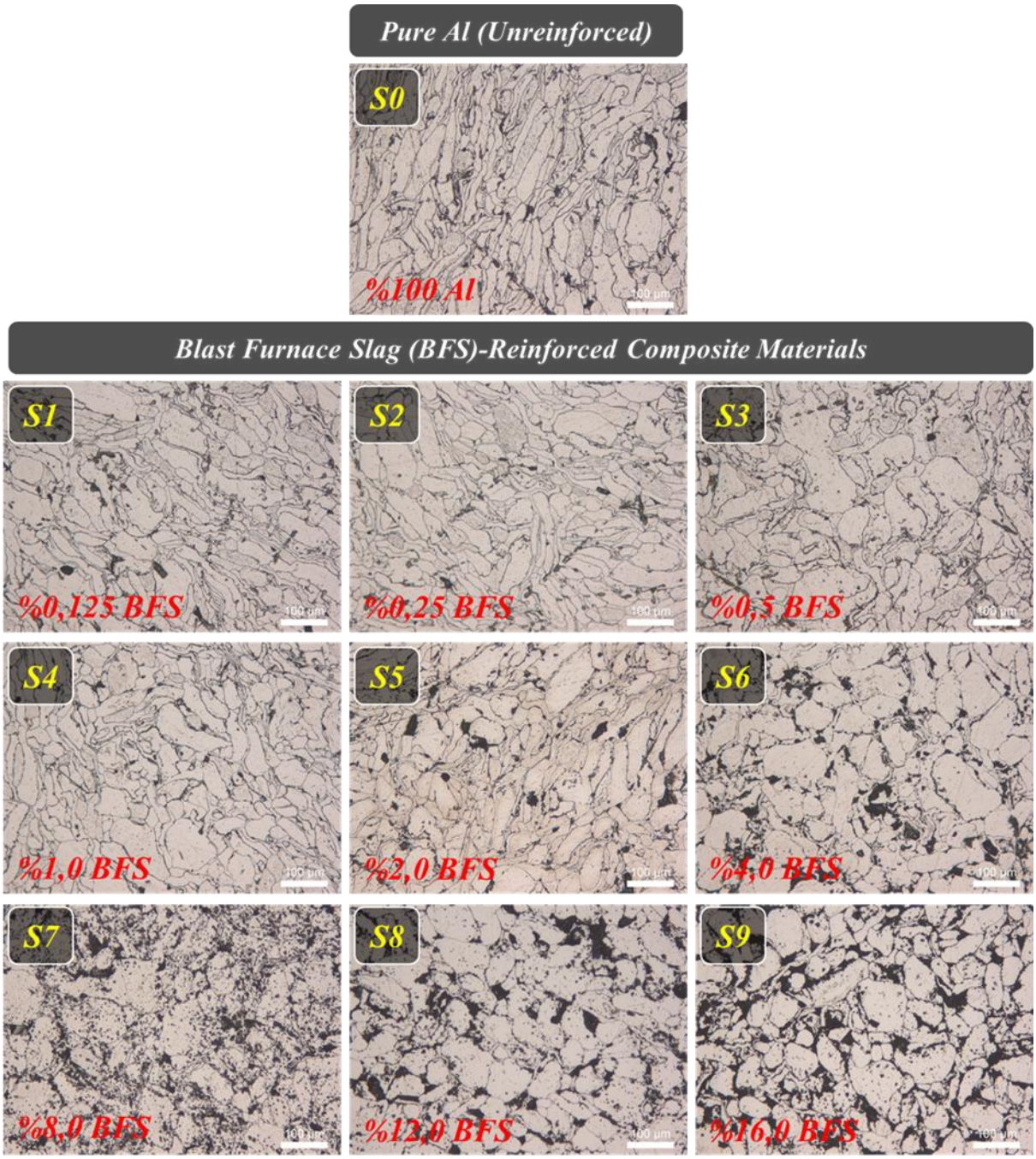

Figure 4. Optical microscopy (OM) images of the Al–BFS composite materials at 100× magnification.

Another noteworthy feature observed in the micrographs is a morphological change in the matrix structure as BFS content increases. The unreinforced aluminum sample exhibited relatively coarse and elongated grains, whereas the microstructure became progressively finer and more fragmented as the BFS content increased. This behavior may be

attributed to the ability of BFS particles to partially restrict grain growth during sintering by acting as grain-boundary barriers. However, this interpretation should be supported by quantitative grain size measurements for definitive confirmation.

Overall, the optical microscopy results demonstrate that BFS reinforcement significantly influences the microstructural characteristics of the aluminum matrix composites. While low- and moderate-BFS contents resulted in a relatively homogeneous particle distribution and good microstructural integrity, higher reinforcement levels promoted particle agglomeration and pore formation. Consequently, BFS has the potential to enhance the performance of aluminum matrix composites; however, the beneficial effects may be limited at high reinforcement levels due to increased agglomeration and porosity. When considered together with the density, hardness, and wear results, the present findings indicate that not only the reinforcement content but also the homogeneity of the reinforcement particle distribution and the porosity level play critical roles in determining the overall performance of Al–BFS composites.

3.3. Hardness Measurements

The hardness behavior of the Al–BFS composites was investigated to evaluate the influence of BFS reinforcement on the materials' resistance to plastic deformation. Figure 5 illustrates the variation in macrohardness values with increasing BFS content.

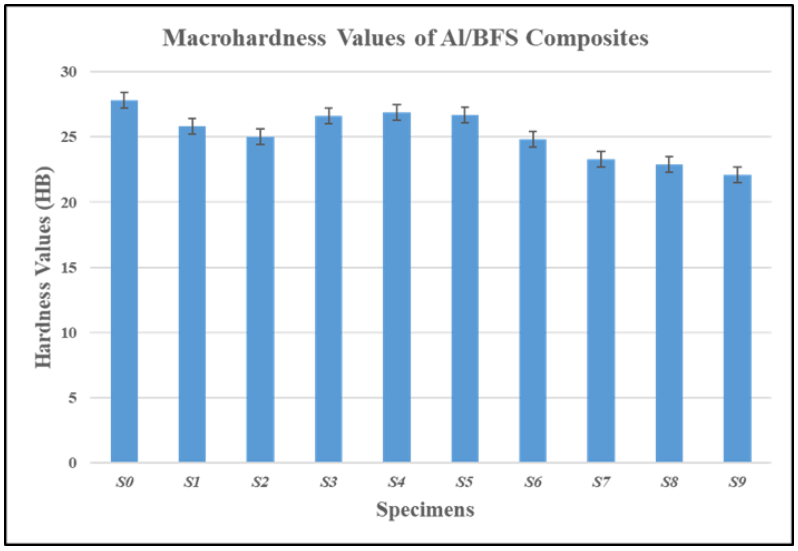

Figure 5. Variation of macrohardness values of Al–BFS composites with BFS reinforcement content.

Figure 5 shows the variation in the macrohardness values of the Al–BFS composites. The unreinforced aluminum sample (S0) exhibited the highest hardness value, approximately 27.8 HB. A slight decrease in hardness was observed at low BFS contents (0.125–0.5 wt.%). However, the hardness values increased again for the composites containing 1–4 wt.% BFS (S4–S6), reaching levels comparable to those of the unreinforced sample. In particular, the hardness values obtained for the composites containing 2 and 4 wt.% BFS can be attributed to the relatively homogeneous distribution of the reinforcement particles within the matrix and their contribution to the load-transfer mechanism. Moreover, the high relative density and low porosity values observed in these samples contributed to the preservation of hardness.

Nevertheless, a pronounced decrease in hardness was observed when the BFS content exceeded 8 wt.%. The lowest hardness value, approximately 22 HB, was recorded for the composite containing 16 wt.% BFS (S9). This reduction can primarily be attributed to the decrease in relative density and the increase in porosity identified in the density measurements, as well as the microstructural changes observed in the optical micrographs. In particular, the tendency of reinforcement particles to agglomerate, the reduction in matrix continuity, and the increase in pore content at high BFS levels promoted stress concentration under the applied load, thereby reducing resistance to plastic deformation. Since increased porosity reduces the effective load-bearing cross-sectional area in powder metallurgy composites, it directly contributes to the deterioration of hardness.

Optical microscopy observations revealed a relatively homogeneous microstructure at BFS contents of 2–4 wt.%, whereas particle agglomeration and irregular pore formation became increasingly evident at higher reinforcement levels. These findings are consistent with the increase in porosity determined from the density measurements and support the observed reduction in hardness. Although BFS is a ceramic-rich reinforcement containing hard oxide phases that would be expected to improve hardness, the potential strengthening effect was counteracted by the formation of microstructural defects and the deterioration of densification behavior at BFS

contents exceeding 4 wt.%. Consequently, the adverse effects of porosity and particle agglomeration became dominant at higher reinforcement levels, leading to a reduction in the overall mechanical performance of the composites.

Overall, the results indicate that the effect of BFS reinforcement on hardness is not linear. The hardness behavior of the composites is governed not only by the reinforcement content but also by the degree of densification, porosity level, and distribution homogeneity of the reinforcement particles within the matrix. While the relatively homogeneous microstructure and high relative density values obtained at BFS contents of 2–4 wt.% contributed to maintaining hardness performance, increased porosity and particle agglomeration at BFS contents above 4 wt.% resulted in a significant reduction in hardness. Considering the combined effects of densification behavior, microstructural integrity, and hardness performance, BFS contents of 2–4 wt.% provided the most favorable mechanical performance among the investigated composites.

3.4. Wear Tests

Pin-on-disk wear tests were conducted to evaluate the tribological behavior of the Al–BFS composite materials. The wear performance of the composites was assessed using weight-loss measurements obtained after testing, and the corresponding results are presented in Figure 6.

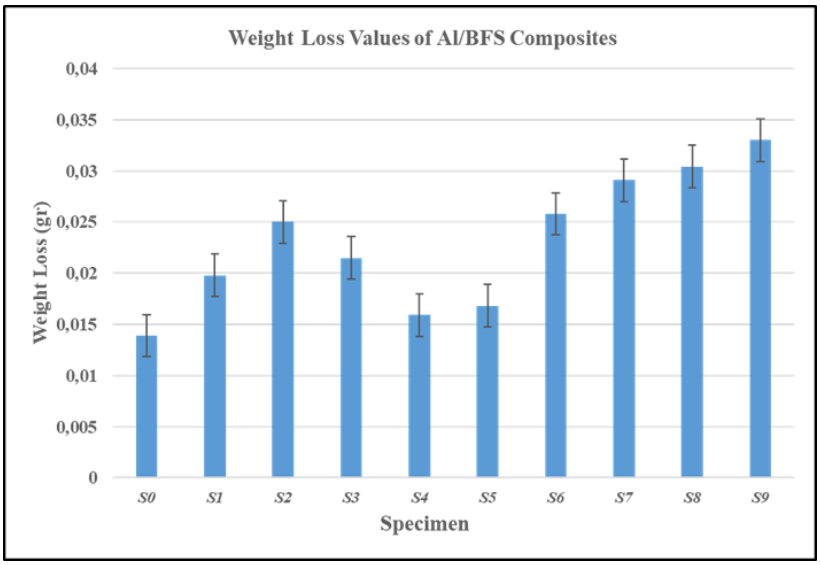

Figure 6. Weight loss values of the Al–BFS composite materials after wear testing.

Figure 6 illustrates the wear behavior of the Al–BFS composites in terms of weight loss after wear testing. The results indicate that the BFS reinforcement content significantly influenced the wear performance of the composites. The lowest weight loss, approximately 0.014 g, was obtained for the unreinforced aluminum sample (S0). In general, weight loss increased with increasing BFS content, indicating a gradual deterioration in wear resistance. This trend became particularly pronounced in the composites containing 8–16 wt.% BFS, with the highest weight loss value of approximately 0.033 g recorded for the S9 sample containing 16 wt.% BFS.

The wear results are more meaningful when evaluated alongside the density and porosity measurements. As discussed in the previous sections, increasing BFS content resulted in lower experimental and relative density values, accompanied by a noticeable increase in porosity. In powder metallurgy composites, porosity reduces the effective load-bearing area and facilitates material removal from the surface during sliding contact. Therefore, the increase in wear loss observed at high BFS contents can be largely attributed to the increased porosity within the composite structure.

The optical microscopy observations further support this interpretation. At low reinforcement levels, the BFS particles were relatively homogeneously distributed throughout the matrix. In contrast, higher reinforcement contents resulted in particle agglomeration and the formation of irregular pores. In particular, the agglomerated regions observed in samples S7, S8, and S9 may have acted as stress concentration sites during wear, thereby accelerating particle pull-out and surface damage. As a result, more material was removed from the worn surface, leading to higher weight-loss values.

A similar trend was observed when the wear behavior was compared with the hardness results. While the hardness values of the composites containing 2–4 wt.% BFS remained comparable to those of the unreinforced aluminum sample, a significant reduction in hardness was observed at higher reinforcement levels (≥8 wt.% BFS). Since wear resistance is generally correlated with hardness, the reduction in hardness contributed to the increased wear loss. Furthermore, the increased porosity and particle agglomeration observed at higher BFS contents promoted microstructural heterogeneity, thereby accelerating material removal during sliding. Notably,

samples S7–S9, which exhibited the lowest hardness values, also showed the highest weight loss values, indicating a strong relationship between hardness degradation and wear performance.

Overall, the results demonstrate that the effect of BFS reinforcement on wear behavior is not governed solely by reinforcement content. Instead, the tribological performance of the composites is strongly influenced by microstructural homogeneity, porosity level, and densification behavior. The composites containing 2–4 wt.% BFS exhibited the most favorable wear performance among the reinforced samples, whereas BFS contents of 8 wt.% and above adversely affected wear resistance because of increased porosity, particle agglomeration, and reduced hardness. Consequently, increasing the BFS content beyond 4 wt.% did not improve the tribological performance of the Al–BFS composites; rather, it led to a progressive deterioration in wear resistance despite the ceramic-rich nature of the reinforcement phase.

4. Conclusion

In this study, pure aluminum matrix composites reinforced with varying amounts of blast-furnace slag (BFS) were successfully fabricated via powder metallurgy, and the effects of BFS addition on density, microstructure, hardness, and wear behavior were systematically investigated. The results demonstrated that BFS reinforcement significantly influences the microstructural, mechanical, and tribological properties of aluminum matrix composites, and that these effects strongly depend on the reinforcement content.

Density measurements revealed that the addition of BFS had only a minor influence on the theoretical density of the composites. However, increasing the BFS content resulted in lower experimental and relative density values and higher porosity levels. Although all composites exhibited relative densities above 95%, the increase in porosity observed at BFS contents of 8–16 wt.% indicated a gradual deterioration in densification behavior. Optical microscopy observations supported these findings, showing relatively homogeneous microstructures at BFS contents of 2–4 wt.%. In contrast, particle agglomeration, irregular pore formation, and reduced matrix continuity became increasingly evident at BFS contents of 8 wt.% and above.

The mechanical and tribological properties were found to be closely related to these microstructural changes. While the hardness values of the composites containing 2–4 wt.% BFS remained comparable to those of the unreinforced aluminum sample, a significant reduction in hardness was observed at BFS contents of 8 wt.% and above due to increased porosity and particle agglomeration. Similarly, wear tests revealed a progressive increase in weight loss with increasing BFS content. The deterioration in wear resistance was associated with increased porosity, reduced matrix continuity, and microstructural heterogeneity, all of which contributed to the observed reduction in hardness and accelerated material removal during sliding.

Overall, the results indicate that the performance of Al–BFS composites is governed not only by the amount of reinforcement but also by the degree of densification, the porosity level, and the homogeneity of the distribution of reinforcement particles within the matrix. The findings demonstrate that blast furnace slag can be used as a low-cost, environmentally sustainable reinforcement material in aluminum matrix composites. However, excessive BFS additions promote microstructural defects that adversely affect the mechanical and tribological performance of the composites. Considering all experimental results together, optimum performance was achieved at low to moderate BFS contents. In contrast, high reinforcement levels should be avoided due to their detrimental effects on densification, hardness, and wear resistance.

Acknowledgment

This study was supported by the Scientific and Technological Research Council of Türkiye (TÜBİTAK) through the 2209-A University Students Research Projects Support Program. The authors gratefully acknowledge the support provided by TÜBİTAK BİDEB (Scientist Support Programs Presidency).

Conflict of Interest

The authors declare that they have no conflict of interest.

Disclosure of Generative AI Use

An AI tool was used in language editing and grammar refinement during the preparation of this article.

References

Abdizadeh, H., Ebrahimifard, R., & Baghchesara, M. A. (2014). Investigation of microstructure and mechanical properties of nano MgO reinforced Al composites manufactured by stir casting and powder metallurgy methods: A comparative study. *Composites Part B: Engineering*, *56*, 217-221. https://doi.org/10.1016/j.compositesb.2013.08.023

Babu, K. G., & Kumar, V. S. R. (2000). Efficiency of GGBS in concrete. *Cement and Concrete Research*, *30*(7), 1031-1036. https://doi.org/10.1016/S0008-8846(00)00271-4

Bilim, C., & Atiş, C. D. (2011). Öğütülmüş granüle yüksek fırın cürufu içeren harçların aşınma ve mukavemet özellikleri. *Politeknik Dergisi*, *14*(2), 101-107. (In Turkish)

Binici, H., Görür, E. B., & Durgun, M. Y. (2016). Yüksek fırın cürufu ve bazaltik pomza katkılı betonların mekanik

aşınması ve su geçirimliliği. *Yapı Teknolojileri Elektronik Dergisi*, *6*(1), 1-10. (In Turkish)

Chen, R., & Zhang, G. (1993). Casting defects and properties of cast A356 aluminium alloy reinforced with SiC particles. *Composites Science and Technology*, *47*(1), 51-56. https://doi.org/10.1016/0266-3538(93)90095-X

Chintada, S., Dora, S. P., Kare, D., & Pujari, S. R. (2022). Powder metallurgy versus casting: Damping behavior of pure aluminum. *Journal of Materials Engineering and Performance*, *31*(11), 9122-9128. https://doi.org/10.1007/s11665-022-06886-2

Dorum, A., Koçak, Y., Yılmaz, B., & Uçar, A. (2009). Yüksek fırın cürufunun çimento yüzey ve hidratasyona etkileri. *Journal of Science and Technology of Dumlupınar University*, (019), 47-58. (In Turkish)

Douglas, E., & Brandstetr, J. (1990). A preliminary study on the alkali activation of ground granulated blast-furnace slag. *Cement and Concrete Research*, *20*(5), 746-756. https://doi.org/10.1016/0008-8846(90)90008-L

Erdoğan, T. Y. (1995). *Öğütülmüş granüle yüksek fırın cürufu ve kullanımı*. TMMOB İnşaat Mühendisleri Odası Bildiriler Kitabı, Endüstriyel Atıkların İnşaat Sektöründe Kullanılması Sempozyumu. (In Turkish)

Erdoğdu, Ş., & Kurbetçi, Ş. (2003). Betonun performansına sağladıkları etkinlik açısından kimyasal ve mineral katkı maddeleri. *Türkiye Mühendislik Haberleri*, *426*(4), 115-120. (In Turkish)

Gräbner, M., Wiche, H., Treutler, K., & Wesling, V. (2022). Micromagnetic properties of powder metallurgically produced Al composites as a fundamental study for additive manufacturing. *Applied Sciences*, *12*(13), 6695. https://doi.org/10.3390/app12136695

Hull, D. (1998). *An introduction to composite materials*. Cambridge University Press

Kok, M. (2005). Production and mechanical properties of Al2O3 particle-reinforced 2024 aluminium alloy composites. *Journal of Materials Processing Technology*, *161*(3), 381-387. https://doi.org/10.1016/j.jmatprotec.2004.07.068

Kumar, D. R., Loganathan, C., & Narayanasamy, R. (2011). Effect of glass in aluminum matrix on workability and strain hardening behavior of powder metallurgy composite. *Materials & Design*, *32*(4), 2413-2422. https://doi.org/10.1016/j.matdes.2010.12.008

Malolepszy, J., & Petri, M. (1986). *High strength slag alkaline binders*. 8th International Congress on the Chemistry of Cement. Rio de Janeiro.

Nayak, K. C., Rane, K. K., Date, P. P., & Srivatsan, T. S. (2022). Synthesis of an aluminum alloy metal matrix composite using powder metallurgy: Role of sintering parameters. *Applied Sciences*, *12*(17), 8843. https://doi.org/10.3390/app12178843

Özer, M., Kaplan, Y., Özer, A., & Aksoz, S. (2024). Influence of different sintering techniques on the wear properties of Al-15Si-2.5 Cu-0.5 Mg/B4C composites. *Science of Sintering*, *56*(3), 269-283. https://doi.org/10.2298/SOS231003060O

Özkan, Ö. (2007). Atık cam ve yüksek fırın cürufu katkılı harçların özellikleri. *Gazi Üniversitesi Mühendislik Mimarlık Fakültesi Dergisi*, *22*(1). (In Turkish)

Şanlı, A. (2017). *Al 6061 matrisli SiC, Al2O3 ve yüksek fırın cürufu takviyeli hibrit kompozitlerin yorulma davranışlarının incelenmesi* (Master's thesis, Bartın University). (In Turkish)

Şap, S., Turgut, A., & Uzun, M. (2021a). Investigation of microstructure and mechanical properties of Cu/Ti–B–SiC_p hybrid composites. *Ceramics International*, *47*(21), 29919-29929. https://doi.org/10.1016/j.ceramint.2021.07.165

Şap, S., Uzun, M., Usca, Ü. A., Pimenov, D. Y., Giasin, K., & Wojciechowski, S. (2021b). Investigation on microstructure, mechanical, and tribological performance of Cu base hybrid composite materials. *Journal of Materials Research and Technology*, *15*, 6990-7003. https://doi.org/10.1016/j.jmrt.2021.11.114

Saran, A. G. (2007). *Öğütülmüş granüle yüksek fırın cürufunun betonun durabilite özelliklerine etkisi* (Master's thesis, İstanbul Technical University). (In Turkish)

Şenel, M. C. (2020). Toz metalürjisi yöntemiyle üretilen saf Al ve Al-B4C, Al-Al2O3 kompozitlerin mekanik ve mikroyapı özelliklerinin karşılaştırılması. *Gümüşhane Üniversitesi Fen Bilimleri Dergisi*, *10*(3), 783-795. https://doi.org/10.17714/gumusfenbil.689359 (In Turkish)

Shi, C. J., & Day, R. L. (1992). *Comparison of the microstructure and performance of alkali-slag and Portland cement pastes*. 9 th International Congress on the Chemistry of Cement. New Delhi.

Tokyay, M., & Erdoğdu, K. (2002). *Cüruflar ve cüruflu çimentolar*. TÇMB. (In Turkish)

Usca, Ü. A., Şap, S., Uzun, M., Giasin, K., & Pimenov, D. Y. (2022). Evaluation of mechanical and tribological aspect of self-lubricating Cu-6Gr composites reinforced with SiC–WC hybrid particles. *Nanomaterials*, *12*(13), 2154. https://doi.org/10.3390/nano12132154

Usca, Ü. A., Uzun, M., Kuntoğlu, M., Şap, S., Giasin, K., & Pimenov, D. Y. (2021). Tribological aspects, optimization and analysis of Cu-B-CrC composites fabricated by powder metallurgy. *Materials*, *14*(15), 4217. https://doi.org/10.3390/ma14154217

Yalçın, H., & Gürü, M. (2006). *Çimento ve beton*. Palme Yayıncılık. (In Turkish)

JAASCI
http://jaasci.com
JOURNAL OF ADVANCED APPLIED SCIENCES
e-ISSN: 2979-9759
PRENSİP
https://prensip.gen.tr

RESEARCH ARTICLE

Tensile Behavior of Injection-Molded PLA Composites Reinforced with Turkey Feather Fibers at Different Loadings

Momin Alihuseyinov[1] • Ugur Soykan[2] • Turker Akkoyunlu[3]✉ • Gurcan Yildirim[1]

[1]Bolu Abant İzzet Baysal University, Faculty of Engineering, Department of Mechanical Engineering, Bolu/Türkiye
[2]Bolu Abant İzzet Baysal University, Yeniçağa Yaşar Çelik Vocational School, Bolu/Türkiye
[3]Kırıkkale University, Faculty of Engineering and Natural Sciences, Department of Mechanical Engineering, Kırıkkale/Türkiye

ARTICLE INFO

Article History
Received: 18.06.2026
Accepted: 25.06.2026
First Published: 28.06.2026

Keywords
Fiber-matrix adhesion
Mechanical performance
Natural fiber reinforcement
PLA composites

ABSTRACT

This study investigates the development and mechanical performance of environmentally friendly polylactic acid (PLA)-based biocomposites reinforced with turkey feather fibers (TFFs) at different weight fractions (1, 3, 5, 7, and 10 wt.%). The primary aim is to evaluate the potential of poultry waste-derived keratin fibers as sustainable reinforcements for lightweight engineering materials. TFFs were extracted, purified, and incorporated into the PLA matrix via melt mixing followed by injection molding. The mechanical behavior of the resulting composites was assessed through tensile testing, focusing on maximum load, elongation at break, and maximum displacement. The results obtained revealed that the incorporation of TFFs significantly influenced the mechanical properties of PLA matrix. While pure PLA exhibited the highest tensile strength and deformation capability, the addition of fibers generally reduced mechanical performance. Among all the samples, the 3 wt.%-reinforced TFF composite displayed the best balance of mechanical properties, exhibiting the highest tensile load and relatively improved ductility compared to other fiber loadings. However, further increases in fiber content led to a progressive deterioration in tensile properties due to fiber agglomeration, insufficient fiber-matrix adhesion, and increased microstructural defects such as void formation and interfacial debonding. In conclusion, the experimental findings indicate that turkey feather fibers can be effectively utilized as low-cost, renewable reinforcement agents for PLA-based composites, contributing to waste valorization and sustainable material development. The study identifies an optimal fiber loading of approximately 3 wt.% for achieving a balance between mechanical performance and structural integrity, providing useful information for the design of green composite materials for lightweight engineering applications.

Please cite this paper as follows:

Alihuseyinov, M., Soykan, U., Akkoyunlu, T., & Yildirim, G. (2026). Tensile behavior of injection-molded PLA composites reinforced with turkey feather fibers at different loadings. *Journal of Advanced Applied Sciences*, *5*(1), 45-54. https://doi.org/10.61326/jaasci.v5i1.505

1. Introduction

In recent years, the development of lightweight and sustainable engineering materials has become a major research priority in mechanical engineering due to increasing demands for energy efficiency, resource conservation, and environmental responsibility. Composite materials play a critical role in numerous engineering sectors, including automotive, aerospace, construction, packaging, and consumer products, where the reduction of structural weight while maintaining adequate mechanical performance is highly desirable. Lightweight materials contribute directly to reduced fuel consumption, lower greenhouse gas emissions, and improved overall system efficiency throughout the product life cycle. Consequently, the replacement of conventional

✉ Correspondence
E-mail address: turkerakkoyunlu@kku.edu.tr

petroleum-based materials with renewable and biodegradable alternatives has emerged as a key strategy for achieving sustainable manufacturing and circular economy objectives (Ghorbal et al., 2019).

Among biodegradable polymers, PLA has attracted considerable attention because of its renewable origin, biodegradability, biocompatibility, and relatively favorable processing characteristics (Trivedi et al., 2023). Nevertheless, its inherent brittleness, limited impact resistance, and moderate thermal stability restrict its broader engineering applications (Akdogan & Soykan, 2025; Mrajji et al., 2022; Shankar & Netravali, 2025). Reinforcement with natural fibers has therefore become one of the most effective approaches to improve the mechanical performance of PLA-based materials while maintaining their environmental advantages (Murariu & Dubois, 2016). In addition to conventional lignocellulosic fibers, animal-derived fibers have recently gained attention because they provide an opportunity to transform agricultural and food-industry wastes into value-added engineering materials (Mann et al., 2023; Soykan, 2022).

Poultry feathers represent one of the most abundant animal-derived wastes worldwide, with annual generation exceeding two million tonnes (Reddy et al., 2021). Disposal of these residues poses environmental and economic challenges, whereas their utilization as reinforcement materials offers an attractive route for waste valorization and resource recovery (Dutta et al., 2024; Shankar & Netravali, 2025). Owing to their keratin-rich structure and low density, feather fibers possess a unique combination of lightweight characteristics, flexibility, and mechanical stability that can be advantageous for the fabrication of bio-based composites (Akdogan & Soykan, 2024; Mrajji et al., 2022). Furthermore, the incorporation of feather fibers into PLA matrices has been reported to improve mechanical performance, reduce environmental impacts, and lower the density of the resulting composites, making them attractive candidates for sustainable lightweight engineering applications (Aranberri et al., 2017; Baba 6 Özmen, 2017).

Despite the growing interest in feather-reinforced PLA composites, the majority of previous studies have focused on chicken feather fibers, while the potential of turkey feather fibers remains largely unexplored (Khan et al., 2022). Turkey feather barbs are characterized by longer fiber lengths and relatively high strength compared with conventional contour feathers, suggesting their suitability as reinforcement materials for biodegradable polymer matrices 32. Moreover, their distinctive double-sided comb-like morphology and the presence of polar functional groups may promote improved interfacial interactions with PLA, potentially leading to enhanced load transfer and mechanical performance.

Therefore, the present study aims to develop a novel series of PLA-based biocomposites reinforced with different contents of turkey feather fibers and to evaluate their mechanical behavior through tensile testing. By establishing the relationship between turkey feather fiber content and the resulting mechanical properties, this work seeks to contribute to the development of sustainable, lightweight, and high-performance composite materials. From a sustainability perspective, the study promotes the valorization of poultry-processing waste and supports circular economy principles. From a mechanical engineering perspective, it provides insights into the design of environmentally friendly structural materials with potential applications in lightweight components and sustainable product development.

2. Materials and Methods

Commercial polylactic acid materials with a density of 1.24 g/cm^3 and a relative viscosity of 3.1 were supplied by NatureWorks LLC under the trade name Ingeo Biopolymer 6100D. Besides, turkey feathers were used as the primary source of reinforcement fibers. A non-ionic surfactant, Setawet ANY-R2205 was employed as a detergent during the cleaning process when ethanol was used for the disinfection and purification of the fibers. All other chemicals and solvents used in this study were of analytical grade and utilized as received without further purification. As for the preparation of turkey feather fibers (TFFs), the procedure described in our previous studies was followed (Abdur Rahman et al., 2023; Rajendran et al., 2025). Briefly, raw turkey feathers were washed with distilled water and subsequently cleaned using Setawet ANY-R2205 detergent at 40 °C for 1 h to remove contaminants while preserving the fiber microstructure. The cleaned feathers were then disinfected by immersion in ethanol for a duration of 24 h, a process repeated 3 times, and subsequently dried in a vacuum oven at 30 °C for a duration of 24 h. After drying, the barb sections were mechanically separated from the quills according to the method reported by Baron and Schmidt (Barone & Schmidt, 2005), cut into smaller pieces, and sieved through a 400 μm mesh to obtain fibers with a more uniform size distribution. Finally, the TFF-Reinforced PLA composites were prepared by the following procedure. Prior to processing, PLA pellets and TFF compounds were dried under vacuum at 40 °C for the time of 1 h. The composites containing 1, 3, 5, 7, and 10 wt.% TFFs were prepared by melt mixing in a Brabender W50 EHT+ Plastograph EC Plus mixer at 175 °C for 20 min, while neat PLA served as the reference. The samples prepared are accordingly labeled as 1 wt.% PLA-1, 3 wt.% PLA-3, 5 wt.% PLA-5, 7 wt.% PLA-7, and 10 wt.% PLA-10. A reference sample is prepared under identical conditions without turkey feather fibers and was named as pure. The resulting blends were granulated using a Retsch SM-100 knife mill and subsequently injection molded using a Thermo Scientific Haake MiniJet II machine. Molding was performed at a mold temperature of 105 °C and an injector temperature of 175 °C under injection and holding pressures of 650 and 400 bar, respectively. For each

composition, at least five dog-bone specimens (75x12.5x2 mm^3) were produced.

3. Results and Discussion

3.1. Variation of Maximum Load Values

The tensile behavior of the PLA/turkey feather fiber composites was evaluated by analyzing the maximum load (F_{max}) sustained by each specimen during tensile testing. The maximum load represents the highest force that a material can withstand before the onset of catastrophic failure and provides an important indication of the reinforcing efficiency of the incorporated fibers. The obtained results are provided in Table 1. The obtained results were also presented graphically in Figure 1 to enhance the impact of turkey feather fibers on the maximum load parameters. It is seen from the table that the neat PLA (pure reference sample) specimens exhibited the highest tensile performance among all tested materials, with a maximum load of 0.8267 kN, which is higher than those of all fiber-reinforced composites. The result obtained indicated that the unreinforced PLA matrix possesses superior tensile load-bearing capability under the present processing conditions.

Table 1 Change of the maximum load (F_{max}) parameters of turkey feather-reinforced fibers at different weight fractions.

Samples	F_{max} (kN)
Pure	0.8267
%1 PLA-1	0.5304
%3 PLA-3	0.5863
%5 PLA-5	0.548
%7 PLA-7	0.4903
%10 PLA-10	0.4884

The incorporation of turkey feather fibers generally resulted in a reduction in the maximum tensile load. The 1 wt.% TFF composite exhibited F_{max} value of 0.5304 kN, representing a noticeable decrease compared with neat PLA. Increasing the fiber content to 3 wt.% improved the tensile response, with maximum load of 0.5863 kN. This composition exhibited the highest tensile performance among all reinforced specimens, revealing that a moderate amount of turkey feather fibers can contribute positively to load transfer while maintaining sufficient continuity of the PLA matrix. Further increases in fiber content resulted in a gradual deterioration of tensile performance. The 5 wt.% composite exhibited F_{max} value of 0.5480 kN, while the 7 wt.% composite showed a value of 0.4903 kN. The lowest maximum load was obtained for the 10 wt.% composite, which fractured under a load of 0.4498 kN, as provided in Table 1. These results recorded indicted that increasing the turkey feather fiber content beyond the optimum level progressively reduces the tensile load-bearing capacity of the composites.

The relatively superior performance of the 3 wt.% TFF composite displays that this reinforcement level provides the most effective balance between fiber reinforcement and matrix integrity. At low fiber concentrations, the feather fibers are more likely to be uniformly dispersed throughout the PLA matrix, allowing more efficient stress transfer across the fiber-matrix interface. Under these conditions, the fibers can partially impede crack propagation and contribute to load sharing without severely disrupting the continuity of the polymer phase. Consequently, the composite exhibits improved mechanical performance compared with the other reinforced formulations. However, as can be seen from the numerical data obtained, the tensile performance of the composite with a 3% weight ratio remained lower than that of pure PLA, as seen in Figure 1. The relatively limited improvement in tensile performance indicates that the reinforcing potential of the untreated turkey feather fibers was not fully exploited. This behavior is most likely attributable to the weak interfacial adhesion between the hydrophilic keratin-based feather fibers and the relatively hydrophobic PLA matrix. Such inadequate interfacial bonding hinders efficient stress transfer from the matrix to the reinforcing fibers, accordingly limiting their ability to function as effective load-bearing constituents during tensile deformation.

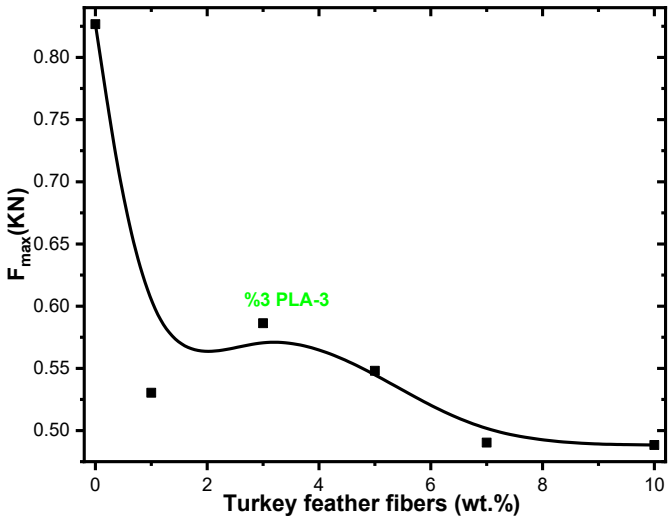

Figure 1. Variation of F_{max} values depending on turkey feather fiber-reinforced composites. Lines represent the general trend to guide the eye.

The gradual decrease in F_{max} observed at fiber contents above 3% can be explained by various microstructural mechanisms. As fiber concentration increases, achieving homogeneous distribution within the polymer matrix becomes increasingly difficult. Fibers tend to clump together, resulting in localized regions of high fiber density surrounded by matrix-deficient areas. These clumped regions act as stress concentration points where cracks can more easily form under applied tensile loads. In addition, higher fiber loadings increase the likelihood of void formation during composite fabrication.

The presence of voids reduces the effective cross-sectional area available to carry tensile loads and promotes premature fracture by facilitating crack nucleation. Furthermore, insufficient wetting of the feather fibers by the molten PLA matrix can produce interfacial defects and micro-gaps around the fibers, further reducing stress transfer efficiency.

Another important factor contributing to the reduction in tensile strength is the increased frequency of fiber pull-out and interfacial debonding during loading. Instead of transferring the applied stress efficiently, weakly bonded fibers may separate from the surrounding matrix, consuming only a limited amount of fracture energy before complete failure occurs. This phenomenon becomes more pronounced at higher fiber contents due to the larger total interfacial area and the increased probability of fiber–fiber interactions.

The observed tensile behavior is consistent with numerous studies on natural fiber-reinforced PLA composites (Dhaou & Mnif, 2026; Hinchcliffe, 2015; Yiga et al., 2023), where moderate fiber contents often provide slight improvements in mechanical performance, whereas excessive fiber loading leads to reduced tensile strength because of poor dispersion, inadequate fiber-matrix adhesion, and increased structural defects (Kilinc, 2025; Morabiya & Joshi, 2026; Singhal et al., 2016). Similar trends have been reported for composites reinforced with cellulose (Ljungberg et al., 2006; Rahman et al., 2026; Siqueira et al., 2011), flax (Kesentini et al., 2022; Radkar et al., 2019; Yan et al., 2025), hemp (Hernández-Díaz et al., 2020; Masirek et al., 2007), bamboo (Bautista et al., 2025; Sayed et al., 2022), and poultry feather fibers (Soykan et al., 2022), where an optimum reinforcement content typically exists before mechanical properties begin to deteriorate.

All in all, the F_{max} parameters deduced from tensile strength results obtained showed that the incorporation of turkey feather fibers influences the mechanical performance of PLA in a concentration-dependent manner. While the addition of 3 wt.% TFF provides the most favorable tensile response among the reinforced composites, higher fiber loadings gradually reduce the maximum load-carrying capacity due to weaker interfacial bonding, fiber agglomeration, increased porosity, and premature crack initiation. The findings obtained indicate that further improvements in the F_{max} parameters may be achieved through fiber surface modification, chemical treatments, or the use of compatibilizing agents to enhance the interfacial adhesion between turkey feather fibers and the PLA matrix, accordingly enabling more efficient stress transfer and improved reinforcement efficiency.

3.2. Change of Elongation at Break

Secondly, the tensile strength findings enable us to determine the change of elongation of PLA matrix. Table 2 including the elongation at break results clearly displays that the incorporation of turkey feather fibers significantly influenced the ductility of the PLA composites. To illustrate the dramatic change of the elongation at break, we used Figure 2. The pure PLA specimen exhibited elongation value of 2.58%, indicating the characteristic deformation behavior of unreinforced PLA. Although PLA is generally regarded as a relatively brittle thermoplastic compared with conventional engineering polymers, the pure specimen retained a measurable capacity for plastic deformation prior to fracture. The addition of turkey feather fibers resulted in a substantial reduction in elongation at break, indicating that fiber reinforcement restricted the deformation capability of the polymer matrix. In more detail, the 1 wt.% TFF composite exhibited an elongation of approximately 0.80%, corresponding to a considerable decrease compared with pure PLA material. This reduction indicates that even a small amount of feather fiber limits polymer chain mobility and promotes earlier crack initiation during tensile loading. However, it is interesting that, the 3 wt.% TFF composites exhibited an elongation value of 1.75%, representing the highest ductility among all reinforced specimens, as shown in Table 2. The recorded value approach those of the pure PLA sample, indicating that a moderate fiber content provides a relatively balanced microstructure in which the fibers are sufficiently dispersed to reinforce the matrix without excessively restricting its deformation. This observation is consistent with the maximum load results, where the 3 wt.%-reinforced composite also exhibited the best tensile performance among the reinforced materials, as given in Figure 2.

Table 2 Differentiation of the elongation at break of prepared samples.

Samples	Elongation at Break (%)
Pure	2.58
%1 PLA-1	0.80
%3 PLA-3	1.75
%5 PLA-5	-
%7 PLA-7	0.86
%10 PLA-10	0.65

As the fiber loading increased beyond 3 wt.%, the elongation at break decreased continuously. The 7 wt.% composites exhibited an elongation value of 0.86%, while the 10 wt.% composite showed the lowest value of 0.65%. This is attributed to the fact that increasing the fiber content transforms the composite from a relatively ductile material into one exhibiting increasingly brittle fracture behavior. Although no elongation value is recorded for the 5 wt.%-reinforced specimen (Table 2), the corresponding reduction in maximum load and displacement indicates that the prepared composite structure would likely follow the same decreasing trend.

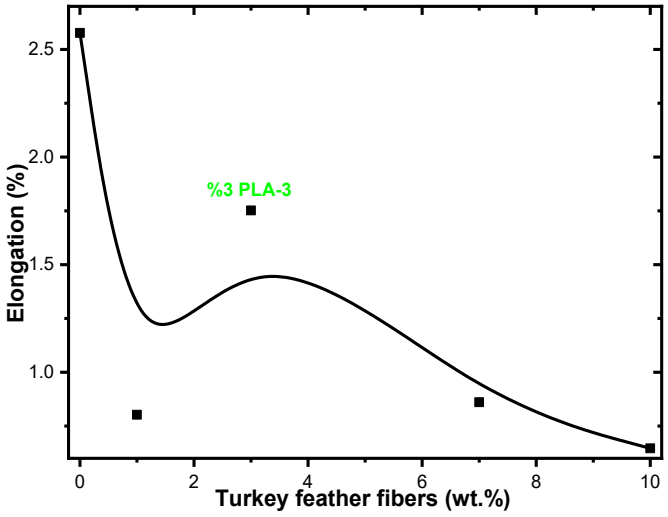

Figure 2. Variation of elongation at break with turkey feather fiber reinforcement of PLA matrix. Lines represent the general trend to guide the eye.

The reduction in elongation at break can be explained by several interacting mechanisms associated with the presence of natural fibers in the polymer matrix. Turkey feather fibers possess a significantly higher stiffness than PLA (Nur Ainin et al., 2022; Srinara et al., 2020; Talimi, 2011; Zhang et al., 2019) and therefore act as physical constraints that restrict the mobility of polymer chains during tensile deformation (Nur Ainin et al., 2022). As the fiber concentration increases, the continuous polymer phase becomes interrupted by a greater number of reinforcing fibers, reducing the matrix's ability to undergo plastic deformation before fracture (Chen & Turng, 2024; Khakalo et al., 2017; Sandeep et al., 2026; Zheng, 2000).

In addition to restricting polymer chain movement, higher fiber loadings increase the likelihood of fiber agglomeration, non-uniform fiber dispersion, and void formation within the composite structure. The microstructural defects reported may form localized stress concentration sites where cracks can initiate more easily under applied tensile loads. Once initiated, the cracks occurred propagate rapidly through the matrix, resulting in premature failure and lower elongation values. The quality of the fiber-matrix interface also plays a crucial role in determining the ductility of composites. Since untreated turkey feather fibers exhibit limited chemical compatibility with the hydrophobic PLA matrix, interfacial adhesion is relatively poor. The similar discussion is also performed for F_{max} values. Consequently, tensile loading typically leads to interfacial separation and fiber rupture instead of effective stress transfer from the matrix to the fibers. These interfacial failures reduce the composite's ability to absorb deformation energy and accelerate crack propagation, ultimately leading to reduced elongation at break.

To sum up, the elongation results deduced from the tensile strength experiments indicate that turkey feather fiber reinforcement decreases the ductility of PLA composites, with the extent of reduction becoming more pronounced as the fiber content increases. Among the reinforced specimens, the 3 wt.%-reinforced TFF composite exhibited the most favorable balance between tensile strength and ductility, revealing that this fiber loading provides the most effective compromise between reinforcement and deformation capability. In contrast, composites containing 7 wt.% and 10 wt.%-reinforced TFF compounds displayed significantly reduced elongation at break, confirming that the presence of excess fiber incorporation promotes brittle fracture due to restricted polymer chain mobility, increased stress concentrations, and insufficient fiber-matrix interfacial bonding. These findings are in good agreement with previous studies on natural fiber-reinforced PLA composites (Sandeep et al., 2026; Soykan et al., 2022; Zheng, 2000), where increasing fiber content generally leads to reduced ductility unless fiber surface modification or compatibilization techniques are employed to improve interfacial adhesion and stress transfer efficiency.

3.3. Effect of Turkey Feather Fiber Reinforcement on Maximum Displacement of PLA Matrix

We also determined the effect of turkey feather fiber on the maximum displacement of PLA matrix with the tensile strength experiments. We depicted the experimental findings in Table 3 and used Figure 3 to clearly illustrate the dramatic changes. One can see from the table that the maximum displacement at fracture exhibited a clear decreasing trend with increasing turkey feather fiber content in the PLA matrix, indicating a progressive reduction in the deformation capacity of the composites. The pure PLA matrix showed the highest displacement value of 2.305 mm, indicating the inherent ductility of the unreinforced polymer and its ability to sustain relatively large deformations before failure. Following the incorporation of turkey feather fibers, the displacement values decreased noticeably (Figure 3).

Table 3 Differentiation of the maximum displacement of prepared samples.

Samples	Maximum displacement
Pure	2.305
%1 PLA-1	1.025
%3 PLA-3	1.085
%5 PLA-5	1.05
%7 PLA-7	0.895
%10 PLA-10	0.959

The 1 wt.% TFF composite exhibited a maximum displacement of approximately 1.025 mm, representing a considerable reduction compared with the pure PLA specimen prepared. The 3 wt.% composite showed a displacement value of 1.085 mm, revealing that although the fibers limited the deformation capacity of the matrix, the reduction was relatively moderate at this reinforcement level. Similarly, the 5 wt.%

composite displayed a fracture displacement of 1.05 mm (Table 3), indicating that the addition of more fibers did not provide any improvement in deformation behavior. Increasing the fiber loading led to decreasing in the maximum displacement. In this context, as the fiber loading increased to 10 wt.%, the maximum displacement further decreased to 0.959 mm, while the 7 wt.% composites exhibited the lowest displacement value of 0.895 mm. The reported results clearly indicated that increasing the turkey feather fiber content progressively reduces the ability of the PLA matrix to undergo deformation prior to fracture.

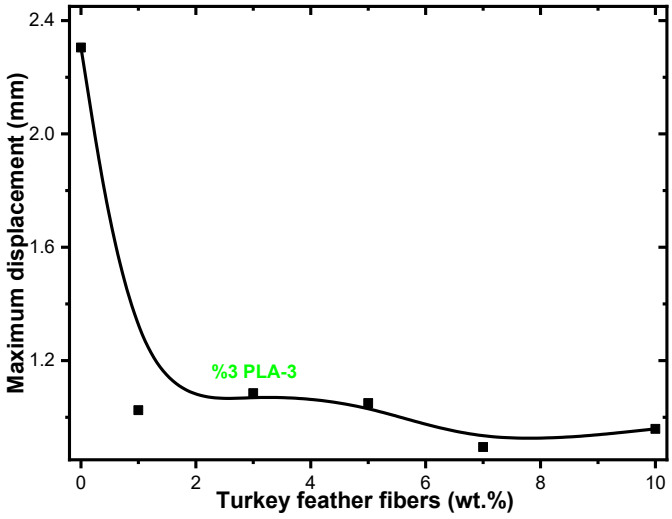

Figure 3. Influence of turkey feather fiber reinforcements on maximum displacement of PLA matrix. Lines represent the general trend to guide the eye.

The reduction in maximum displacement can be attributed to several microstructural factors associated with fiber reinforcement (Majdzadeh et al., 2006; Muhammad et al., 2018; Rapoport et al., 2002; Rashid et al., 2023; Run-ke et al., 2018; Trinh-Duc et al., 2021). Turkey feather fibers are considerably stiffer than the PLA matrix and therefore restrict the mobility of polymer chains during tensile loading. As the fiber concentration increases, the polymer matrix becomes increasingly constrained, limiting its ability to deform plastically. Furthermore, higher fiber loadings often lead to non-uniform fiber dispersion, fiber agglomeration, and the formation of voids or micro-defects within the composite (Chen & Turng, 2024; Muhammad et al., 2018; Rashid et al., 2023; Trinh-Duc et al., 2021; Zheng, 2000). These structural imperfections serve as stress concentration sites that promote premature crack initiation and accelerate crack propagation under tensile loading. Another important factor influencing the displacement behavior is the fiber-matrix interfacial adhesion, having already been discussed above. Since untreated natural fibers generally exhibit limited compatibility with hydrophobic PLA, the efficiency of stress transfer across the interface is restricted. Under tensile loading, weak interfacial bonding facilitates fiber pull-out and interfacial debonding instead of allowing the matrix to undergo significant deformation. Consequently, fracture occurs at lower displacement values, particularly at higher fiber contents where the total interfacial area increases substantially.

The observed decrease in displacement is also closely associated with the reduction in elongation at break obtained from the tensile tests. Both parameters consistently indicate that increasing turkey feather fiber content changes the mechanical response of the composite from relatively ductile to increasingly brittle. While low fiber concentrations (particularly 3 wt.%) still allow limited deformation before failure, higher reinforcement levels significantly reduce the composite's toughness and energy absorption capability.

Correspondingly, the maximum displacement results indicate that although turkey feather fibers can reinforce PLA, excessive fiber loading compromises the composite's deformation capability. The 3 wt.% TFF composite provides the most balanced mechanical response among the reinforced samples, whereas composites containing 7 wt.% and 10 wt.% TFF exhibit the greatest loss in ductility due to restricted polymer chain mobility, increased stress concentrations, and weaker fiber-matrix interactions. The recorded findings are consistent with previous studies on natural fiber-reinforced PLA composites (Bautista et al., 2025; Majdzadeh et al., 2006; Muhammad et al., 2018), where increasing fiber content generally leads to reduced fracture displacement and increased brittleness unless appropriate fiber surface treatments or compatibilizers are employed to improve interfacial adhesion.

3.4. Effect of Fiber Content on Maximum Displacement and Tensile Behavior

All the results recorded clearly present that turkey feather fiber content has a significant influence on the tensile response of PLA-based composites, particularly in terms of maximum displacement and deformation behavior. A systematic reduction in deformation capacity is observed as the fiber loading increases, indicating a transition from a more ductile polymer-dominated response toward a more brittle composite structure.

At low fiber contents (1–3 wt.%), the composites exhibit a balanced mechanical response, where moderate reinforcement is achieved without severely compromising ductility. In particular, the 3 wt.%-reinforced TFF composite stands out as the most favorable composition, showing the highest maximum load and comparatively higher elongation among all reinforced samples. This shows that at low loadings, turkey feather fibers are more effectively embedded within the PLA matrix, enabling relatively efficient stress transfer while still allowing limited polymer chain mobility. However, when the fiber content is increased beyond 3 wt.%, a clear deterioration in tensile performance is observed. Both maximum load and maximum displacement decrease progressively, indicating reduced load-

carrying capacity and diminished deformation capability. This degradation is primarily attributed to the increasing likelihood of fiber agglomeration, non-uniform dispersion, and insufficient interfacial bonding between the hydrophobic PLA matrix and hydrophilic feather fibers. On the other hand, at higher fiber concentrations, the probability of fiber-fiber contact increases, leading to incomplete encapsulation of fibers by the polymer matrix. This results in inefficient stress transfer across the interface and promotes localized stress concentration zones. Consequently, microcrack initiation occurs at lower strain levels, and crack propagation becomes more rapid, ultimately leading to premature failure. The mechanisms discussed collectively explain the observed reduction in ductility and maximum displacement at higher fiber loadings.

All in all, the findings observed reveal that while turkey feather fibers can act as effective natural reinforcements for PLA at low concentrations, excessive fiber incorporation adversely affects the structural integrity of the composite. Therefore, an optimal fiber content of 3 wt.% is identified, where a favorable balance between reinforcement efficiency and mechanical integrity is achieved.

3.5. Change of Mechanical Behavior Belonging to Turkey Feather Fiber-Reinforced PLA

The tensile test results obtained clearly show that the incorporation of turkey feather fibers significantly influences the mechanical behavior of PLA composites. The addition of TFF altered not only the tensile strength but also the deformation characteristics of the material, resulting in a gradual transition from relatively ductile behavior toward increasingly brittle fracture with increasing fiber content. This trend is evident from the simultaneous reductions in maximum load F_{max}, elongation at break, and maximum displacement observed as the fiber loading increased. The pure PLA specimens exhibited the highest tensile strength related parameters, such as F_{max}, elongation, and fracture displacement, confirming the superior mechanical integrity and deformation capability of the unreinforced polymer. Although PLA is generally considered a brittle thermoplastic, its continuous polymer matrix allows a relatively uniform distribution of applied stresses and enables limited plastic deformation before fracture. In contrast, the introduction of turkey feather fibers disrupted the continuity of the matrix and introduced additional interfaces that influenced crack initiation and propagation.

Among all reinforced composites, the 3 wt.% TFF formulation consistently exhibited the most favorable mechanical performance. This composition produced the highest maximum load, the greatest elongation at break, and one of the highest displacement values among the reinforced specimens, indicating that this fiber concentration provides the most effective balance between reinforcement and matrix continuity. At this relatively low fiber loading, the feather fibers appear to be sufficiently dispersed within the PLA matrix, allowing more efficient stress transfer while minimizing the formation of structural defects such as fiber agglomerates and voids. Consequently, the composite retains a reasonable degree of ductility while benefiting from the reinforcing effect of the fibers.

However, increasing the fiber content beyond 3 wt.% resulted in a progressive deterioration of tensile properties. Composites containing 5 wt.%, 7 wt.%, and particularly 10 wt.%-reinforced TFF exhibited lower maximum loads, reduced elongation at break, and smaller fracture displacements, indicating diminished tensile performance and reduced toughness. The findings obtained reveal that excessive fiber incorporation exceeds the reinforcing capability of the matrix and instead promotes defect formation within the composite. Several mechanisms may explain this behavior. Higher fiber contents increase the probability of fiber agglomeration, producing localized regions where stress is concentrated during tensile loading. In addition, insufficient wetting of closely packed fibers by the molten PLA matrix can generate voids, microcracks, and interfacial defects, all of which serve as preferential sites for crack initiation. Furthermore, the inherent incompatibility between the hydrophilic keratin structure of turkey feather fibers and the relatively hydrophobic PLA matrix limits the effectiveness of stress transfer across the interface. Under tensile loading, weak interfacial adhesion facilitates fiber pull-out and interfacial debonding, reducing the reinforcing contribution of the fibers and accelerating catastrophic failure.

The combined reductions in tensile strength, F_{max}, elongation, and displacement indicate that increasing fiber loading restricts polymer chain mobility and limits the ability of the matrix to undergo plastic deformation. Consequently, fracture occurs at lower strains and lower displacement values, showing a transition toward increasingly brittle mechanical behavior. This phenomenon is commonly observed in natural fiber-reinforced thermoplastic composites when the fiber content exceeds the optimum reinforcement level.

Accordingly, the experimental findings indicate that turkey feather fibers can function as an environmentally friendly reinforcement for PLA; however, their reinforcing efficiency is highly dependent on achieving an appropriate fiber concentration and adequate fiber-matrix interfacial bonding. The present results suggest that approximately 3 wt.% reinforcement represents the optimum reinforcement level for the composites produced in this study.

4. Conclusion

The tensile properties of PLA composites reinforced with turkey feather fibers were systematically investigated as a function of fiber loading. The results indicated that the mechanical performance of the composites is strongly influenced by the amount of fiber incorporated into the polymer

matrix. It is found that the pure PLA sample exhibited the highest tensile strength, F_{max}, elongation at break, and maximum displacement, revealing the superior mechanical integrity and deformation capability of the unreinforced polymer. The addition of turkey feather fibers generally reduced these tensile properties; however, the extent of deterioration depended on the fiber concentration. Among all reinforced specimens, the 3 wt.%-reinforced TFF composite exhibited the best mechanical performance, achieving the highest maximum load together with relatively high elongation and displacement values. This indicates that moderate fiber loading provides the most effective balance between reinforcement efficiency and preservation of matrix continuity.

In contrast, increasing the fiber content beyond 3 wt.% resulted in continuous reductions in tensile strength, ductility, and fracture displacement. These reductions are primarily attributed to fiber agglomeration, inadequate fiber dispersion, void formation, restricted polymer chain mobility, and weak interfacial adhesion between the turkey feather fibers and the PLA main matrix. These microstructural factors promote stress concentration, premature crack initiation, and brittle fracture, thereby limiting the reinforcing efficiency of higher fiber loadings.

Although untreated turkey feather fibers did not improve the tensile properties beyond those of neat PLA, the results demonstrate that they can be successfully incorporated into PLA to produce lightweight and sustainable biocomposites. The identification of 3 wt.%-reinforced material as the optimum fiber content provides valuable guidance for future material development.

Further improvements in mechanical performance are expected through fiber surface modification, alkaline or silane treatments, plasma treatment, or the incorporation of compatibilizers capable of enhancing the interfacial bonding between turkey feather fibers and the PLA matrix. Such approaches can improve strain transfer efficiency, reduce fiber clumping, and allow for higher fiber loads without compromising tensile performance. Therefore, the findings of this study provide an important basis for the development of environmentally friendly PLA-based biocomposites reinforced with poultry feather waste, contributing to both sustainable materials engineering and the valorization of agricultural by-products.

Conflict of Interest

The authors declare that they have no conflict of interest.

Disclosure of Generative AI Use

No generative artificial intelligence tools were used in the preparation of this article.

References

Abdur Rahman, M., Haque, S., Athikesavan, M. M., & Kamaludeen, M. B. (2023). A review of environmental friendly green composites: production methods, current progresses, and challenges. *Environmental Science and Pollution Research*, *30*(7), 16905-16929. https://doi.org/10.1007/s11356-022-24879-5

Akdogan, E., & Soykan, U. (2025). Sustainable rigid polyurethane foam composites based on used palm oil and turkey feather fiber: structural, morphological, thermal, insulation and mechanical properties. *Clean Technologies and Environmental Policy*, *27*(9), 3969-3984. https://doi.org/10.1007/s10098-024-03080-x

Aranberri, I., Montes, S., Azcune, I., Rekondo, A., & Grande, H. J. (2017). Fully biodegradable biocomposites with high chicken feather content. *Polymers*, *9*(11), 593. https://doi.org/10.3390/polym9110593

Baba, B. O., & Özmen, U. (2017). Preparation and mechanical characterization of chicken feather/PLA composites. *Polymer Composites*, *38*(5), 837-845. https://doi.org/10.1002/pc.23644

Barone, J. R., & Schmidt, W. F. (2005). Polyethylene reinforced with keratin fibers obtained from chicken feathers. *Composites Science and Technology*, *65*(2), 173-181. https://doi.org/10.1016/j.compscitech.2004.06.011

Bautista, B. E., De Gracia, E. H., Cacanando, C. J. D., & Leaño, J. L. (2025). *Comparison of the tensile behavior of coated vs uncoated bamboo (Bambusa blumeana JA & JH Schultes) textile reinforced mortar (TRM)*. The 5th International Symposium on Concrete and Structures for the Next Generation (CSN2025)At: The Verdure, Henry Sy Sr. Hall, De La Salle University. Manila.

Chen, E., & Turng, L. S. (2024). A double-expanded polytetrafluoroethylene fabrication method for increased mechanical compliance in tubular vascular graft applications. *Polymer Engineering & Science*, *64*(4), 1756-1769. https://doi.org/10.1002/pen.26652

Dhaou, I., & Mnif, R. (2026). Flexural, dynamic mechanical, and rheological properties of date palm fiber-reinforced PLA composites. *Fibers and Polymers*, *27*, 3447-3463. https://doi.org/10.1007/s12221-026-01430-8

Dutta, H., Bora, D., Chetia, P., Bharadwaj, C., Purbey, R., Bohra, R. C., Dutta, K., Varada Rajulu, A., Sadiku, E. R., Periyar Selvam, S., Gurusamy, P., Rawal, R. K., & Jayaramudu, J. (2024). Biopolymer composites with waste chicken feather fillers: A review. *Renewable and Sustainable Energy Reviews*, *197*, 114394. https://doi.org/10.1016/j.rser.2024.114394

Ghorbal, A., Sdiri, A., & Elleuch, B. (2019). Green approaches for materials, wastes, and effluents treatment. *Environmental Science and Pollution Research*, *26*(32), 32675-32677. https://doi.org/10.1007/s11356-019-06848-7

Hernández-Díaz, D., Villar-Ribera, R., Julián, F., Tarrés, Q., Espinach, F. X., & Delgado-Aguilar, M. (2020). Topography of the interfacial shear strength and the mean intrinsic tensile strength of hemp fibers as a reinforcement of polypropylene. *Materials*, *13*(4), 1012. https://doi.org/10.3390/ma13041012

Hinchcliffe, S. A. (2015). *Feasibility study of prestressed natural fiber-reinforced polylactic acid (PLA) composite materials* (Master's thesis, Colorado at Boulder University).

Kesentini, Z., El Mahi, A., Rebiere, J. L., El Guerjouma, R., Beyaoui, M., & Haddar, M. (2022). Static and fatigue tensile behavior and damage mechanisms analysis in aged flax fiber/PLA composite. *International Journal of Applied Mechanics*, *14*(08), 2250080. https://doi.org/10.1142/S1758825122500806

Khakalo, A., Vishtal, A., Retulainen, E., Filpponen, I., & Rojas, O. J. (2017). Mechanically-induced dimensional extensibility of fibers towards tough fiber networks. *Cellulose*, *24*(1), 191-205. https://doi.org/10.1007/s10570-016-1102-z

Khan, A. A., Parikh, H., & Qureshi, M. R. N. (2022). A review on chicken feather fiber (CFF) and its application in composites. *Journal of Natural Fibers*, *19*(16), 12565-12585. https://doi.org/10.1080/15440478.2022.2073495

Kilinc, A. C. (2025). Additive manufacturing and characterization of continuous nettle fiber-reinforced PLA composites. *Polymers*, *17*(17), 2388. https://doi.org/10.3390/polym17172388

Ljungberg, N., Cavaillé, J. Y., & Heux, L. (2006). Nanocomposites of isotactic polypropylene reinforced with rod-like cellulose whiskers. *Polymer*, *47*(18), 6285-6292. https://doi.org/10.1016/j.polymer.2006.07.013

Majdzadeh, F., Soleimani, S. M., & Banthia, N. (2006). Shear strength of reinforced concrete beams with a fiber concrete matrix. *Canadian Journal of Civil Engineering*, *33*(6), 726-734. https://doi.org/10.1139/l05-118

Mann, G. S., Azum, N., Khan, A., Rub, M. A., Hassan, M. I., Fatima, K., & Asiri, A. M. (2023). Green composites based on animal fiber and their applications for a sustainable future. *Polymers*, *15*(3), 601. https://doi.org/10.3390/polym15030601

Masirek, R., Kulinski, Z., Chionna, D., Piorkowska, E., & Pracella, M. (2007). Composites of poly (L-lactide) with hemp fibers: Morphology and thermal and mechanical properties. *Journal of Applied Polymer Science*, *105*(1), 255-268. https://doi.org/10.1002/app.26090

Morabiya, D., & Joshi, H. (2026). Natural fiber-reinforced PLA composites for fused deposition modeling: A critical assessment and experimental feasibility of jute fiber reinforcement. *ITEGAM-JETIA*, *12*(59), 611-624. https://doi.org/10.5935/jetia.v12i59.3533

Mrajji, O., El Wazna, M., El Bouari, A., & Cherkaoui, O. (2022). The properties of feather fiber-reinforced polymer composites: A review. *Journal of Natural Fibers*, *19*(13), 4868-4885. https://doi.org/10.1080/15440478.2020.1870633

Muhammad, A., Rashidi, A. R., & Buddin, M. M. H. S. (2018). Effect of coconut fiber reinforcement on mechanical properties of corn starch bioplastics. *International Journal of Engineering and Technology*, *7*(4.18), 267-270.

Murariu, M., & Dubois, P. (2016). PLA composites: From production to properties. *Advanced Drug Delivery Reviews*, *107*, 17-46. https://doi.org/10.1016/j.addr.2016.04.003

Nur Ainin, F., Azaman, M. D., Abdul Majid, M. S., & Ridzuan, M. J. M. (2022). Low-velocity impact behavior of sandwich composite structure with 3D printed hexagonal honeycomb core: varying core materials. *Functional Composites and Structures*, *4*(3), 035007. https://doi.org/10.1088/2631-6331/ac8d7a

Radkar, S. S., Amiri, A., & Ulven, C. A. (2019). Tensile behavior and diffusion of moisture through flax fibers by desorption method. *Sustainability*, *11*(13), 3558. https://doi.org/10.3390/su11133558

Rahman, M. A., Rahman, M. Z., Nag, R. K., Debnath, S., Al Rafi, H., Suad, M. R., Al Bashar, A., & Dev, B. (2026). Biocomposites reinforced with cellulose-rich snake plant and *Sesbania aculeata* lignocellulosic fibers: Fabrication, property optimization and structure-performance relationships. *Materials Today Communications*, *52*, 115110. https://doi.org/10.1016/j.mtcomm.2026.115110

Rajendran, S., Al-Samydai, A., Palani, G., Trilaksana, H., Sathish, T., Giri, J., Saravanan, R., Isaac JoshuaRamesh Lalvani, J., & Nasri, F. (2025). Replacement of petroleum based products with plant-based materials, green and sustainable energy—a review. *Engineering Reports*, *7*(4), e70108. https://doi.org/10.1002/eng2.70108

Rapoport, J., Aldea, C. M., Shah, S. P., Ankenman, B., & Karr, A. (2002). Permeability of cracked steel fiber-reinforced concrete. *Journal of Materials in Civil Engineering*, *14*(4), 355-358. https://doi.org/10.1061/(ASCE)0899-1561(2002)14:4(355)

Rashid, A. A., Ikram, H., & Koc, M. (2023). Effect of carbon fiber reinforcement on dimensional variations of 3D printed polyamide-6 composites: A simulation study. *Turkish Journal of Chemistry*, *47*(1), 33-39. https://doi.org/10.55730/1300-0527.3513

Reddy, C. C., Khilji, I. A., Gupta, A., Bhuyar, P., Mahmood, S., AL-Japairai, K. A. S., & Chua, G. K. (2021). Valorization of keratin waste biomass and its potential applications. *Journal of Water Process Engineering*, *40*, 101707. https://doi.org/10.1016/j.jwpe.2020.101707

Run-ke, H., Shu-guang, L., Li-hui, D., Jun-qing, Y., & Fei, H. (2018). Tunnel lining reinforced with carbon fiber: Effect simulation and construction technique. *Journal of Changjiang River Scientific Research Institute*, *35*(11), 69-75. https://doi.org/10.11988%2Fckyyb.20170536

Sandeep, M. P., Rudresh, B. M., Kumar, M. P., Kumar, M. P., Lingesh, B. V., Naik, N. C. K., & Emma, A. F. (2026). Exploring the effect of higher loading of short carbon fibers on mechanical and physico-mechanical characterization of polyamide66 and polytetrafluoroethylene blend composites. *Scientific Reports*. https://doi.org/10.1038/s41598-026-53792-x

Sayed, U., Dauletbek, A., Xin, X., Lorenzo, R., & Li, H. (2022). A review on the mechanical behaviour of bamboo reinforced concrete beams. *Journal of Renewable Materials*, *10*(12), 3629-3657. https://doi.org/10.32604/jrm.2022.022624

Shankar, A. N., & Netravali, A. N. (2025). Mechanical properties of chicken feather modified soy protein-based resins and jute fabric-reinforced green composites. *Polymer Composites*, *46*(6), 5517-5531. https://doi.org/10.1002/pc.29308

Singhal, A. V., Debnath, K., Singh, I., & Daniel, B. S. S. (2016). Critical parameters affecting mechanical behavior of natural fiber reinforced plastics. *Journal of Natural Fibers*, *13*(6), 640-650. https://doi.org/10.1080/15440478.2015.1102788

Siqueira, G., Tapin-Lingua, S., Bras, J., da Silva Perez, D., & Dufresne, A. (2011). Mechanical properties of natural rubber nanocomposites reinforced with cellulosic nanoparticles obtained from combined mechanical shearing, and enzymatic and acid hydrolysis of sisal fibers. *Cellulose*, *18*(1), 57-65. https://doi.org/10.1007/s10570-010-9463-1

Soykan, U. (2022). Development of turkey feather fiber-filled thermoplastic polyurethane composites: Thermal, mechanical, water-uptake, and morphological characterizations. *Journal of Composite Materials*, *56*(2), 339-355. https://doi.org/10.1177/00219983211056137

Soykan, U., Khaleel, M., Cetin, S., Yahsi, U., & Tav, C. (2022). Investigation of the relation between free volume and physico-mechanical performance in rigid polyurethane foam containing Turkey feather fibers: Part 2. *Journal of Cellular Plastics*, *58*(6), 893-915. https://doi.org/10.1177/0021955X221144541

Srinara, T., Lowrattanaounjit, N., & Chaochanchaikul, K. (2020). Improvement of mechanical properties of polylactic acid/oil palm fiber composites by alkali treatment. *Applied Mechanics and Materials*, *901*, 73-78. https://doi.org/10.4028/www.scientific.net/AMM.901.73

Talimi, M. (2011). *Characterization of natural fibre reinforced biodegradable composites* (Doctoral dissertation, Ontario Institute of Technology University).

Trinh-Duc, D., Piotrowski, A., Ajdukiewicz, C., Woyciechowski, P., & Gajewski, M. (2021). Estimation of post-cracking dissipation capabilities of fiber reinforced concretes in three point bending test monitored with application of digital image correlation system. *Materials*, *14*(17), 5088. https://doi.org/10.3390/ma14175088

Trivedi, A. K., Gupta, M. K., & Singh, H. (2023). PLA based biocomposites for sustainable products: A review. *Advanced Industrial and Engineering Polymer Research*, *6*(4), 382-395. https://doi.org/10.1016/j.aiepr.2023.02.002

Yan, Z. W., Bai, Y. L., & Zhou, Q. C. (2025). Dynamic tensile properties of flax fiber reinforced polymer composites. *Journal of Reinforced Plastics and Composites*, *44*(15-16), 926-938. https://doi.org/10.1177/07316844241233156

Yiga, V. A., Lubwama, M., Pagel, S., Olupot, P. W., Benz, J., & Bonten, C. (2023). Optimization of tensile strength of PLA/clay/rice husk composites using Box-Behnken design. *Biomass Conversion and Biorefinery*, *13*(13), 11727-11753. https://doi.org/10.1007/s13399-021-01971-3

Zhang, X., Chen, L., Mulholland, T., & Osswald, T. A. (2019). Effects of raster angle on the mechanical properties of PLA and Al/PLA composite part produced by fused deposition modeling. *Polymers for Advanced Technologies*, *30*(8), 2122-2135. https://doi.org/10.1002/pat.4645

Zheng, S. (2000). *The effect of interphase and interfacial cracks on the elastic and elastoplastic behavior of fiber-reinforced composites* (Doctoral dissertation, Rutgers The State University).

AIMS & SCOPE

Journal of Advanced Applied Sciences aims to publish relevant articles that focus on modern applications of Physics, Electrical and Electronics Engineering, Computer Science and Information Engineering and Material Science. We are particularly interested in applied research that makes significant scientific contributions across the broad spectrum of applied sciences.

The **Physics and Materials section** of the *Journal of Advanced Applied Sciences* targets the latest development in the Applied Physics area and its intersection with the Material Science. Some keywords that we are considering are: Electronic, Optical, Mechanical Magnetic and Structural properties of materials. Especially, Structure-Property relationship and characterization, Superconductivity, Cryogenics, Semiconductivity, Spintronics, Organic electronics, Perovskite/Silicon solar cells, Biomaterials and health applications, Bioelectronics and sensors, Photonic materials, Thermoelectric materials, Nanomaterials/nanoparticles, Energy transfer storage and conversion, Organic materials doping, Batteries, Alloys and ceramics, Applied biophysics and other topics related to applied sciences are of our interest.

The **Engineering section** deals with studies in various sub-disciplines of electrical and electronics and computer engineering technology such as Applied Engineering, Robotics and Control, Signal Processing, Data Analysis, Computational Systems, Communication Systems, Machine Learning, Artificial Intelligence and Deep Learning, Image Processing and Signal Processing, Big Data, Energy, Power and Industrial Applications, Systems security and data encryption, Microwaves and optics.

AUTHOR GUIDELINES

Manuscripts must be submitted to the journal in electronic version through online submission system at https://prensipjournals.com/ojs/index.php/jaasci/author-guidelines following the Author Guidelines of the journal.

Types of Paper

Research articles, review articles, short communications, and letters to the Editor.

• Research articles: original full-length research papers which have not been published previously and should not exceed 7500 words or 25 manuscript pages (including tables and figures).

• Review articles: on topical subjects and up to 10000 words or 25 manuscript pages (including tables and figures).

• Short communications: describing work that may be of a preliminary nature or a case report; preferably no more than 3000 words or 10 manuscript pages (including tables and figures).

• Letters to the Editor: should be included on matters of topical interest and not exceeding 2000 words or 10 manuscript pages (including tables and figures).

Page Charges

This journal has no page charges.

Preparation of Manuscripts

Papers must be written in English. Prepare your text using a word-processing software and save in ".doc" or ".docx" formats. Manuscripts must be structured in the following order:

• ***Title Page File***
  - Title (Concise and informative. Avoid abbreviations and formulae)
  - Author names and affiliation addresses (Full names should be given, no abbreviations. The corresponding author should be identified with an asterisk. Each affiliation address should include institution, faculty/school, department, city, and country)
  - ORCID numbers for all authors.
  - Corresponding author's e-mail, telephone number, and address
  - Acknowledgements (if applicable. Keep these to the absolute minimum)
  - Compliance with Ethical Standards
    - ❖ Conflict of Interest Statement
    - ❖ Statement on the Welfare of Animals (if applicable)
    - ❖ Statement of Human Rights (if applicable)

• ***Main File***
  - Title
  - Abstract (Should be between 100 and 350 words. References and abbreviations should be avoided)
  - Keywords (Minimum 3, Maximum 6 keywords)
  - Introduction
  - Materials and Methods
  - Results
  - Discussion (Can be combined with Results section if appropriate)
  - Conclusion
  - References
  - Table(s) with caption(s) (on appropriate location in the text)
  - Figure(s) with caption(s) (on appropriate location in the text)
  - and appendices (if any)

Manuscript Formatting

Use a 12-point Times New Roman font, including the references, table headings and figure captions, double-spaced and with 25 mm margins on all sides of A4 size paper throughout the manuscript. The text should be in single-column format.

• Each page must be numbered with Arabic numerals, and lines must be continuously numbered from the start to the end of the manuscript.

• Use italics for emphasis.

• Use only SI (international system) units.

• Use "dot" for decimal points.

References

Journal of Advanced Applied Sciences uses APA style (7th edition). Accordingly, authors must format their references as per the guidelines below. Please ensure that each reference cited in the text is also presented in the reference list. Authors should always supply DOI or URL of the work cited if available.

In-text citation (Narrative):

…The results of Bliss (2022) support…
…Sönmez and Taştan (2020) indicated that…
…According to the method of Öztürk et al. (2021)…

In-text citation (In parenthesis):

…It was found to be isometric (Öztürk, 2018)…
…is highly susceptible to friction (Doma & Craig, 2019)…
…have been studied (Kale et al., 2020)…

Two or more works in the same parenthesis:

…crushes under high pressure (Sönmez, 2018, 2019; Öztürk et al., 2020a; Kadak & Taştan, 2021)…

Citation in the reference list:

References should be listed first alphabetically and then further sorted chronologically at the end of the article. The citation of all references should conform to the following examples:

Article:

Lastname, N., Lastname, M., & Lastname, O. (Year). Title of the work. *Title of the Journal*, *Volume*(Issue), Page numbers. DOI

Tort, S. (1998). Stress and immune modulation in fish. *Developmental & Comparative Immunology*, *35*(12), 1366-1375. https://doi.org/10.1016/j.dci.2011.07.002

Kasumyan, A. O., & Døving, K. B. (2003). Taste preferences in fishes. *Fish and Fisheries*, *4*(4), 289-347. https://doi.org/10.1046/j.1467-2979.2003.00121.x

Özçelik, H., Taştan, Y., Terzi, E., & Sönmez, A. Y. (2020). Use of onion (*Allium cepa*) and garlic (*Allium sativum*) wastes for the prevention of fungal disease (*Saprolegnia parasitica*) on eggs of rainbow trout (*Oncorhynchus mykiss*). *Journal of Fish Diseases*, *43*(10), 1325-1330. https://doi.org/10.1111/jfd.13229

Article by DOI (early access):

Salem, M. O. A., Salem, T. A., Yürüten Özdemir, K., Sönmez, A. Y., Bilen, S., & Güney, K. (2021). Antioxidant enzyme activities and immune responses in rainbow trout (*Onchorhynchus mykiss*) juveniles fed diets supplemented with dandelion (*Taraxacum officinalis*) and lichen (*Usnea barbata*) extracts. *Fish Physiology and Biochemistry*. https://doi.org/10.1007/s10695-021-00962-5

Book:

Lastname, N., Lastname, M., & Lastname, O. (Year). *Title of the work*. Publisher.

Oidtmann, K., Xao, Q., & Lloyd, A. S. (2018). *The food need by the year 2050*. Elsevier.

Book Chapter:

Lastname, N., Lastname, M., & Lastname, O. (Year). Title of the chapter. In N. N. Lastname, A. Lastname & B. Lastname (Eds.), *Title of the book* (pp. Page numbers). Publisher.

Pickering, A. D. (1993). Growth and stress in fish production. In G. A. E. Gall & H. Chen (Eds.), *Genetics in Aquaculture* (pp. 51-63). Elsevier. https://doi.org/10.1016/b978-0-444-81527-9.50010-5

Dissertation or Thesis:

Lastname, N. (Year). *Title of dissertation/thesis* (Doctoral dissertation/Master's thesis, Name of Institution).

Sönmez, A. Y. (2011). *Karasu ırmağında ağır metal kirliliğinin belirlenmesi ve bulanık mantıkla değerlendirilmesi* (Doctoral dissertation, Atatürk University).

Taştan, Y. (2018). *Tatlısu kerevitindeki (Astacus leptodactylus) siyah solungaç hastalığı etkeni mantar Fusarium oxysporum'un PCR yöntemi ile teşhisi* (Master's thesis, Akdeniz University).

Conference Proceedings:

Lastname, N., Lastname, M., & Lastname, O. (Year). *Title of the work*. Title of the Conference. City.

Ken, A., & Kumar, S. (2020). *A new statistical model for fuzzy logic evaluation*. 3rd International Congress on Statistics. İstanbul.

Institution Publication:

Institution name. (Year). *Title of the work*. URL

FAO. (2020). *Fishery and aquaculture statistics 2018*. http://www.fao.org/3/cb1213t/CB1213T.pdf

Internet Source:

Lastname, N. (Year). *Title of the work*. Retrieved May 15, 2020, from URL

Perreault, L. (2019). *The future of agriculture: Polyculture*. Retrieved January 12, 2020, from https://www.agriculture.com

Table(s)

Tables, numbered in Arabic, should be in separate pages with a short descriptive title at the top. Place footnotes to tables below the table body and indicate them with superscript lowercase letters (or asterisks for significance values and other statistical data).

Figure(s)

All illustrations should be labelled as 'Figure' and numbered in consecutive Arabic numbers, Figure 1, Figure 2 etc. in the text. If panels of a figure are labelled (a, b, etc.) use the same case when referring to these panels in the text. Figures are recommended to be in electronic formats such as PNG, JPEG, TIFF (min.

300 dpi). All figures or tables should be presented in the body of the text.

Online Manuscript Submission
Authors are requested to submit manuscripts via the journal's online submission system at https://prensipjournals.com/ojs/index.php/jaasci/index

Submission Checklist
- Author Guidelines of the journal has been read and adhered

- **Title Page File**
  - Title
  - Full names, e-mails, and affiliation addresses of all authors
  - ORCID numbers of all authors
  - Corresponding author's e-mail, telephone number, and address
  - Ethical statements

- **Main File**
  - Continuous page numbers
  - Continuous line numbers
  - Blinded document (no personal information is present)
  - Title
  - Abstract (100-350 words)
  - Keywords (3-6 keywords)
  - All figures and tables are numbered and cited in order in text
  - Completeness and accuracy of the references have been checked
  - References have been edited as per the Journal guidelines

Publication Frequency
The journal includes original scientific articles on a variety of different subjects in English and is being published twice a year in June and December.

Publication Fees
Journal of Advanced Applied Sciences is an open access journal. No submission or publication charges are collected. All authors and readers have free access to all papers.

PUBLICATION ETHICS
Details about Publication Ethics can be found at https://prensipjournals.com/ojs/index.php/jaasci/policy

OPEN ACCESS POLICY
Details can be found at https://prensipjournals.com/ojs/index.php/jaasci/open-access

REVIEW PROCESS
Double-Blind Review and Evaluation Process
Double-Blind Review is a method applied for publishing scientific publications with the highest quality. This method forms the basis of an objective evaluation of scientific studies and is preferred by many scientific journals.

The views of referees have a decisive place in the publication quality of a Journal. *Journal of Advanced Applied Sciences* uses the double-blind review method, which means that both the reviewer and author identities are concealed from the reviewers, and vice versa, throughout the review process, in the evaluation process of all studies. For this reason, the authors are asked to blind their manuscripts before submitting. All the studies submitted to *Journal of Advanced Applied Sciences* are evaluated by double-blind review method according to the following steps.

1. Initial Evaluation Process
The studies submitted to *Journal of Advanced Applied Sciences* are first evaluated by the editor. At this stage, studies that are not in line with the aim and scope of the journal, are weak in terms of language and narrative rules in English, contain scientifically critical mistakes, are not original worthy, and cannot meet publication policies are rejected. Authors of rejected studies will be notified within one month at the latest from the date of submission. Eligible studies are sent to the field editor to which the study is relevant for pre-evaluation.

2. Pre-Evaluation Process
In the pre-evaluation process, the field editors examine the studies, introduction and literature, methods, findings, results, evaluation and discussion sections in detail in terms of journal publication policies, scope and authenticity of study. Study which is not suitable as a result of this examination is returned to the author with the field editor's evaluation report within four weeks at the latest. The studies which are suitable for the journal are passed to the referee process.

3. Referee Process
The studies are sent to the referees according to their content and the expertise of the referees. The field editor examining the study may propose at least two referees from the pool of *Journal of Advanced Applied Sciences* Advisory Board or referee pool according to their field of expertise or may propose a new referee appropriate to the field of study. The editors evaluate the referee's suggestions coming from the field editor and the studies are submitted to the referees. Referees are obliged to guarantee that they will not share any process or document about the study they are evaluating.

4. Referee Evaluation Process
The period given to the referee for the evaluation process is 15 days. Proposals for corrections from referees or editors must be completed by the authors within 1 month according to the "correction instruction". Referees can decide on the suitability of the study by reviewing the corrections and may also request multiple corrections if necessary.

Referee Reports
Referee evaluations are based in general on the originality of the studies, the method used, and the conformity with the ethical rules, the consistent presentation of the findings and results, and the examination of the literature.

This review is based on the following elements:

1. Introduction and Literature: The evaluation report contains the presentation and purpose of the problem addressed in the study, the importance of the topic, the scope of the relevant literature, the timeliness and the originality of the study.

2. Methodology: The evaluation report includes information on the suitability of the method used, the choice and characteristics of the research group, validity and reliability, as well as on the data collection and analysis process.

3. Findings: The evaluation report includes opinions on the presentation of the findings obtained in the frame of the method, the correctness of the analysis methods, the aims of the research and the consistency of the findings, the presentation of the required tables, figures and images and the conceptual evaluation of the tests used.

4. Evaluation and discussion: The evaluation report includes the opinion on the subject based on findings, relevance to research questions and hypotheses, generalizability and applicability.

5. Conclusion and suggestions: The evaluation report contains the opinion on the contributions to the literature, future studies and recommendations for the applications in the area.

6. Style and narration: The evaluation report includes compatibility of the title with the content, appropriate use of English in the study, refers and references in accordance with the language of the study and APA rules.

7. Overall evaluation: The evaluation report contains opinion on the authenticity of the study as a whole, its contribution to the educational literature and the applications in the area. The journal considers that scientists should avoid research which kills or damages any species of animal which, using IUCN criteria, is regarded as threatened or is listed as such in a Red Data Book appropriate for the geographic area concerned. In accordance with this view, papers based on such research will not be accepted by the Journal, unless the work had clear conservation objectives.

Plagiarism Detection
In agreement with publishing policies of *Journal of Advanced Applied Sciences*, plagiarism check is required for each study that has undergone the "Review Process". The Turnitin plagiarism checker software is used for plagiarism detection.

Proofs
Proof documents will be sent to the corresponding authors via e-mail. Proofs should be checked immediately and responses should be returned back within 15 working days. It is the responsibility of the authors to check carefully the proofs. No changes will be allowed after this stage.

DISCLAIMER
The Publisher and Editors cannot be held responsible for errors or any consequences arising from the use of information contained in this journal; the views and opinions expressed do not necessarily reflect those of the Publisher and Editors.

Editor or members of the editorial board are not responsible for the author's opinions and manuscript contents. Authors are responsible for the ethical originality of and possible errors in their manuscripts.

This journal is available online at http://jaasci.com/

Kindly visit website to search the articles and register for table of contents e-mail alerts.

LICENCE

INDEXING
Journal of Advanced Applied Sciences is currently indexed by

- Crossref
- Scilit
- Index Copernicus
- EuroPub
- Road
- Google Scholar

PUBLISHER
Prensip Publishing and Consultancy Ind. Trade. Co. Ltd.
Kuzeykent mah., Orgeneral Atilla Ateş Paşa Cad., No: 15CD,
İç Kapı No:31, Merkez/Kastamonu, 37150, TÜRKİYE
https://prensip.gen.tr
info@prensip.gen.tr

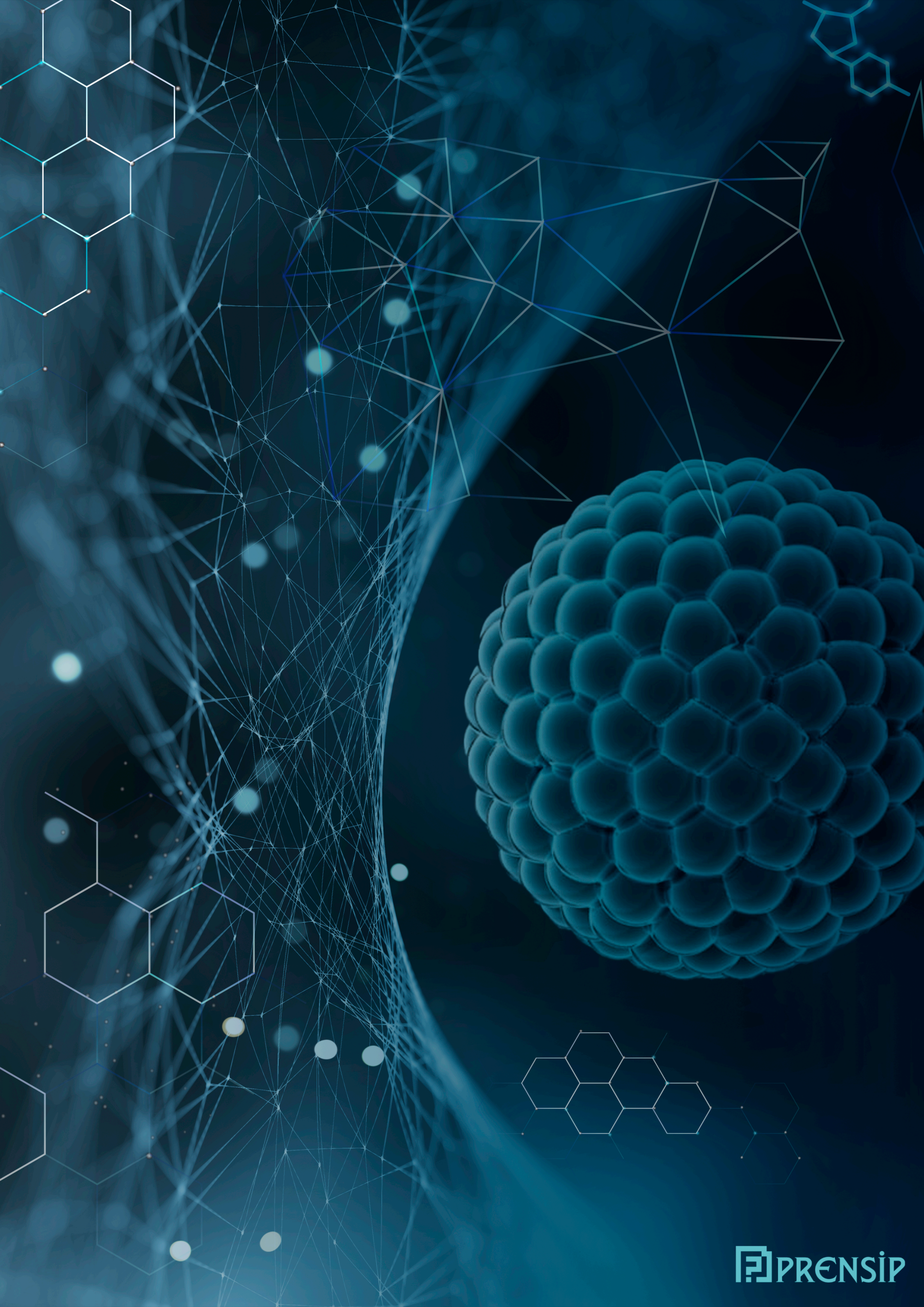
PRENSİP